ACCURACY STUDIES ON NON-DESTRUCTIVE METROLOGY OF SMALL HOLE

by

Zhige Zhang B.Sc. M.Sc.

Submitted for the degree of Doctor of Philosophy in the Department of Engineering, University of Warwick, UK

April. 1996

" When you can measure what you are speaking about and express it in numbers, you know something about it; but when you cannot measure it, when you cannot express it in numbers, your knowledge is of a meagre and unsatisfactory kind"

LOAD KELVIN
(1824-907)

CONTENTS:

6.4.2 Mirror size

6.4.3 Improvements

7. Further research and applications

7.1 Internal dimensional measurement

7.1.1 The accuracy

7.1.1.1 Improve original image

7.1.1.2 Improve software in edge detecting

7.1.2 Resolution

7.1.2.1 Internal multiple reflections

7.1.2.2 The optical character of ceramic

7.1.3 Computation speed

7.2 Internal surface roughness measurement

7.2.1 Reconstructing shadow image.

7.2.2 Shadow model

7.3 Other methods of internal inspection

List of Figures

List of Tables

Acknowledgements

I would like to express my thank to my supervisor, Dr. Peter Bryanston-Cross, for his guidance, constant encouragement and valuable criticism throughout the course of my studies. I am grateful to Prof. D. J. Whitehouse for his advice in many parts especially in surface metrology. Special thanks are due to my colleagues in Dr. Peter Bryanston-Cross' group for their fruitful discussions and especially helps in correcting the first draft of this thesis, to the technicians in Microengineering and Metrology Centre for their collaboration.

I would also like to take the opportunity to thanks Chinese government, The British Council and Dr. Peter Bryanston-Cross for their funding the project.

Abstract

The use and formation of small holes in different materials is critical to the efficient operation of many industrial processes. The application of such technology spreads across a very broad spectrum of problems, from the efficient ejection of diesel spray to the quality of drawn synthetic yarns. However, there is a lack of suitable non-destructive methods available for evaluating the quality of such holes below the size of 200 μm. This work has been further stimulated by evolving manufacturing technology which has both increased production throughput and the need to assess the quality of the hole.

The thesis concentrates on the application of digital image processing to conventional microscopy. In particular random edge detection and internal surface shadow image reconstruction algorithms have been devised to achieve an internal view of the hole. This has been achieved by selectively filtering the in-focus-strip formed by the microscope objective. Measurements have been made of the diameter, straightness and interior surface roughness. The method has been applied successfully to the following applications:

The internal 3-dimensional visualisation within a 0.2 mm diameter diesel injector hole. The objective is to give a complete account of the hole diameter and

straightness at the same speed as a spark erosion tool formed the hole. The internal surface roughness has also been measured.

The measurement of a spinneret holes used in the production of synthetic yarn. In this case the hole size varies from 0.07 to 0.5 mm in diameter.

Investigations have been performed for Rolls-Royce where an accurate measurement is required of the straightness and diameter within a typical turbine coolant hole. The exercise has also measured the wall thickness between the hole and the blade surface.

A research exercise has been tried for Marconi Electronics, their research specification being to construct the equivalent of a RS232 connector for fibre optic inter-connects. To achieve this they required a series of 0.1 mm holes through which to run a series of fibre optic cables. Again research has been performed to assess the straightness and diameter of these holes.

Further investigations has been made to investigate more general applications of the technique for the interior mapping of large production components.

Finally although the initial stages of this study were performed using a high cost research microscope an exercise to make a low cost dedicated automated inspection process has been successfully been completed.

List of publications

1. Z. Zhang and P. J. Bryanston-Cross "The accurate internal measurement of 200 micron diameter holes automatically by the use of three dimensional image processing" *Proceeding of LAMDAMAP 95* international symposium, 1995 Southampton UK

2. Z. Zhang and P. J. Bryanston-Cross "Detection of a random edge and its application to interior surface measurement" *Proc. SPIE Denver, Colorado* (1996) In publish .

3. Z. Zhang and P. J. Bryanston-Cross "Accurate dimensional measurements within a an internal structure" *Optical and Lasers in Engineering* In Publish.

4. Z. Zhang and P. J. Bryanston-Cross *The shadow image and the roughness of the internal surface of small hole* in Publish

1. Introduction and general review of small hole measurement and relevant techniques

The wheel might be one of the first few tools invented by humankind. It can be seen everywhere nowadays. During the long history of the wheel using, many methods have been developed to test how round a wheel is. It is called roundness measurement. In the measurement, the following aspects are checked [1 , Chapter 14] [2] (as shown in Figure 1-1):

(a) the roundness in every cross section;

(b) the concentricity between two different parts of the wheel;

(c) the parallel between the wheel surface normal and the axis;

(d) the concentricity between the hole and the wheel;

(e) the straightens of the hole.

Besides items d and e, which are related hole measurement, all other aspects can be found in cylinder measurement. This is because of the geometrical similarity between wheel and cylinder. Some equipment such as Tolyrond[1] can be used in both measurements.

When the measurement of hole is needed and the size is getting smaller, the difficulty of measurement rises. On the other hand, the use and fabrication of small holes in different materials is critical to the efficient operation of many industrial processes. The manufacture techniques are continually developing and requiring greater accuracy. A method of measuring the internal dimensions and

[1] Rank Taylor Hobson Ltd. Leicester England

surface roughness of small holes (approximately 0.07 - 0.25 mm in diameter and 0.5 - 6 mm in depth) has been devised and described in this thesis.

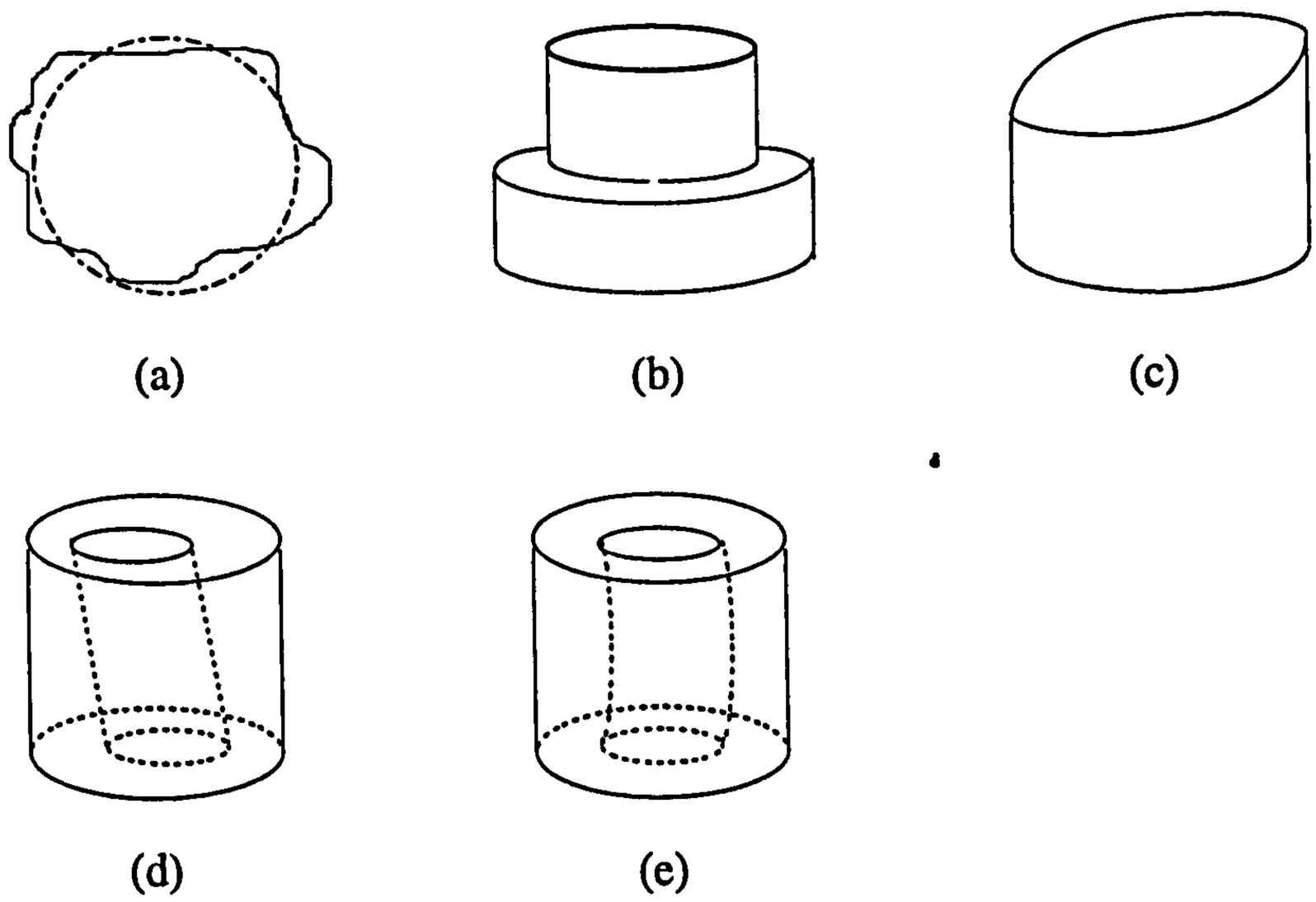

Figure 1-1 Different aspects in roundness measurement (see the text p.1)

The introduction of the problem (including the industrial background) and a general review about relative methods are given in Chapter 1. Chapters 2 -4 focus on the dimensional measurement: Chapter 2 describes the evolution of the methods, the design of software is discussed in Chapter 3. Chapter 4 presents examples of applications. Chapter 5 describes internal surface roughness measurement. Chapter 6 describes the dimensional measurement of internal structures. Chapter 7 is a discussion of further work.

1.1 Problems posed by internal dimensions and surface roughness in holes of approximately 0.2 mm diameter

The holes measured are in the size range of 0.07-0.25 mm in diameter and 0.5-6 mm in depth. They are formed by either spark erosion or pulsed laser. An example of surface roughness of Ra is 1.4 μm (it will be described in Chapter 5).

Conventional methods can not be used because of physical limitation. A measuring method is therefore needed to determine the dimensions and the deviation of small holes.

The non-destructive method of small hole measurement has two parts:

1) determining diameter and the depth of small holes.

2) evaluating the statistical parameters of the internal surface finish.

1.2 Industrial relevance of these measurements

The one of the first problems originated from Cummins, a US diesel engine manufacturer. The holes of injector are used to spread the fuel into the cylinder of the engine. Figure 1-2 is the picture of the injector. There are 8 holes at the tip of the injector, which cannot be seen in this picture. Figure 1-7 is a magnified image of the tip. The approximate dimensions of the hole are 0.2 mm in diameter and 0.7 mm in depth. In order to achieve a manufacture rate, the company makes the holes by spark erosion. This technique may allow the necessary rate of production, but it increases the number of component failures as well. The company therefore is interested :

1) measuring the shape of the hole

2) making a system to check the holes at the same speed as manufacture.

3) correlating the surface finish with the fuel efficiency.

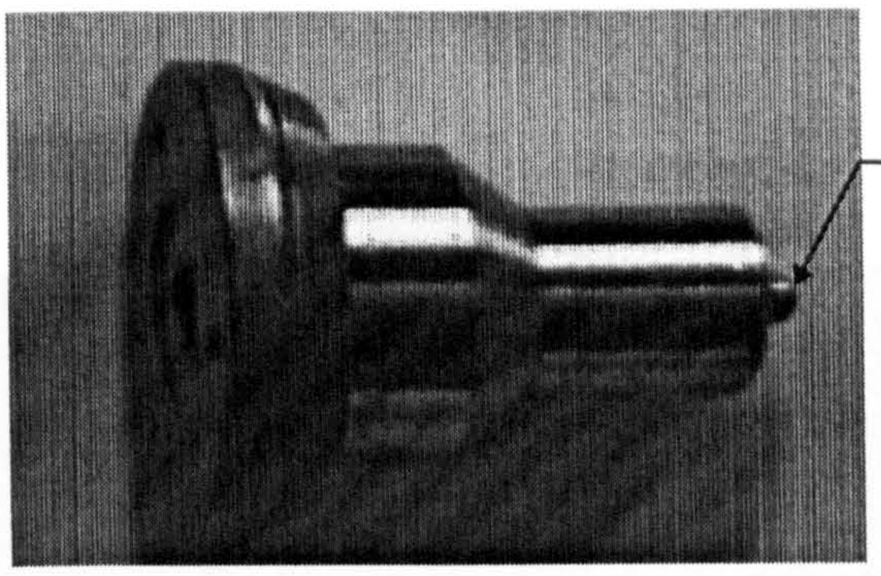

Figure 1-2 A diesel engine injector. There are 8 holes on the tip. Detail of the tip is given in figure 1-6 and figure 2-9 (a)

Another type of hole is shown in Figure 1-3 with 0.25 mm in diameter and 6 mm in depth. This hole is used to carry coolant through a turbine blade in a Rolls-Royce jet engine. Besides the dimension and the straightness, the thickness from the hole to the surface of the blade is also required. This is because the thickness is a factor in determining the blade strength.

A common property of these two holes is that only one end of the hole can be reached freely by the viewing system. The other end of the hole is inside the component where only a small cavity exists to access the measuring equipment.

A third example was supplied by Courtaulds, a UK textile business. Their spinneret hole is used to extrude polymer into yarn. The hole, as well as shown in finger 4-8 (p.92), has a non-parallel profile with 1 mm in depth and the diameter varies from 0.07 to 5 mm .

The fibre optic inter-connector of GEC-Marconi Electronics has 5 holes to hold fibres. The size of the hole is approximately 0.12 mm in diameter and 0.6 mm in depth. Both ends of Courtaulds and GEC-Marconi's holes can be reached freely by viewing system.

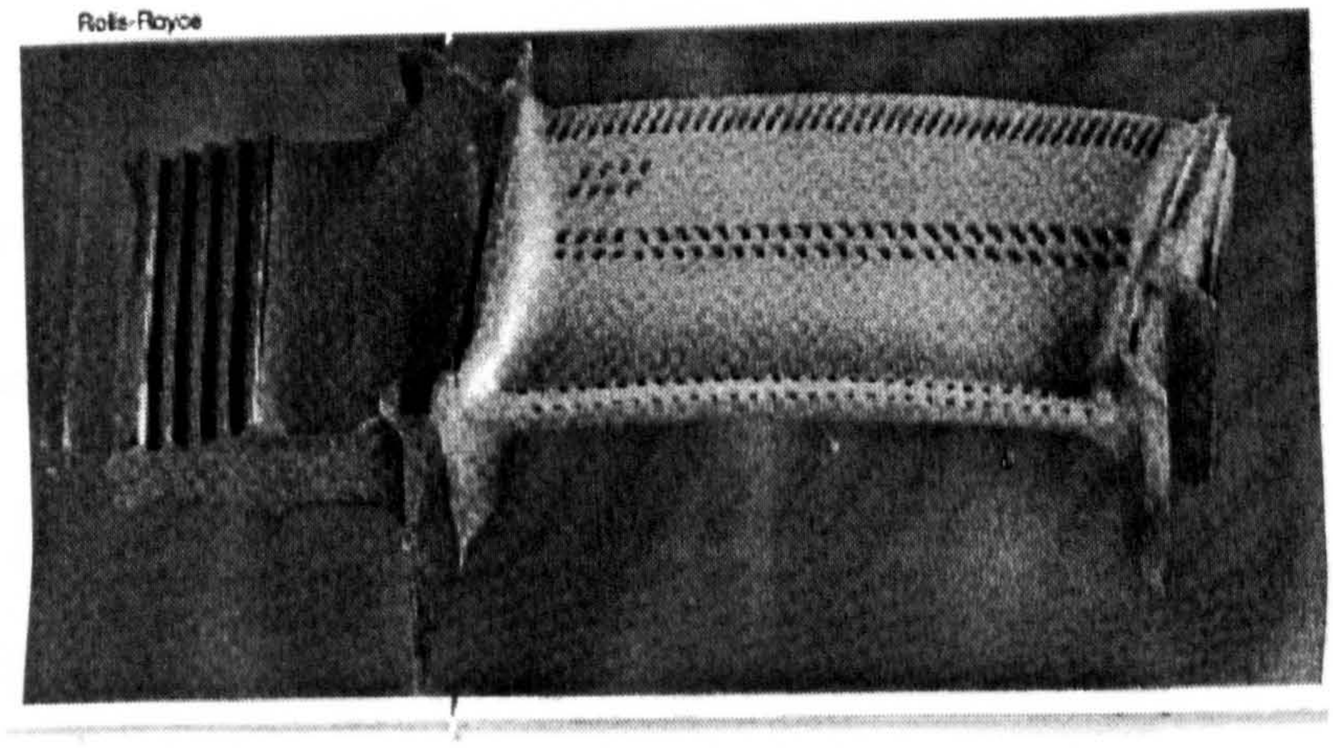

Figure 1-3 A turbine blade

1.3 Conventional small hole diameter measurement

There are several traditional methods for measuring the diameter of small holes [1, chapter 2 & 3]. The small hole gauge is one of them. This gauge consists of a split ball which can be expanded by rotating the handle to the size of the diameter of the hole. A three-point contact internal micrometer is another instrument used. The range of this gauge is from 7 mm to 200 mm with a accuracy of 2.5 μm. Both of the two instruments convert the rotation of the handle to the movement of the contact point inside the hole. It is obvious that they cannot be made very small. Because the measurement depends on three contacting points, it is not reliable if the cross section is far from being circle. Wire type plug gauges are also designed to measure diameters and can measure holes as small as 0.7 mm (0.03 inch), but

they can only give a possible single diameter judgement (pass or not pass) not specific shape. None of the instruments are automatic.

Currently no method was found which can give the straightness and surface roughness of such small holes non-destructively.

1.4 A review of non-destructive testing (NDT) [3]

Non-contacting optical testing has now become a fundamental metrological technique. Before starting on small hole measurement, it was deemed useful to review existing testing method. From them, it may be possible to define a method which could be used for the evolution of an internal measurement tool.

Many different techniques have been used in non-destructive testing (NDT) for different situations. In general, the methods divide into 4 groups. They are: 1) visual and optical inspection techniques; 2) radiation techniques; 3) acoustic and dynamic techniques and 4) others.

1.4.1 Visual and optical inspection techniques[3, part 2]

Interferometry methods, such as holography and speckle interferometry, are used in NDT for their high sensitivity (holography interferometry has half wavelength sensitivity in out-of-plane displacement and speckle interferometry has a one micrometre sensitivity in in-plane displacement) [4, Chapter 8]. They can therefore be used to detect the flaws inside the object by examining the

deformation on the outside surface. However they cannot achieve such a sensitivity when measuring the internal dimension from outside. Among recent works, The electronic speckle pattern interferometer (ESPI) NDT method has been verified by comparing with peel test [5] and studied in a real-time interval measurement[6]. Holographic NDT has been studied to expand the range and used in composite material studies[7].

Because of the human visual ability, any visual inspection is a simple, direct and clear method. Therefore, "an article should be visually inspected even when other more sophisticated NDT methods are used" [3, p. 28]. These visual methods are further combined with image processing techniques which can enhance the information from the original image or even construct an image of the object such as when using tomography [8].

It can be seen from the following chapters that visual inspection, including the conventional microscope and digital image processing, has been used in small hole measurements.

1.4.2 Radiation techniques [3, part 3]

The penetration of high energy particles (such as X-ray, Gamma and Neutron) and the characteristics of absorption by different material are used in NDT. The early method made 2-D shadow images were displayed to indicate material structures. This has been later developed into computerised 3-D images [8] - [12]. The main

disadvantage of these methods is that the sources used are not convenient and vacuum testing is usually needed.

1.4.3 Acoustic and dynamic techniques [3, part 4]

Continuous and pulse ultrasonic testing are also used in NDT. Because the propagation, reflection and attenuation of the wave are related to the structure flaws and stress states, they are used to detect the characteristic of the objects [13] - [25]. The methods are further combined with holography and data processing to improve sensitivity, resolution and quality of image [26], [27] - [29]. As the principle of the method is to measure the rebound signal, it is difficult to measure the complicated internal dimension. The multiple reflection will destroy the results.

1.4.4 Others techniques[3, part 5]

Other techniques are also used in NDT, such as magnetic particles, electrical and eddy current and thermal inspection techniques.

1.5 Optical surface finish measurement

Many different kinds of optical methods have been developed in surface metrology. This review is based on the tutorial given by Professor D. J. Whitehouse and his book[30]. The methods was divided into five groups as listed in Table 1-1 to Table 1-5 (pp. 19-23, the source of the data can be found from the

references in the following text): geometrical optics, wave optics, light scattering, follower technique and atomic scale. If the methods are divided in to geometrical and wave optics, there should be no other group. However, some methods listed in Table 1-3 and Table 1-4 have their special characteristic. Also although atomic scale methods are not strictly optical methods, they reflect the modern trend in measurement and have to be included for completeness.

1.5.1 Geometrical optics

The methods in this group are structured light (including triangulation[30, 4.3.5], light section and shadowing[30, 7.7.10.3] and moiré[30, 4.3.8]) and image comparison. The light is considered as a ray, and its behaviour can be described by geometrical analysis.

Perhaps the earliest examination of surfaces for engineering purposes is due to Schmalz [31]. He designed one of the first optical methods and the first stylus technique in 1929. The optical method he devised used the basic principle of triangulation in which an angular projection via an object is transformed by the surface geometry into a displacement of the image which could then be measured. In its simplest form a slit or edge is projected onto the surfaces. The surface geometry modulates the image which is viewed at a different angle with a microscope to produce a magnified profile as shown in Figure 1-4. The effective magnitude of the vertical geometric features (such as roughness) caused by the obliquity of the source projection is limited to about 50 × so that only

comparatively rough surfaces could be examined. The great advantage of this method is its simplicity and the direct presence of a simple image on the surface.

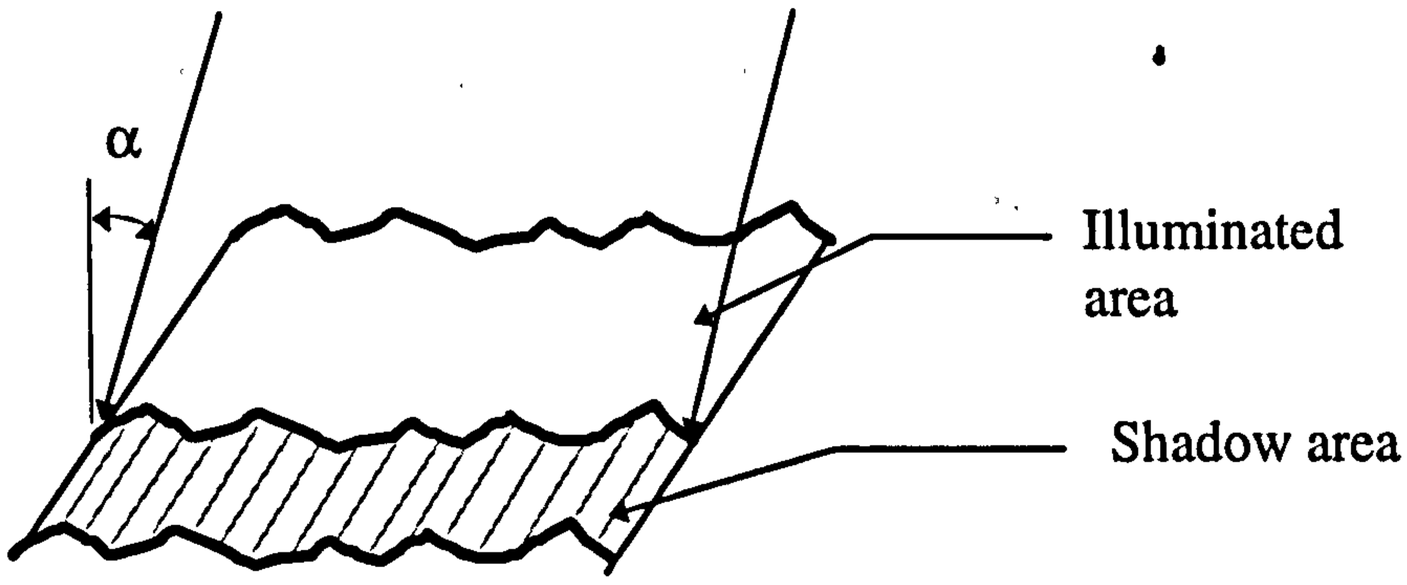

Figure 1-4 Oblique light edge profilometer

An extension of this technique is that in which fringes are projected on to the surface. This provides areal information. To analysis this information moiré fringes analysis is used in which the working fringe pattern is seen via observer optics [30, 4.3.8]. These have been used to measure form error e.g. curvature and flatness rather than roughness. Some recent works are still in this area [32] - [37].

This simple measuring principle is used in Chapter 5 to calculate the surface roughness after the shadow image is reconstructed.

1.5.2 Wave optics

Light may be interpreted as either scalar or polarised electromagnetic waves. Methods in this section include ellipsometry, speckle and interferometric phase-stepping analysis.

Ellipsometry is an example in which some state of polarisation is used as a measure of roughness[30, 7.8.11]. Because of the sensitivity of polarised light to surface structure the areal properties or "lay" of the surface can be characterised using this method. Intrinsically, this method is best used for comparison because the changes in polarisation are often due to surface films rather than the roughness as such. The extreme sensitivity of the polarisation method stems partly from the fact that the behaviour is rather than scalar. It is often difficult to make the necessary inversion from the distribution of light scatter to obtaining a value of roughness. Insofar as a surface film can be regarded as part of the surface geometry, ellipsometry is a useful tool for the measurement of its thickness. Provided that the roughness and film effects can be separated method provides a useful measure of surface integrity.

Speckle is a property of coherent light, when the light is reflected or passes though a non-smooth surface. The relationships between the speckle effect and the surface have been examined to measure the roughness[38]. Direct evaluation of the correlation function of the surface and its height are found by speckle correlation and speckle contrast techniques. From evaluation and deformation geometry are described in terms of electronic speckle pattern interferometry (ESPI) using the advantage that the speckle spatial bandwidth is well suited to the bandwidth of TV cameras and electronics. The measurement of form, having a lower bandwidth than roughness, has been achieved with particular success using this method.

An interference pattern can be generated when two coherent plane wave fronts meet together on a surface[39, chapter 9]. The pattern $I(x,y)$ can be written as:

$$I(x,y)=a+ b \sin(2\pi(x(\cos(\theta_1)+\cos(\theta_2))+z(x,y)(\sin(\theta_1)-\sin(\theta_2)))/\lambda+ \varphi) , \quad 1.1$$

where a and b are independent of z, the surface profile, θ_1 and θ_2 are incident angles of two plane wave fronts as illustrated in Figure 1-5. Along the curves of $I(x,y)$ reaches its minimum or maximum, fringes are found. Therefore in fringe analysis the information of the surface profile can only be got only where

$$2\pi(x(\cos(\theta_1)+\cos(\theta_2))+z(x,y)(\sin(\theta_1)-\sin(\theta_2)))/\lambda = n\pi + \pi/2, \quad n= 0, 1, \ldots \quad 1.2$$

Phase stepping technique is used to analysis the phase distribution of this interference pattern on the surface. It therefore can give more information with a high resolution. By giving one of the waves a few known phase shifts steps, say four, the z then can be deduced from follow fringe patterns for the whole area:

$$I_i(x,y) = a+ b \sin(2\pi(x(\cos(\theta_1)+\cos(\theta_2))+z(x,y)(\sin(\theta_1)-\sin(\theta_2)))/\lambda+ \varphi_i)$$

$$i=1, 2, 3, 4 \quad 1.3$$

A horizontal resolution of profile 7 nm measured by phase stepping technique has been achieved with noise-limited vertical resolution of 0.3 nm/square-root Hz [40]. The phase stepping method has also been used in moiré fringe analysis. The resolution of measurement is 1 μm on displacement and 10^{-5} on the strains [41]. Phase-stepping microscopy (PSM) has achieved a vertical resolution of 1 nm and horizontal resolution of 0.6 μm [42]

This method can possibly be used in further internal surface profile analysis. It is discussed in Chapter 7.

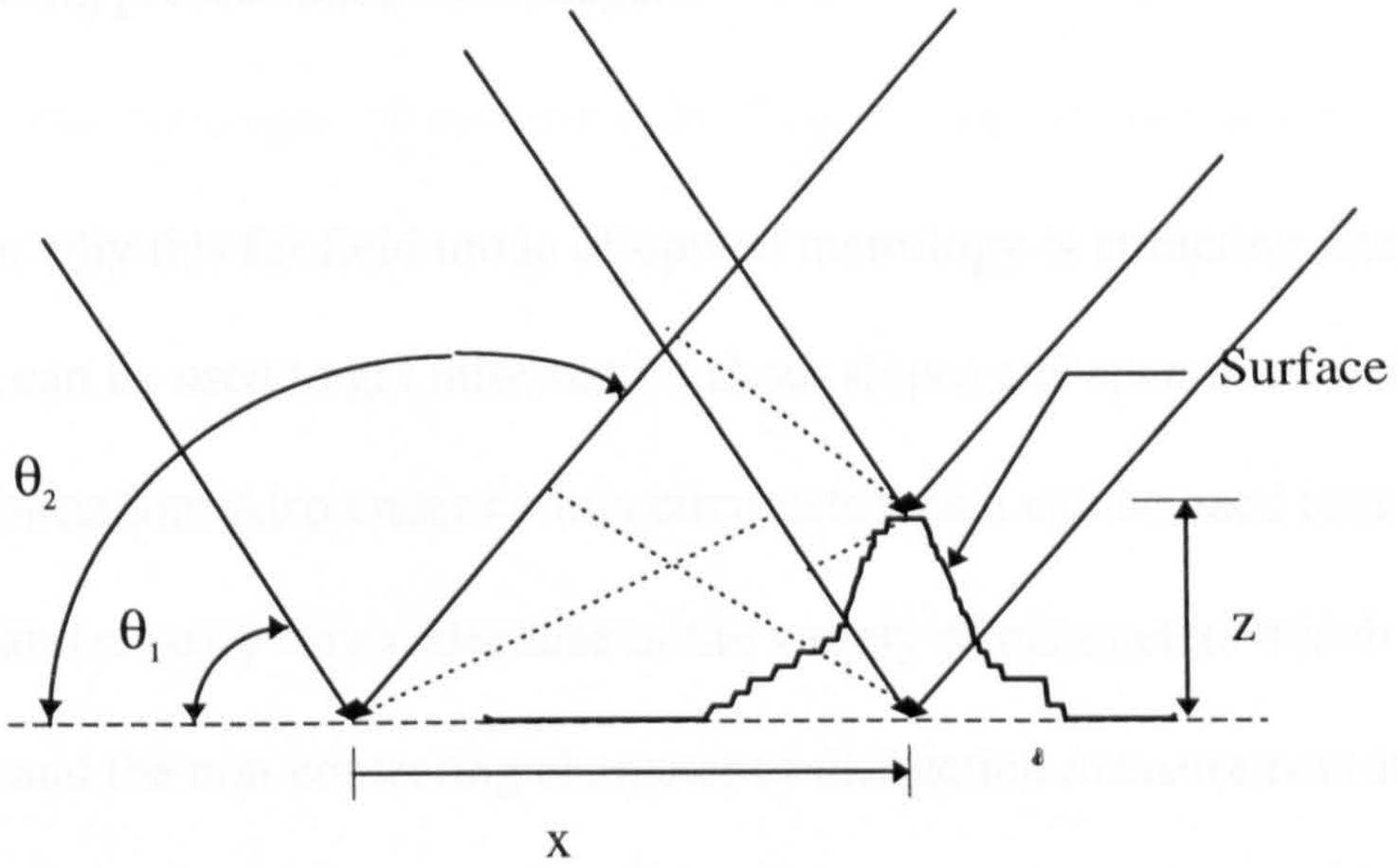

Figure 1-5 The phase changes caused by height distribution

1.5.3 Light scattering [30, 4.3.12]

In order to estimate the roughness, all the light scattered is used. This is Total Integrated Scatter (TIS) and as the name implies the scattered light is measured over all angles. The result is obviously independent of angle. Other methods which make use of the way the scattered light is distributed as a function of angle (BRDF, Bi-directional reflection distribution function) are studied. These methods are more versatile than the TIS technique and can be used to get meaningful estimates of rougher surfaces. The point should be made that these methods are best used for comparison purposes and even then confined to similar manufacturing processes. For very rough surfaces the geometrical mode of scatter is invoked to give surface roughness slopes. For finer surfaces the spacing becomes important. The far field scatter resembles the power spectral density of

the surface if it is sufficiently smooth. The accuracy depends on the ratio of the roughness to the wavelength of light but there is a growing use of mathematical algorithms to extend the range to rougher surfaces providing that the manufacturing process does not change.

The reason why this far field mode of optical metrology is attracting attention is because it can be used to get information about slopes and spectra as well as the height information. Also under certain circumstances it can be used to measure waviness and classify flaws. Because of the variety of parameters which can be estimated and the non-contacting character of diffraction measurement it is being considered for in-process monitoring of machine tool behaviour as well as the prediction of functional behaviour of surfaces in tribological situations.

However, as the measurement of the industrial holes (concerned in section 1.2 p.3) allows only a very restricted angle to view and illuminate the surface, these methods are not suitable for this measurement.

1.5.4 Follower techniques[30, 4.3.3]

There has been a desire to develop instruments which have the basic versatility of the stylus technique for measuring surfaces and yet be free from any surface damage implications. Optical "follower" techniques are perhaps the most successful. In these the mechanical stylus is replaced by a focused cone of light. Also the mechanical "skid" often used in practical stylus instruments is replaced by an optical equivalent - sometimes a defocused cone.

Heterodyne technique is used in interferometry[304.3.7]. It is a "phase follower". As one of the light is given a frequency shift(2 MHz - 100 MHz), when these two lights meet together, a signal with the shift frequency can be cane be detected. The electronic technique "phase lock loop" is used to measure the phase change caused by surface profile.

Conventional follower systems constitute in one form or another the original method of Dupuy [43] which detects the defocus of the light spot on the surface by means of masks in the image plane - the knife edge test. Another variant is achieved by simply using the spot size change with defocus. Many variations on this have been tried. All use a closed loop control to maintain focus of the objective lens on the surface as the probe is scanned laterally.

These methods can be very sensitive to z displacement and are capable of measuring to fractions of nanometres. The danger is the expectation that such instruments give the same values for roughness as stylus methods. As a rule agreement will only occur if the curvature of the surface is low i.e. local radius of curvature of the geometry should be large compared with the wavelength of light λ otherwise diffraction can occur at sharp points and edges which will destroy fidelity. This problem is associated with all optical methods. So neither method optical or stylus is without substantial problems.

The sensitivities of optical follower methods, especially when coupled with accurate x and y stages, are very high. However, because of the relatively large value of λ the wavelength of light, significant interpolation of phase is necessary. The large interpolation is difficult to justify metrologically. The feature being measured should wherever possible be of the same scale as the unit of measurement i.e. λ. There is a serious mismatch in the case of visible light and has led to interest in the possibility of using wavelengths which are considerably shorter, in particular x-ray. These are considered in the next subsection.

More discussions about followers are given in chapter 2.

1.5.5 Atomic scale technique

The availability of soft x-ray sources has led to the possibility of using the scatter of grazing incidence x-rays to determine the surface roughness value and also some attempt has been possible to estimate the auto-correlation function of the surface[30, 7.8.3]. It seems that scalar theory and Beckmann analysis[44] gives a reasonable explanation of the scatter in just the same way for x-ray as for visible light. Hard x-rays have also been used but suffer from the property of deep penetration. Values of roughness in the region of 1 nm can be investigated.

Surface measuring techniques using x-ray obey the rules of metrology mentioned above more nearly than when visible light is used but the extreme grazing angle necessary imposes severe practical restrictions on surface shape. In practice up to now only nominally flat surfaces have been examined.

Potentially x-ray are superior to visible light as a tool for general surface examination because of the extra ability of the rays to penetrate the surface skin as a function of grazing incidence angle. This penetration can be used to investigate the surface elastic modulus and local strain. Therefore it is inevitable that the use of integrated parameters involving geometrical and material properties of the surface will supercede that of geometry alone because the properties of the surface will be more adequately covered.

Raman and other elastic and non-elastic scattering[30, 7,8.1.2 & 7.8.3.1] are also possibilities. Secondary electron scattering and its large depth of focus has been used to effect but even with a number of detectors the ability to reveal accurate height information has been elusive.

Optical performance is often limited by diffraction effects. This has been a severe limitation restricting resolution to a fraction of λ. It was pointed out by O'Keefe [45] that at sufficiently near field the conventional criteria involving λ could be replaced by one in which the physical dimensions of the probe becomes the limitation. Most modern scanning microscopes utilise this principle. Near field optical scanning provides resolution in the 20 nm range. This is achieved by means of an effective evanescent escape mechanism.

Much work has recently concentrated on scanning probe microscopes working on a closed loop null action based on some atomic phenomenon such as charge

density or force[30, 4.2.3]. In such cases a solid probe is the sensor. This new technology, to some extent , resurrects the traditional stylus contact technique although "contact" at the atomic level is difficult to define. Also problems of resolution are even more dependent on tip dimension a factor which has taken on considerable importance. It must suffice to consider that in these new microscopes the fields of optical surface metrology and stylus surface metrology have effectively been merged.

Table 1-1 Geometrical optics

	Structured light				Image
Subset	Light sectioning and shadowing	Triangulation detection of surface	Projected moiré	Reflected moiré	Comparison
Height sensitivity	0.5 μm	0.5 μm	1/50 fringe	1/25 fringe	1nm
Height range	2-200 μm	~500 μm		500 × *	100 nm
Horizontal sensitivity	20 μm	0.5 - μm 0.3-15mm		~ 0.01 mm	10 μm
Horizontal range	Determined by optical scheme	60 - 200 mm	10^4× *	10^4× * ~ 100 mm	2 mm
Roughness	5 μm Ra	-	-	-	Ra ~ 0.1 μm
Form	400 μm	Flatness via autocollimator sensitivity 0.3" arc	Contouring convex surface shadow for small object	Slope flatness 0.1 - 1 mm	-
defects		-	-	-	
Thickness		As height			
Position		0.1 μm on polished surface		As horizontal sensitivity × 5	

* related sensitivity

Table 1-2 Wave optics

	Ellipsometry	Speckle		Interference
Subset	Ellipsometry	Contrast	interferometry & correlation	Phase stepper
Height sensitivity	0.1 μm	0.6 μm	1 μm	0.1 nm
Height range		6 μm	10 μm	0.1 μm
Horizontal sensitivity	2 μm		~ 2 μm	1 μm
Horizontal range Bandwidth		Cut-off simulated by spread function	25 μm contour 10 - 100 mm typical	~ 100 μm
Roughness		Contrast 0-1 for Ra ~ $\lambda/5$. Range increased white light	1 - 30 μm using two angles	
Form			Complex shape on rough surfaces possible using ESPI	
Thickness	Thin film measurement			

Table 1-3 Light scattering

	Angle scatter (source modulated by surface)			
Subset	Gloss	TIS	ARS (BRDS)	Diffraction
Height sensitivity	-	1 nm ~ .001 λ		10 nm - 0.05 λ
Height range	-	0.1 λ		120 nm
Horizontal sensitivity	2		0.5 - 5 μm	10 μm
Horizontal range Bandwidth	50			~ 30 μm
Roughness	Used only for comparison purpose	0.5 nm- 0.2 μm		< λ/4
Form		can cause problems	-	lateral shift in spectrum origin gives waviness
Defects	-	Defects scatter light in all direction	Possible providing spatial bandwidth separation	Filtering in reconstruction or of axis selection
Thickness		-		Dimensional information possible with small objects and r plane
Step high	Indirectly only	-	-	Only with respect to close plane

Table 1-4 Follower techniques

Subset	Heterodyne	Nomarski	Confocal	Focus (typical)
Height sensitivity	λ/3600		100 nm	> 0.1 nm
Height range	λ/3600 ~ 0.01 nm	-		5 μm
Horizontal sensitivity	-	-		0.1 μm
Horizontal rang	2 μm			1 mm
Form	~ 1 nm after filter	< 25 nm Ra		spheres & general curves, waviness
Defects	Shape 10 nm - 40 μm	Reduces influence of tilt		Related to spot size
Thickness				Only via step height

Table 1-5 Atomic scale

Atomic scale					
Subset	X-ray	Raman	Near field	STM	AFM
Height sensitivity			1 μm		0.01 nm
Height range					1 μm
Horizontal sensitivity	0.8 μm		0.3 μm	10 nm	0.1 μm
Horizontal rang	100 μm				
Thickness		1 bn - 50 nm			

1.6 Destructive measurement of small hole using scanning electron microscopes

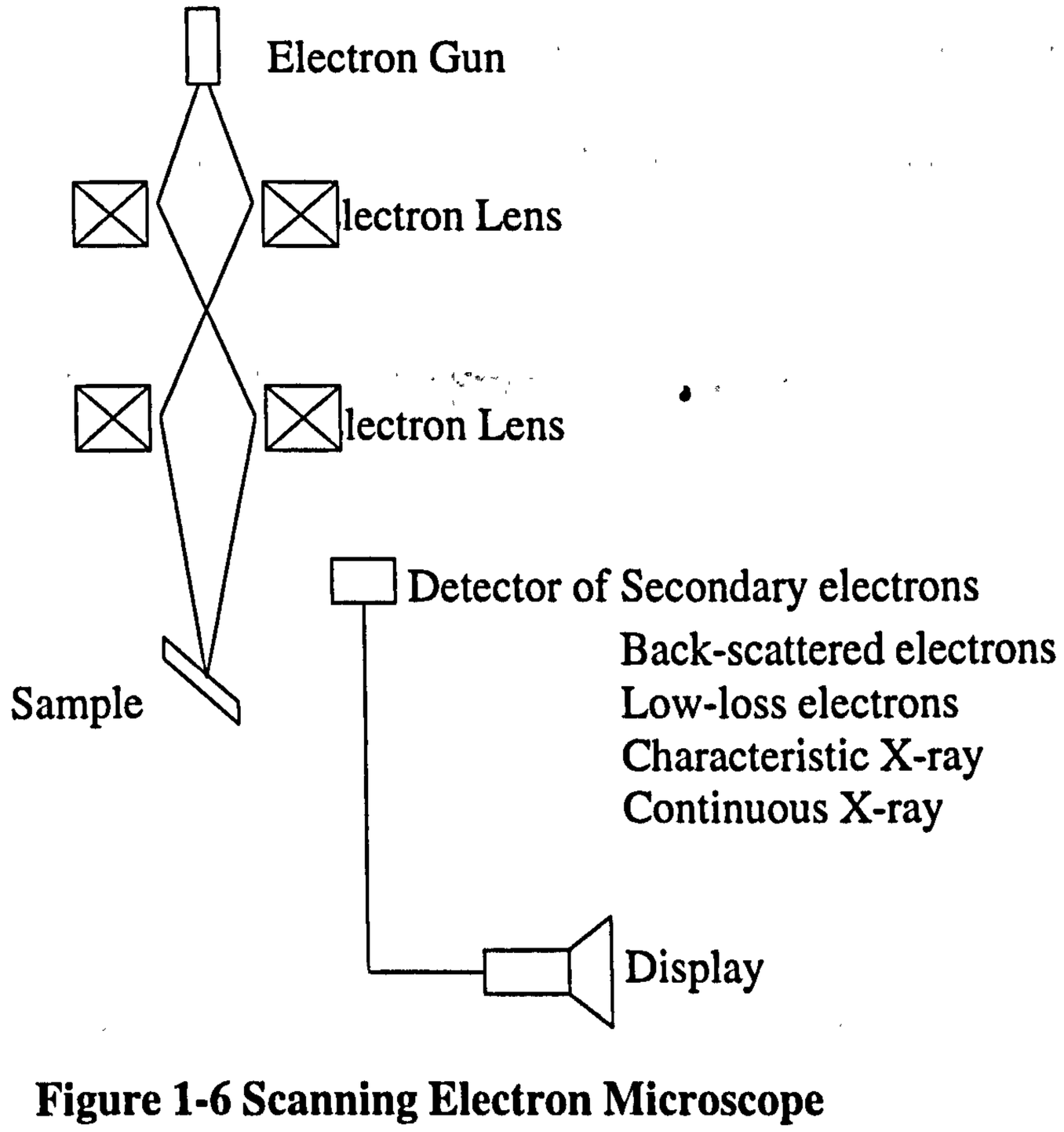

Figure 1-6 Scanning Electron Microscope

The scanning electron microscope (SEM) is a powerful tool for surface texture studies. The principle of SEM is that when an electron beam hits a metal surface, some form of radiation is released as shown in Figure 1-6. The radiation takes the form of secondary, back-scattered or low-loss electrons and characteristic or continuous X-ray. The intensity of the radiation depends upon the shape, chemical composition and crystal orientation at the surface where the beam hits. The electron beam can be focused into a very fine spot, as small as 10 nm in diameter (the order of vision light wavelength is about 550 nm). The resolution of SEM is reported as a few nanometers [48],[49]. Mr H. Hingle, Department of Engineering,

University of Warwick, studied the internal surface of a Cummins injector's hole by the method of SEM. To achieve this, the hole is cut along its axis and SEM image of the surface is taken which provided an initial visualised image of the surface formed inside hole. Figure 1-7 is SEM image of the inside tip of the injector. On the top of the image, it can be seen that the cavity inside the tip is approximately 1 mm in diameter. Figure 1-8 is SEM image of the internal surface of the hole.

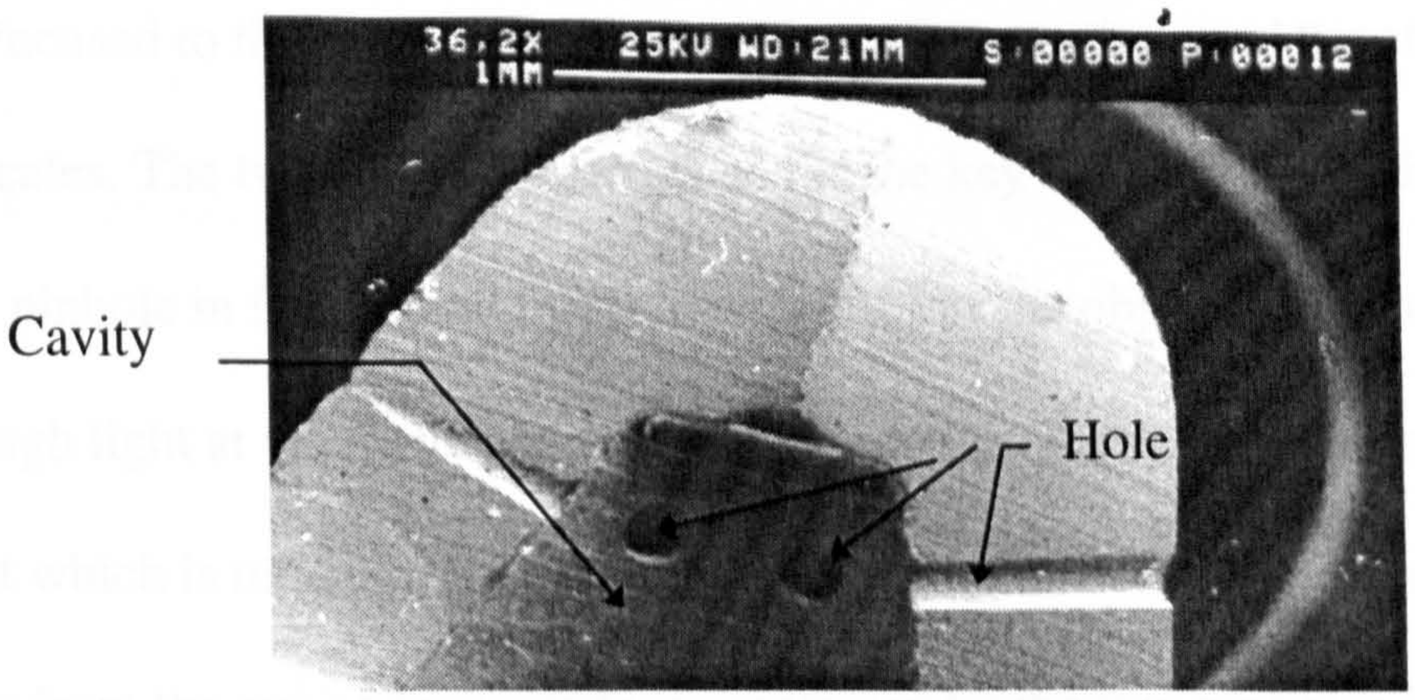

Figure 1-7 A SEM image of the inside injector

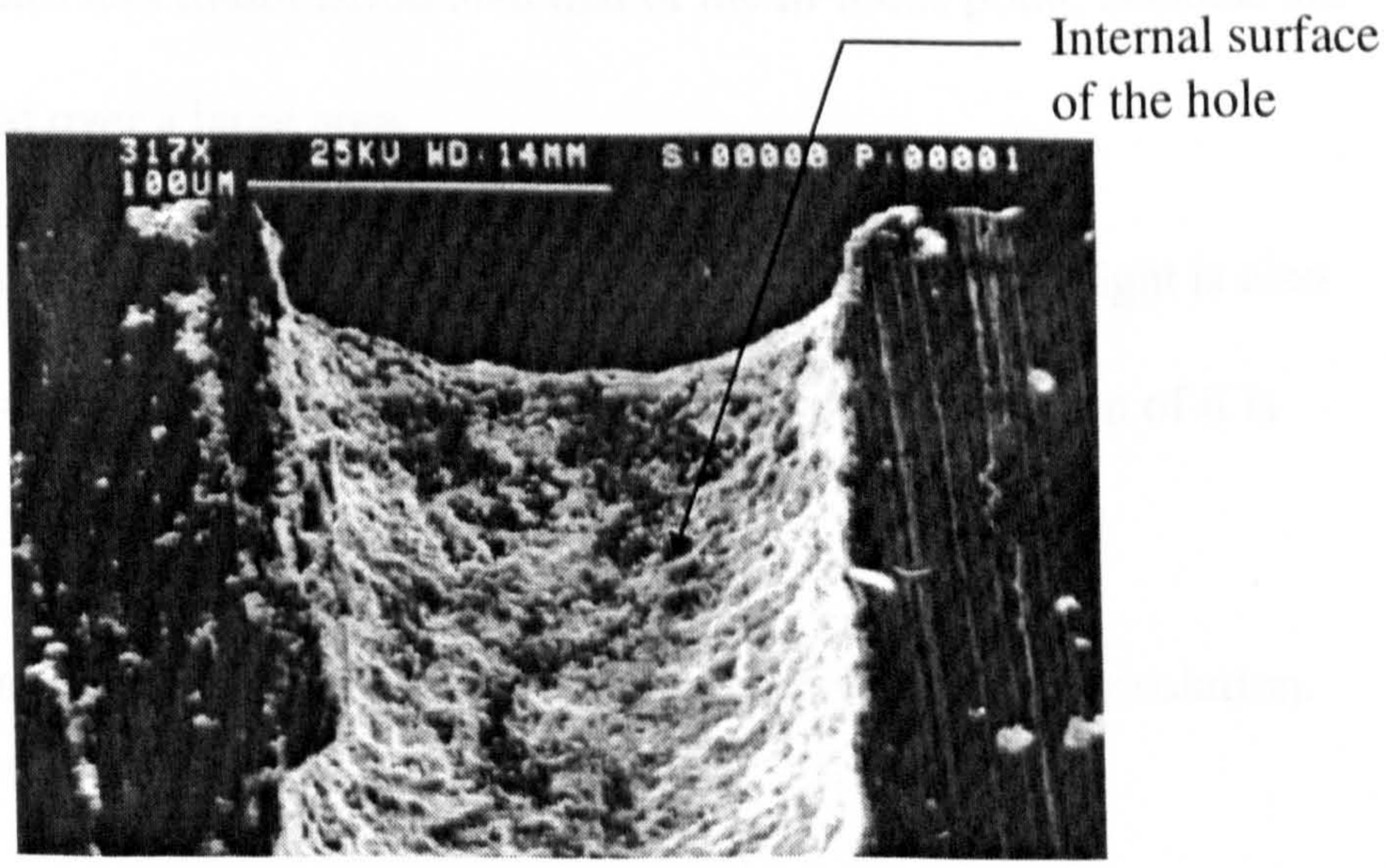

Figure 1-8 A SEM image of the internal surface of the hole

1.7 Confocal microscope and its limitation for measurement.

The confocal microscope is a sub-wavelength high resolution Scanning Optical Microscope (SOM) [50]. Figure 1-9 is an illustration of the basic principle of the confocal microscope (The figure is provided by Lance Ladic, Department of Physiology, University of B C, Canada [51]). It can be seen that unlike conventional microscopes, two pinholes are used. One of them is placed in front of the light source and the other is in front of the image plane. Both of the holes are focused to the same point on the object plane, as the word "confocal" indicates. The two-pinhole arrangement is the key factor of the high resolution. The pinhole in front of the light source only lets the object be illuminated with enough light at the focus point, whilst the pinhole in the image plane only lets the light which is reflected back from focus point be detected. Therefore the received light from the out-of-focus surface is reduced by the two pinholes in the following ways.

1) The surface has less illumination than that of the in-focus point, because the light is spread over a large area.

2) Not all the light reflection can be received by the detector. The light is also spread over a large area at the detection plane and a large fraction of it is blocked by the pinhole.

This double limitation lets the system achieve the sub wavelength resolution.

Unfortunately, when a confocal microscope was used to measure the internal dimension of the holes, it failed. The reflected light was too weak to be detected by the system. There are possible two reasons:

1) The light illuminates the internal hole surface with a large oblique angle (about 80^0), the backward reflection therefore is very weak, as shown in Figure 1-10 (a). Transmission confocal microscope is not suitable for this measurement, because only one end of the hole can be viewed freely.

2) Not all the illuminating light can reach the focus point on the internal surface, approximately 50% is blocked by the part of the hole which is above the focus point. It is represented in Figure 1-10 (b).

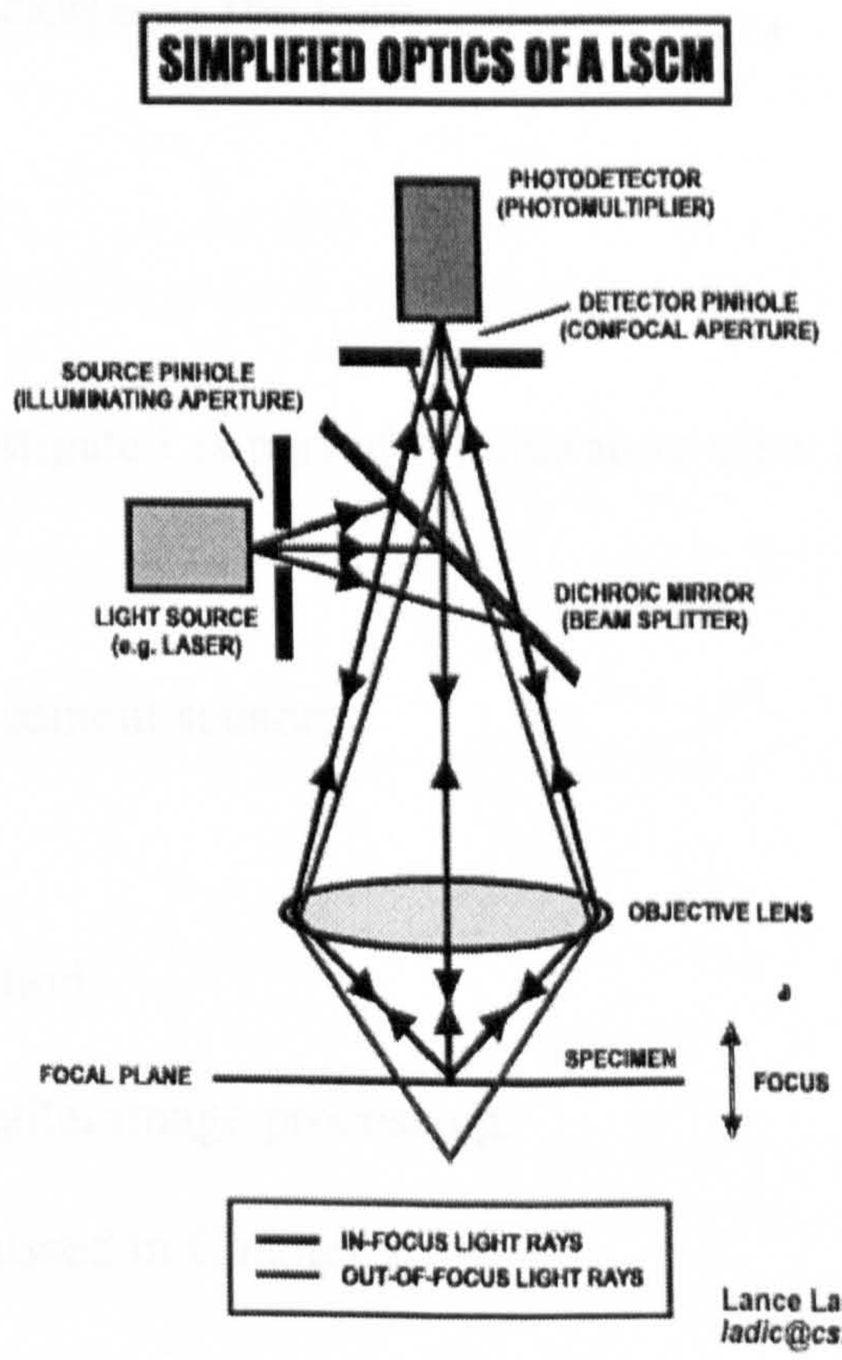

Figure 1-9 An illustration of confocal microscope

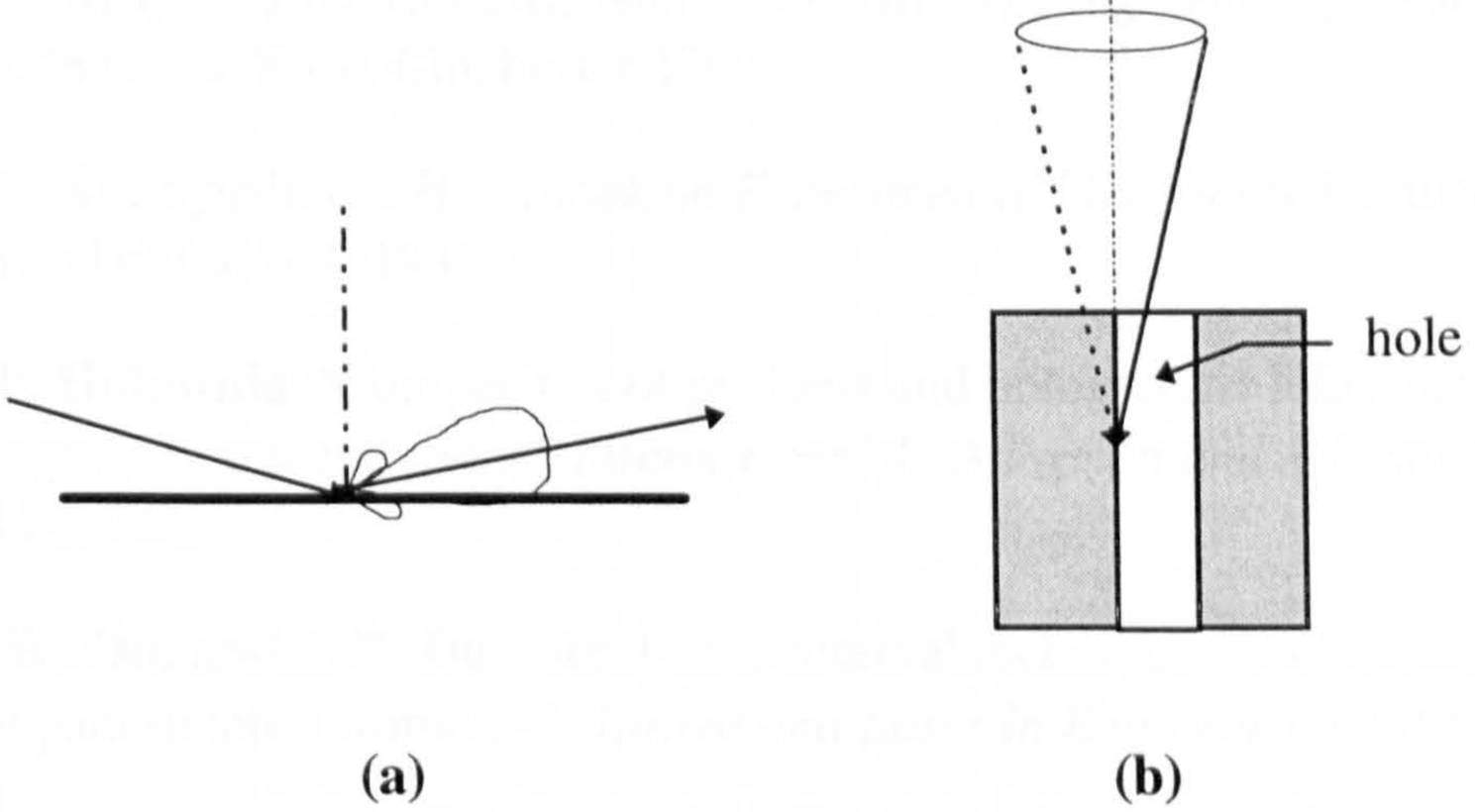

Figure 1-10 Two reasons for weak back scattering (a) The angle distribution of scattering, (b) Blockage by the hole.

1.8 Summary

Several methods investigated as part of the literature view looked possible for the project. They are:

1) optical fibre displacement sensor;

2) optical follower;

3) interferometry method;

4) microscopy and digital image processing.

They are further discussed in Chapter 2.

References:

[1] **F. T. Farago** *Handbook of dimensional measurement* Industrial Press inc. 2nd ed. New York, N.Y. 1982

[2] **H. Dagnall** *Let's Talk Roundness* Rank Taylor Hobson Limited 2nd ed. Leicester England1984

[3] **D. E. Bray and D. McBride** *Non-destructive Testing Techniques* John Wiley & Sons, Inc New York, Chichester 1992

[4] **A. S. Kobayashi** edt *Handbook on Experimental Mechanics* Prentice-Hall, Inc Englewood cliffs, N.J. 1987

[5] **B. P. Holownia** "Comparison of peel test and holographic NDT method for water ingress into metal joints" *International J. Adhesion and Adhesives* **12**(4) 241-244 (1992)

[6] **Y. W. Qin and J. B. Dai** "Real-time interval technique for electronic shearing speckle pattern interferometry" *Optical and Laser in Engineering* **21**(2-3) 241-248 (1994)

[7] **P. Ferraro, A. Ferraiuolo, S. I. Imaparato, C. Voto and K. A. Stetson** "On the holographic detection of core-to-skin disbonds in composite sandwich structures" *Materials Evaluation* **52**(12) 1376-1381 (1994)

[8] **S. F. Burch and P. F. Lanwrence** "Recent advance in computerised X-ray tomography using real-time equipment" *British Journal of Non-Destructive Testing* **34**(3) 129-133 (1992)

[9]**K. S. Tan, Z. G. Li and S. F. Chen** "Soft -X-ray TV microscope developed in China for NDT" *NDT & E International* **27**(1) 11-14 (1994)

[10] **M. L. Jan, C. Y. Chen, C. K. Yen T. R. Yeh and M. .T. Wang** "3D image-reconstruction using cone-beam tomography" *NDT & E International* **27**(2) 83-87 (1994)

[11] **H. Berger** "Trends in Radiologic NDT" *Materials Evaluation* **52**(11) 1248-1256 (1994)

[12] **R. Loveman, J. Bendahan, T. Gozani and J. Stevenson** "Time-of-flight fast-neutron radiography" *Nuclear Instruments & Methods in Physics Research Section B - Beam Interactions with Materials and Atoms* **99**(1-4) 765-768 (1995)

[13] **S. K. Murphy** "Ultrasonics used to examine channel tunnel pipework" *Insight* **37**(6) 450-451 (1995)

[14] M. A. Ward and B. W. Langan "*Strength evaluation of in-situ concrete by rebound hammer and core testing*" *Cement Concrete and Aggregates* **16**(2) 181-185 (1994)

[15] M. Druce and D. W. M. Brereton "A new development in NDT relating to submerged-arc welded pipe" *Insight* **36**(11) 857-862 (1994)

[16] B. Konstantellos and E. Sideridis "The effect of plasticizer on the mechanical and acoustical properties of epoxy polymers" *Plastics Rubber and Composites Processing and Applications* **22**(5) 261-267 (1994)

[17] U. Engel, M. Schwind and S. Stancuniederkorn "New applications of nondestructive testing in metal-forming technology" *J of Engineering Manufacture* **208**(4) 259-267 (1994)

[18] R. Hickling and S. B. Ye "Use of form-function analysis in automated ultrasonic nondestructive testing of composite structures" *Materials Evaluation* **52**(11) 1300-1305 (1994)

[19] E. C. J. N. Dejong, J. G. Duchatinier and J. J. M. Vannisselroij "A straightforward ultrasonic technique for the inspection of adhesively bonded connections and sizing of impact damage in GRP pipelines" *Insight* **36**(9) 683-685 (1994)

[20] R. C. Owen, A. M. Stansfield, A. L. Mcnulty and A. Cheshire "Ultrasonic inspection of complex-geometry components for the sizewell-b preservice inspections" *Insight* **36**(4) 233-236 (1994)

[21] A. Lhemery and R. Raillon "Impulse-response method to predict echo responses from targets of complex-geometry .3. Application to nondestructive testing" *J. the Acoustical Society of America* **95**(4) 1801-1808 (1994)

[22] T. G. Àlvarezarenas, E. R. Desarabia and J. A. Gallegojuarez "Ultrasonic evaluation of creep damage in steel" *Ultrasonics* **31**(3) 155-159 (1993)

[23] C. E. Bull, K. A. Stacey and R. Calcraft "On line Weld Monitoring using ultrasonics" *British J. Non-Destructive Testing* **35**(2) 57-64 (1993)

[24] T. M. Hsieh and M. Rosen "Ultrasonic leaky waves for nondestructive interface characterization" *Ultrasonics* **31**(1) 45-51 (1993)

[25] N. M. Carlson, J. A. Johnson, L. A. Lott and D. C. Kunerth "Ultrasonic NDT methods for weld sensing" *Materials Evaluation* **50**(11) 1338-1343 (1992)

[26] R. Kazys and L. Svilainis "Analysis of adaptive imaging algorithms for ultrasonic nondestructive testing" *Ultrasonics* **33**(1) 19-30 (1995)

[27] I. Dunlop and A. McNab "Shape classification of flaw indications in 3-dimensional ultrasonic images" *IEE Proceedings-Science Measurement and Technology* **142**(4) 307-312 (1995)

[28] C. Delebarre, C. Bruneel, R. Delwiche and I. Dayos "Polycrystalline diamond cutting element control using high-frequency c-scan image-processing" *NDT & E International* **26**(6) 303-308 (1993)

[29] L. Capineri, H. G. Tattersall, J. A. G. Temple and M. G. Silk "Time-of-flight diffraction tomography for NDT application" *Ultrasonics* **30**(5) 275-288 (1992)

[30] D. J. Whitehouse *Handbook of Surface Metrology* IOP Publishing Bristol, Endland1994

[31] G. Schmalz *ZVDI* **73** 144-161 1929 (from [1])

[32] C. Ming, D. S. Wan "Online automated phase-measuring profilometry" *Optics and Lasers in Engineering* **15**(2) 127-139 (1991)

[33] M. Suganuma, T. Yoshizawa "3-dimensional shape-analysis by use of a projected grating image" *Optical Engineering* **30**(10) 1529-1533 (1991)

[34] E. Liasi , W. P. T. North "Retroreflective moire deflectometry - Phase and specular object inspection" *Optical Engineering* **33**(4) 1200-1205 (1994)

[35] R. Rodriguezvera "3-dimensional gauging by electronic moire contouring" *Revista Mexicana de Fisica* **40**(3) 447-458 (1994)

[36] T. Pfeifer, B. Wang, J. Evertz, R. Tutsch "Phase-shifting morie deflectometry" *Optik* **98**(4) 158-162 (1995)

[37] C. Wykes , R. Morshedizadeh "Surface-Topography measurement using digital moire contouring - errors and limitations" *Proc. the Inst. of Mech. Eng. Part B - J. Engineering Manufacture* **209**(4) 317 - 325 (1995)

[38] J. C. Dainty *Laser Speckle and Related Phenomena* 2nd ed. Spinger-Verlag, Berlin 1984

[39] S.G. Lipson, H. Lipson and D.S. Tannhauser *Optical Physics* Cambridge Univ. Press Cambrdge UK 3rd 1992

[40] D. P. Hand, T. A. Carolan, J. S. Barton and J. D. C. Jones "Profile measurement of optically rough surface by fiberoptic interferometry" *Optics Letters* **18**(16) 1361-1363 (1993)

[41] Y. Surrel and B. Zhao "Phase-stepping: Application to high-resolution moire" *SPIE* **2003** (Interferometry VI) 159-170 (1993)

[42] P. C. Montgomery, J. P. Fillard, M. Castagne and D. Montaner " Phase-stepping microscopy (PSM) - A qualification tool for electronic and optoelectronic devices" *Semiconductor Science and Technology* **7**(1A) A237-242 (1992)

[43] M. Dupuy *Proc. I. Mech. Engrs.* **182**(Pt. 3k) 255-259 1967/68

[44] P. Beckman and A. Spizzichino *The Scattering of Electromagnetic Radiation from Surface* (Oxford: Pergamon) 1968

[45] J. A. O'Keefe *U.S. Army Mapping Service* 1956. (From [1])

[46] P. Beckmann and A. Spizzichino *The Scattering of electromagnetic waves from rough surfaces* Oxford Pergamon 1963

[47] F. G. Bass and I. M. Fuchs *Wave scattering of electromagnetic waves from rough surfaces* MacMillan New York 1963

[48] O. C. Wells *Scanning Electron Microscopy* McGraw-Hill Book Company 1974

[49] I. Sherrington and E. H. Smith "Modern measurement techniques in surface metrology: Part 1: Stylus instruments, electron microscopy and non-optical comparators" *Wear* 271-288 (1988)

[50] T. Wilson and C. Sheppard *Theory and Application of Scanning Optical Microscopy* Academic Press 1984

[51] Lance Ladic http://www.cs.ubc.ca/spider/ladic/ confocal.html

2. History of method of approach

In order to measure the internal dimensions of holes, the optical follower and interferometry method have been combined with optical fibres. These tests are described in section 2.1. The conventional microscope, CCD camera and digital signal processing technique are used in the final approach. The whole system is described in section 2.4. Section 2.5 describes the verification of the measuring technique.

2.1 Internal fibre optic measurements

2.1.1 Optical fibre displacement measurement

A solution for the small hole measurement could be to use an optical fibre displacement sensor [1]. The objective was to measure the profiles of the internal surface along a series of lines parallel to the axis of the hole, from these the dimension of the hole should then be deduced. An examination of displacement sensors[2] is shown in Figure 2-1 (a). In this figure, fibre 2 was used to illuminate the surface and fibre 1 was used to receive the reflected light. Only the light which reaches the effective area can be received by the fibre 1. The proportion of the effective area changes with *d*, the distance from the end of fibre to the surface. Therefore as the *d* changes, the intensity collected by fibre 2 also changes. This phenomenon is used for displacement sensor. In order to measure the internal dimension, it is suggested [1] that the end of both fibre should be angled, as shown in Figure 2-1(b).

However, the hole is very small (200 μm) and the surface is not smooth. It is found necessary to reduce the size of fibre so that it could be inserted into the hole. It is also necessary to reduce the light focus spot on the surface to increase the accuracy. A single fibre and lens system has therefore been considered. This system has been evaluated by combined with optical follower and interferometry method for the small hole measurement.

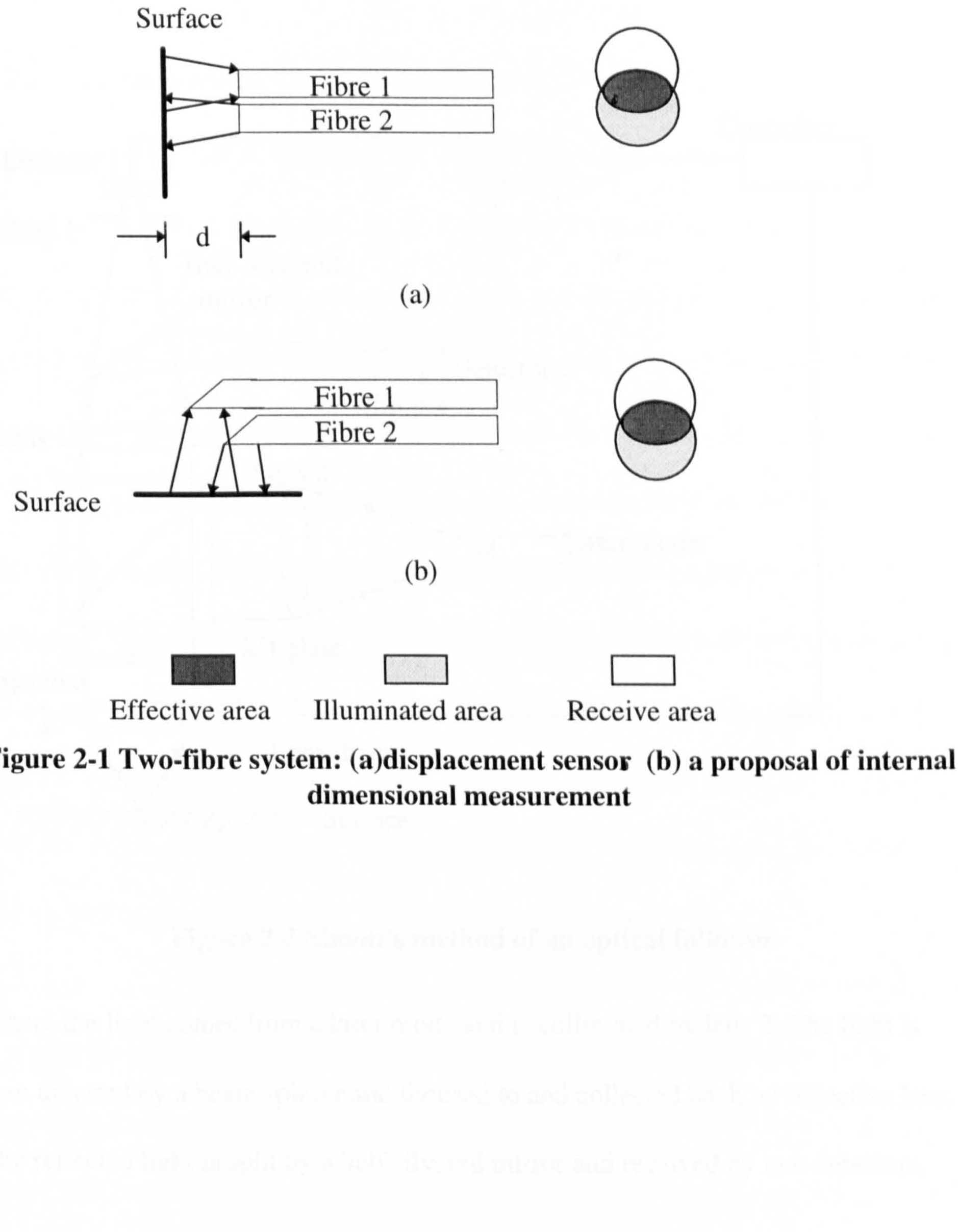

Figure 2-1 Two-fibre system: (a)displacement sensor (b) a proposal of internal dimensional measurement

2.1.2 Optical follower profilometer and its use with fibre optics

2.1.2.1 Optical follower

The principle of an optical follower is that, as given in section 1.5.4 (p.14), with the help of feedback system, the probe of the instrument is forced to follow the profile of the surface during the scanning. Therefore the position of the probe gives the profile of the surface. One of the methods is given by Simon[3] as shown in Figure 2-2.

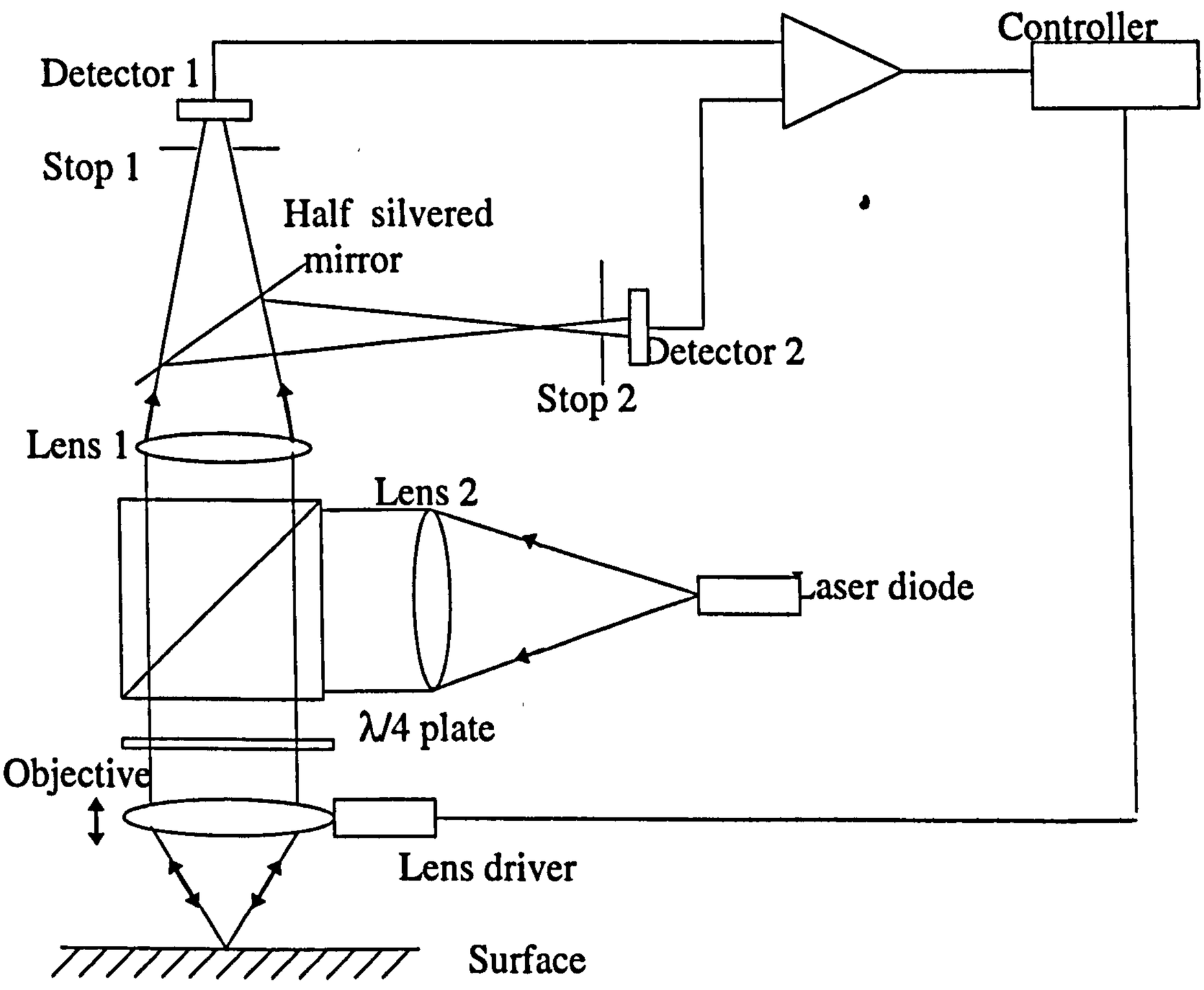

Figure 2-2 Simon's method of an optical follower

Where the light comes from a laser diode and is collimated by lens 2. The light is then diverted by a beam splitter and focused to and collected back by objective lens. The reflected light is split by a half silvered mirror and received by two detectors.

Two stops are placed in front of the detectors. Stop 1 is put before the image plane while stop 2 is fixed after the image plane. When the surface moves away from the focus plane, these two detectors give opposite signal changes. This signal controls the lens following the profile of the surface, so that the focus point is kept on the surface. However, the probe of the optical system is at least few ten millimetres, so it is unsuitable for small hole internal measurements without modification.

2.1.2.2 Two dimensional scanning profilometer

It is because of the size of the probe that optical followers cannot be used directly for internal measurement. A possible method considered was to use a single optical fibre to carry both the illuminating and reflected light into and out of the hole as shown in Figure 2-3. The sketch (a) in Figure 2-3 is the proposed system where a laser source is used. The light is delivered to and collected back by the same fibre. It is separated by a fibre splitter. At the end on the fibre a lens is used to focus the light into a small point on the surface. However a single fibre cannot produce an image, there is no "follower". Instead of following the surface profile, the probe is driven to scan along the normal direction of the surface. Similar to a confocal microscope, the received signal is a maximum when the surface just locates in the focus point. The distance from the lens to the surface can therefore be found. By scanning along the surface, a surface profile can be generated.

A simple system was assembled to test the principle, as shown in Figure 2-3 (b). Figure 2-4 is a profile measurement made by the testing system. The measuring length is 0.1 mm and the height range is from 0.02 to 0.14 mm. Figure 2-5 shows a

profile measured by a stylus on the same surface. The measuring length is 2 mm and the height range is from -0.107 to 0.096 mm. Because of the difficulty in making these two measurements along the same profile, a direct comparison between these two results proved to be very difficult. A further study needs to use statistical analysis as it is used in Chapter 5 to analyse same problem.

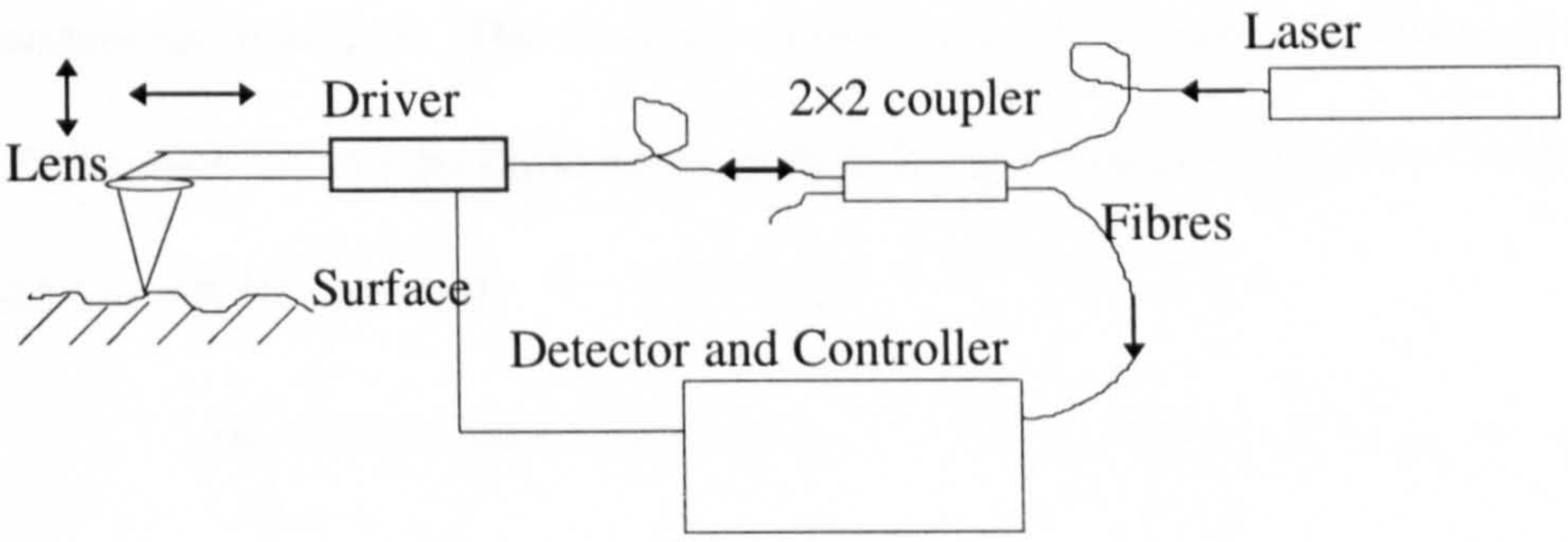

(a)

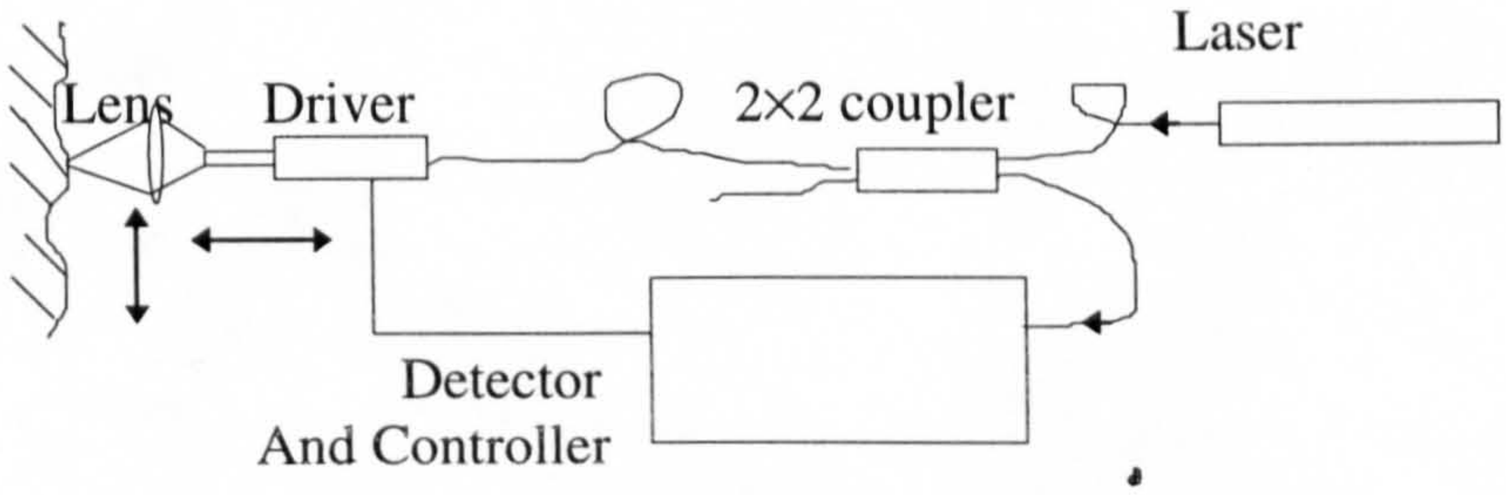

(b)

Figure 2-3 A 2-D scanning profilometer: a) For internal measurement b) For principle test

Unfortunately, the following disadvantages make the method unsuitable for small hole measurement:

1) It was not possible to find a supplier who could make an angled fibre end (45^0) and mount the microlens on it, even though this process has been reported in the literature of the manufacture of microlenses [4]-[8].

2) Because the microlens technique is not presently obtainable, this kind of probe is very expensive. In order to protect it from damage during the measurement, the servo system would have to be delicate and expensive.

3) The processing speed could be very slow as it is basically a point measurement.

However, if the internal space is not so small (bigger than 10 mm), the method has a measurement potential. The accuracy of this method depends on the sensitivity of the light detector. An oscilloscope is used in the test mentioned above. An accuracy of 25 μm can be achieved.

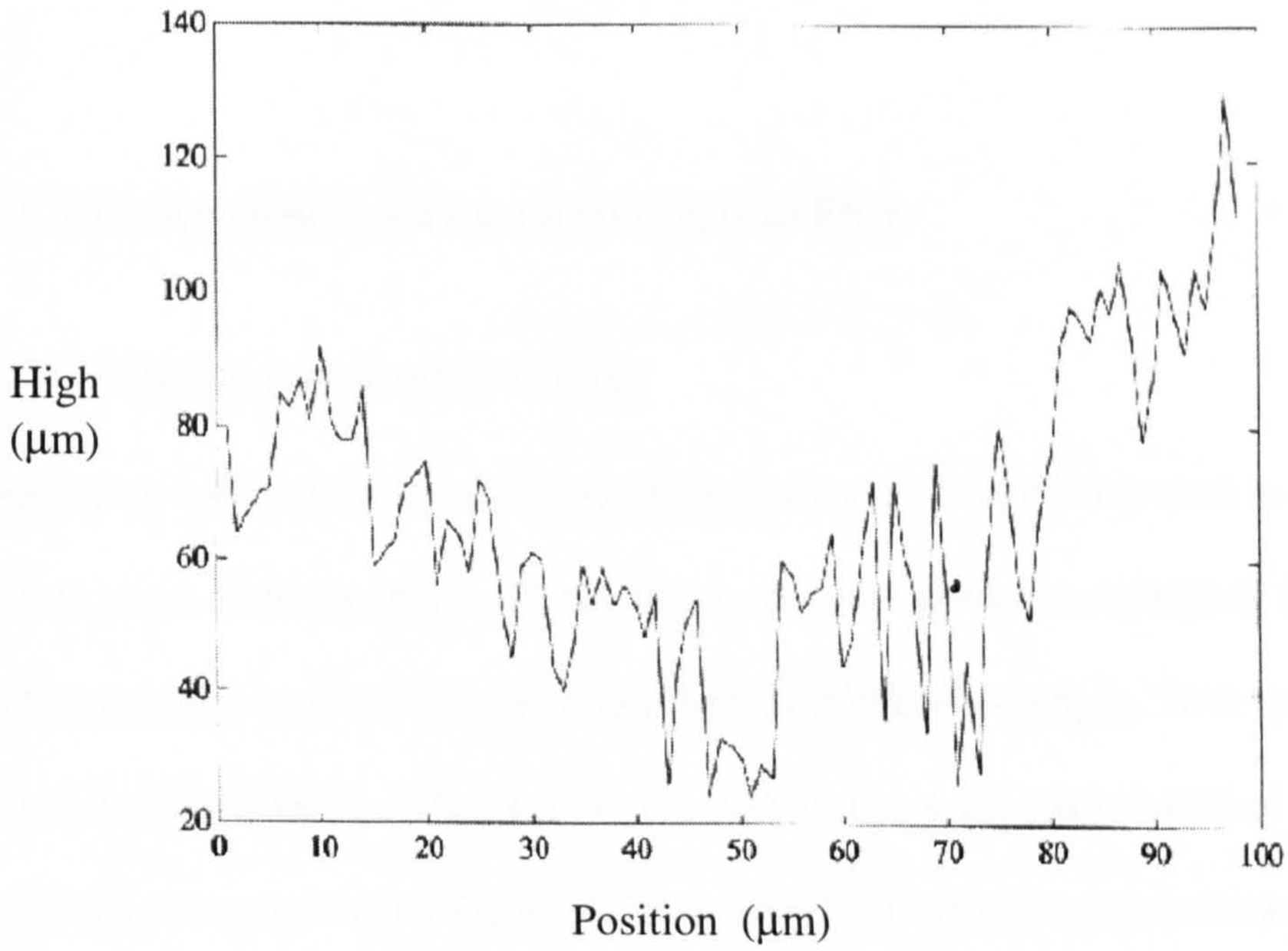

Figure 2-4 One of the profiles measured by the optical system, the total measuring length is 0.1 mm and the height range is from 0.02 to 0.14 mm

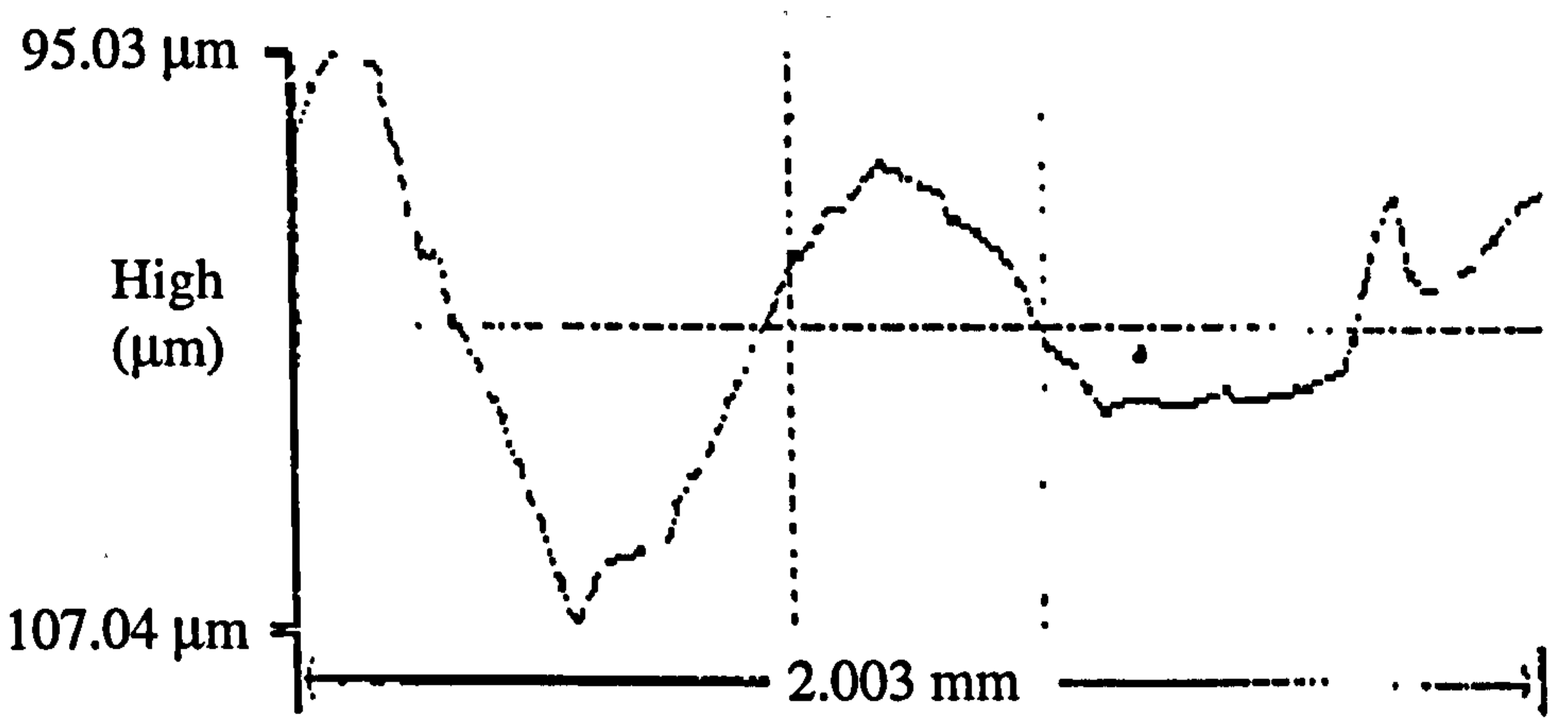

Figure 2-5 The profile measured by stylus, the total measuring length is 2.0 mm and the height range is from -0.107 to 0.096 mm.

2.1.3 Interferometry and its use with optical fibre

2.1.3.1 Interferometric measurement

Interference methods have a relatively long history, and have been used in metrology in many ways. Newton rings and Michelson interferometry are examples. The resolution of the methods is approximately half of the wavelength. With the help of phase sensitive detection, the heterodyne method can reach a resolution of a hundredth of a wavelength. Figure 2-6 is a variant of Michelson interferometer used for surface measurement. The coherent light beams reach to and reflect back from either the surface or reference plane to the detector. An interference fringe pattern can be detected. From the interference fringe pattern the relative height of the surface can be measured. A heterodyne system is more complicated than the direct Michelson approach, as the frequency of one beam is changed in the range of 2 - 100 MHz.

When these two beams meet, a 2 - 100 MHz beat frequency signal can be received. The surface profile can then be measured by detecting the phase shift of the signal.

Although the method looks promising for an 'open' surface, it is not applicable for internal surface measurement without modification.

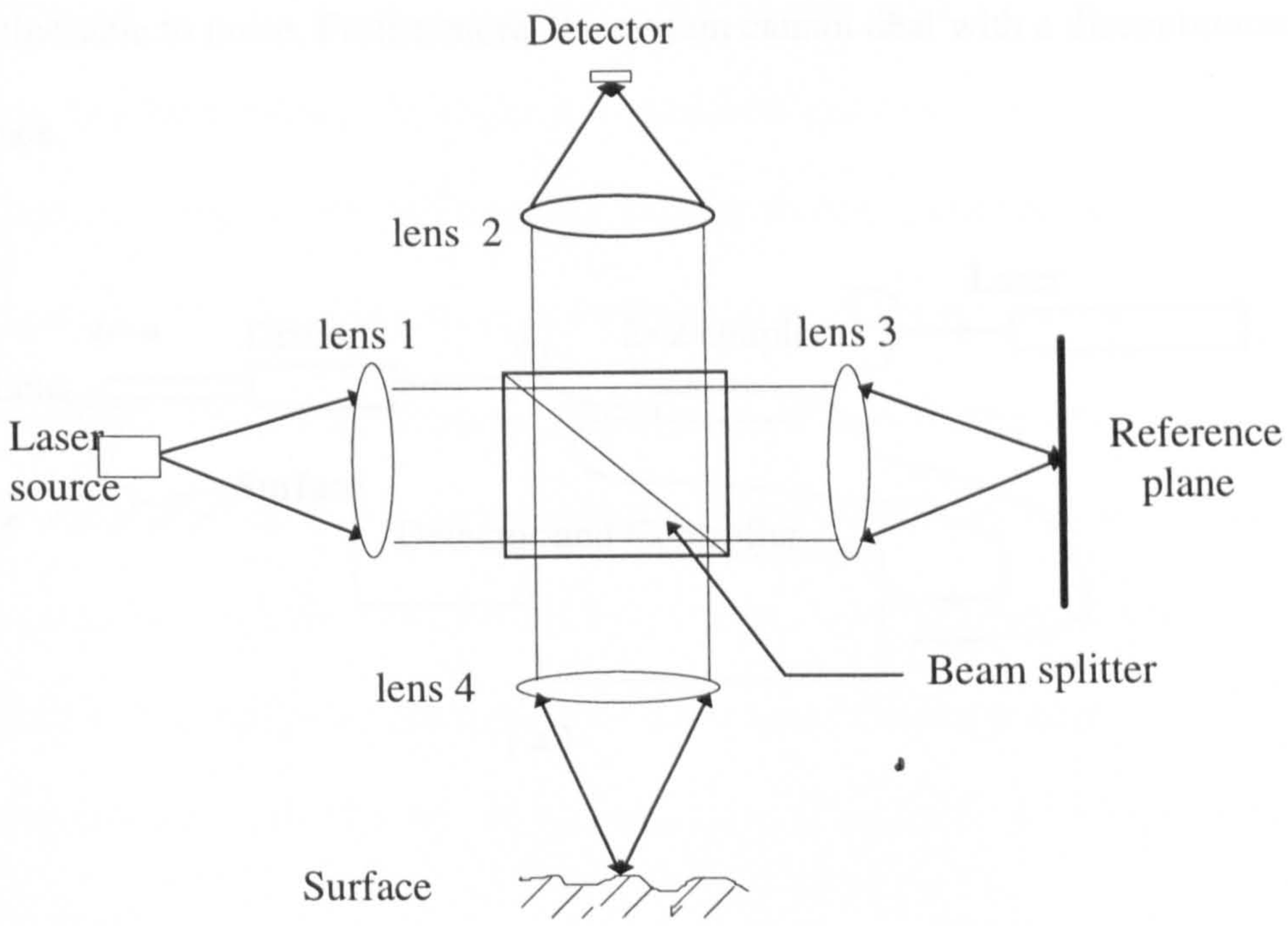

Figure 2-6 A Michelson interferometer for surface measurement

2.1.3.2 Interferometry with optical fibre

In the same way that an optical fibre modification can be applied to the optical follower, the interferometry method can also be coupled with an optical fibre system as shown in Figure 2-7. With the help of a 2×2 fibre coupler, a Michelson

interferometry system was set up. The laser beam is split by the optical fibre coupler. One light beam is sent to the surface. The other is delivered to the detector as a reference where it meets the reflected light from the surface. An arm of the optical fibre coupler is used to send the light to and collected light reflected back from the surface. An interferometric fringe pattern is generated on the detector. When the distance between the surface and the probe changes a fringe shift can be observed. This method needs only a one dimension scan axis, but due to scattering, the system is vulnerable to noise. Furthermore, the system cannot deal with a discontinuous surface.

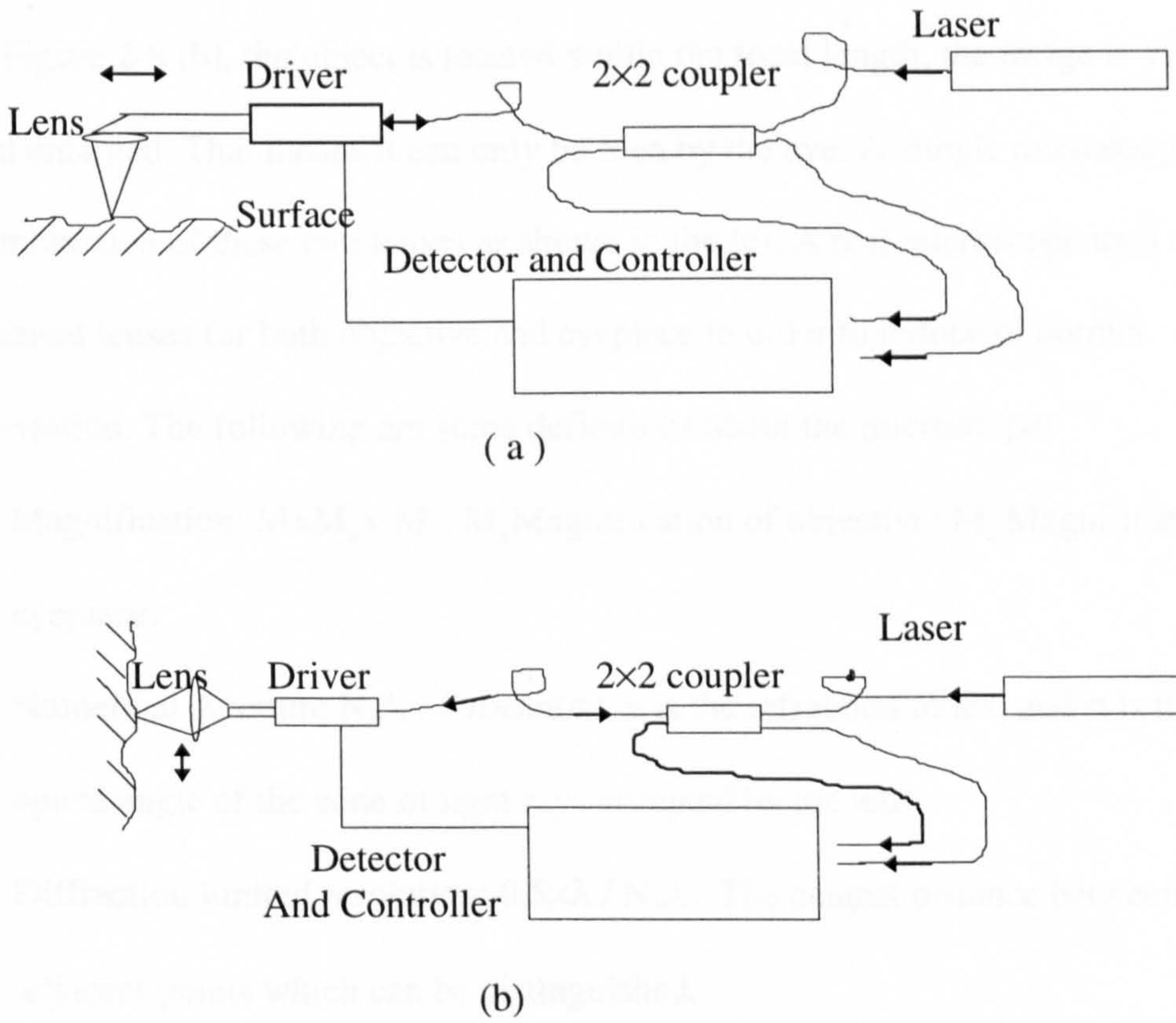

Figure 2-7 Optical fibre interferometry: (a) for internal measuring use (b) for principle testing

2.2 Optical microscopy

2.2.1 The optical microscope [9][10]

From a single lens a magnified image can be seen. It is shown in Figure 2-8 (a) and (b). The relationship of object distance d_o, image distance d_i and focus length f is:

$$\frac{1}{d_o}+\frac{1}{d_i}=\frac{1}{f} \qquad 2.1$$

As shown in Figure 2-8, when $d_i > 0$ the image is real, while $d_i < 0$ the image is virtual. In Figure 2-8 (a), the object is located between one to two focal lengths from the lens, the image is real and enlarged. In other words, is can been seen on a screen. In Figure 2-8 (b), the object is located within the focal length, the image is virtual and enlarged. That means it can only be seen by the eye. A simple microscope is the combination of these two lenses as shown in the (c). A real microscope uses multi-element lenses for both objective and eyepiece in order to reduce or correct aberration. The following are some definitions about the microscope:

- Magnification: $M=M_o \times M_e$. M_o Magnification of objective; M_e Magnification of eyepiece.
- Numerical Aperture N.A.: = $n \times \sin(\alpha)$. n is the refraction index, and α is the half apical angle of the cone of light rays accepted by the lens.
- Diffraction limited resolution: $0.5 \times \lambda$ / N.A. The nearest distance between two adjacent points which can be distinguished.
- Depth of the field (DOF): The clear focused depth of the microscope.
- Working distance: The clearance between the end of object and the focal plane.

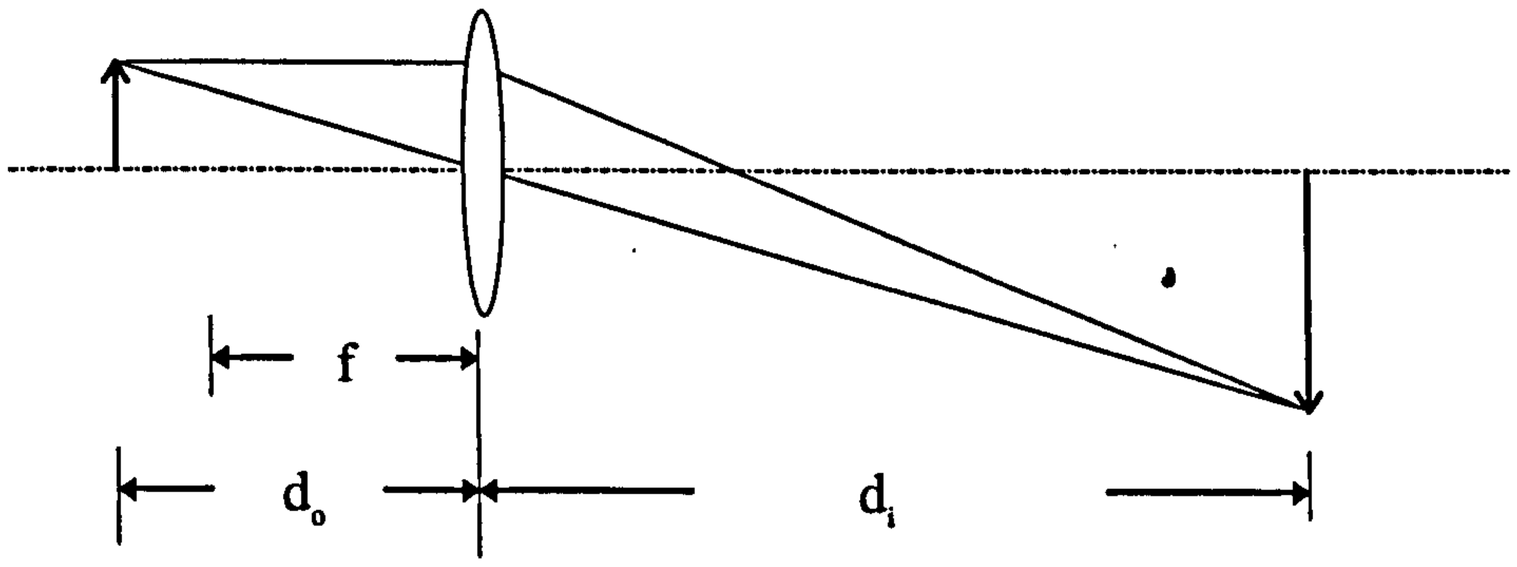

(a)

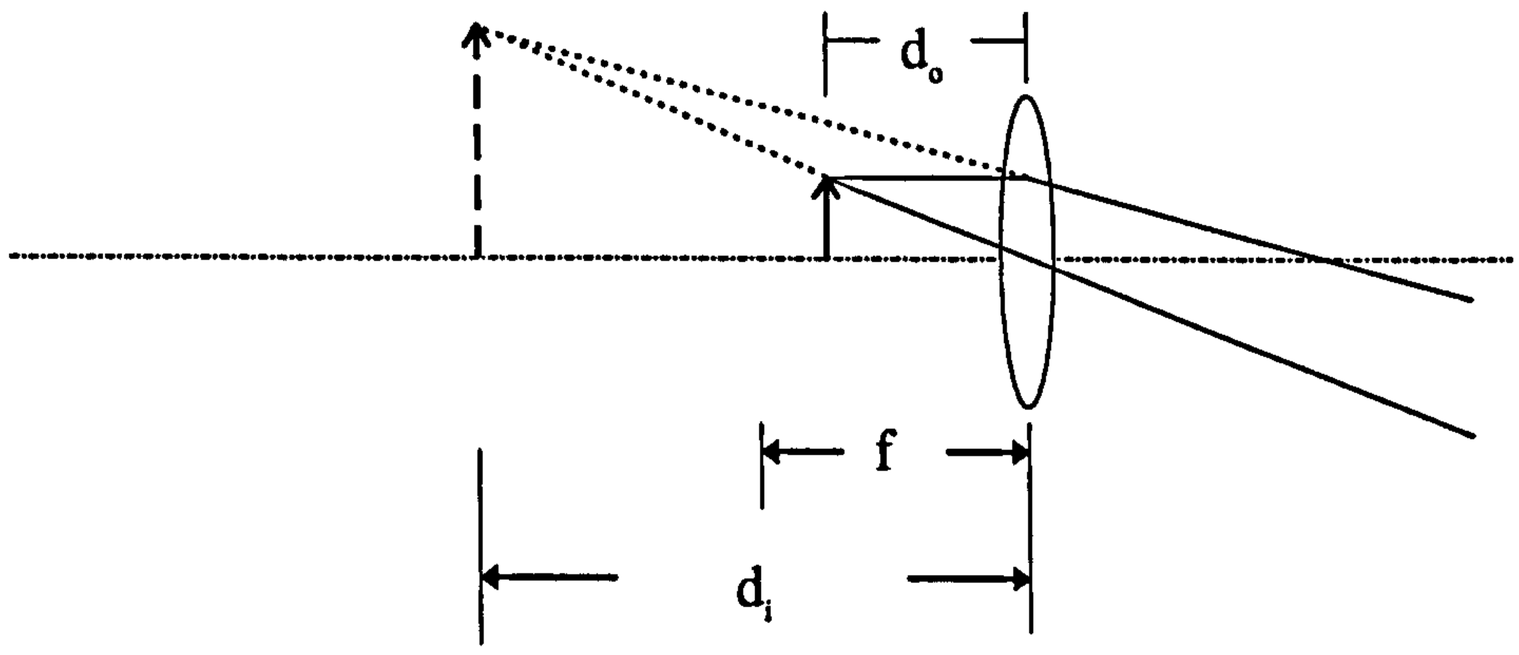

(b)

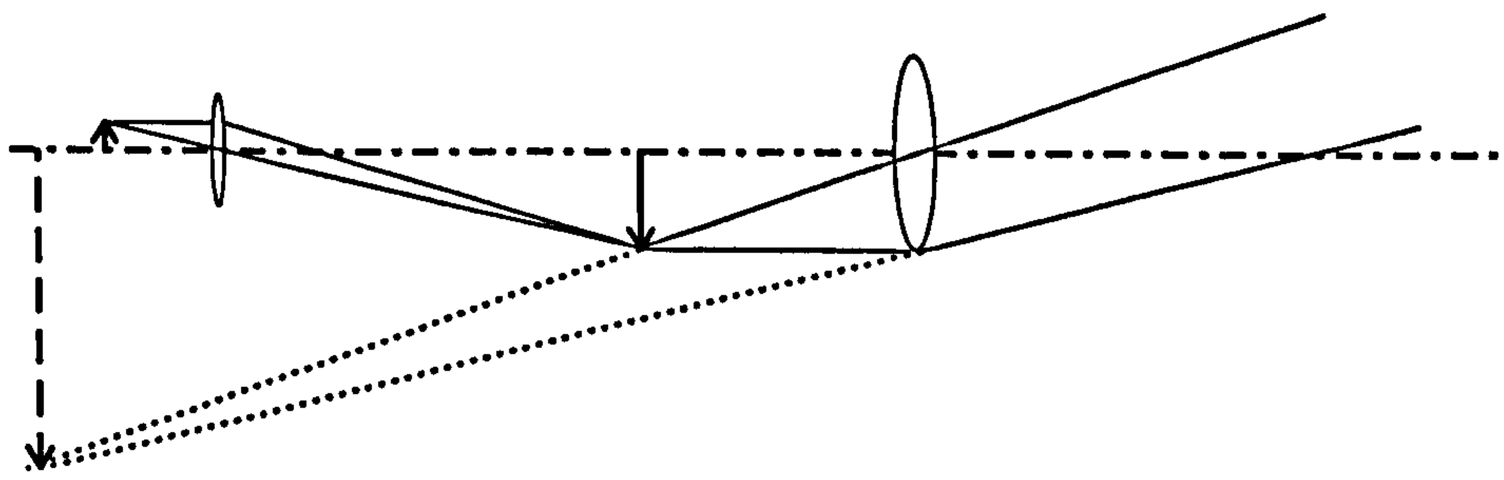

(c)

Figure 2-8 Illustration of microscope

2.2.2 Use of microscope

Figure 2-9 shows the use of microscope in small hole measurement. Figure 2-9(a) shows the tip and holes of the diesel engine fuel injector, considered in section 1.2(p.3). Figure 2-9(b) shows the optical system. The injector is mounted on the stage. The hole is illuminated by a flexible light guide from the restricted end of the hole which is inside the injector. The image of the hole is enlarged by the objective and can be therefore viewed from a CCD camera. Two factors allow the successful use of the microscope:

1) The method of illumination.

2) Having a long working distance objective.

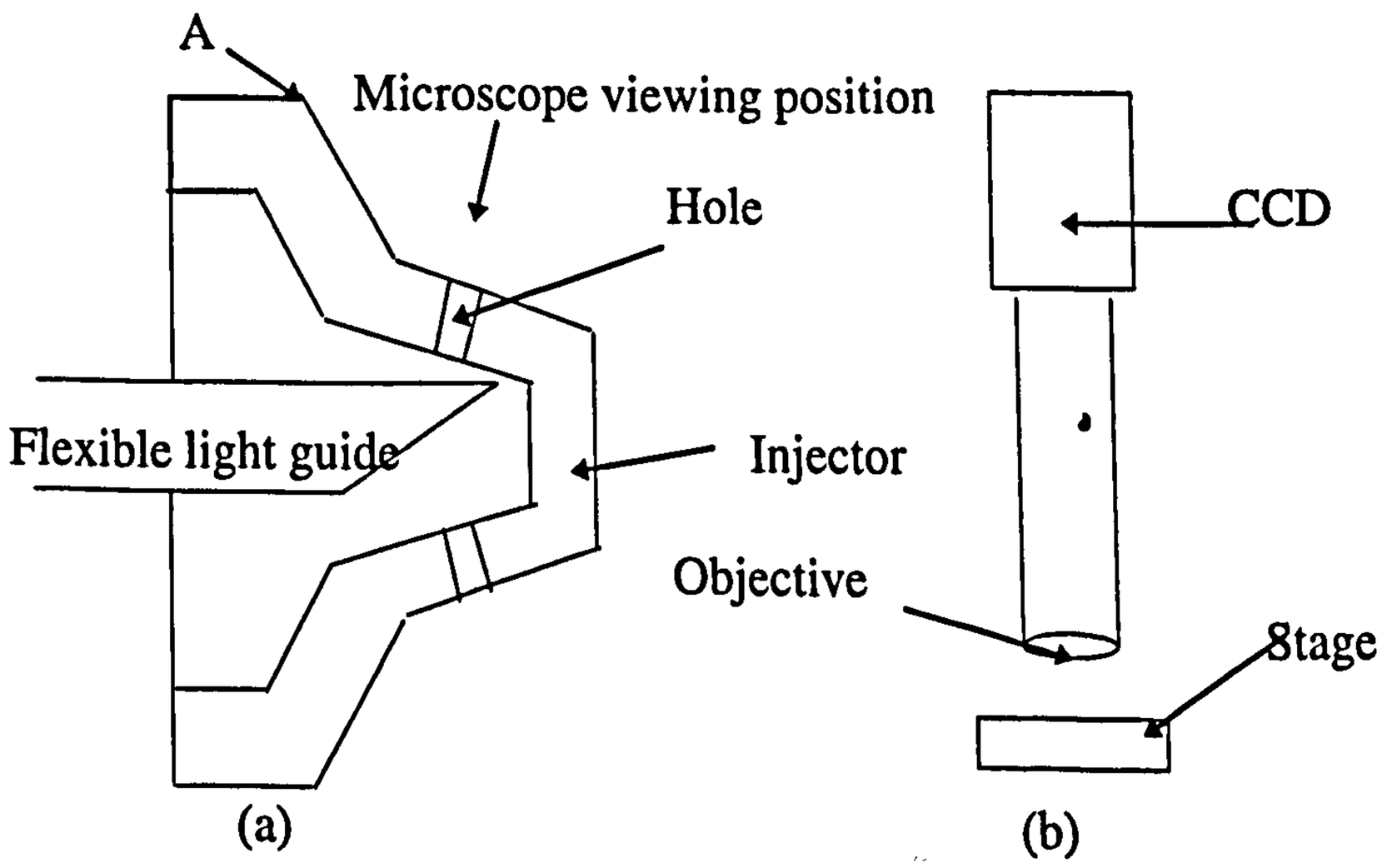

Figure 2-9 (a) Injector and illumination fibre (b) The stage to hold the sample

2.2.2.1 The method of illumination

One end of the hole is not readily available. If the hole is viewed and illuminated from the same side of the hole, nothing can be seen. The reasons are the same as in

the use of confocal microscope(section 1.8, p.26): the hole restricts the illumination and the back scattering light is too weak to be detected. A flexible light guide with an angled end is used to illuminate the internal surface from the restricted end of the hole (inside the injector).

Figure 2-10 illustrates the way to calculate the angle of the flexible light guide end. If β is the angle between the axis of the hole and the axis of the light guide, ϕ is the oblique angle of the end of the fibre and *n* presents the refractive index of the fibre, then:

$$n\sin(\pi/2-2\phi)=\sin(\pi/2-\beta) \qquad 2.2$$

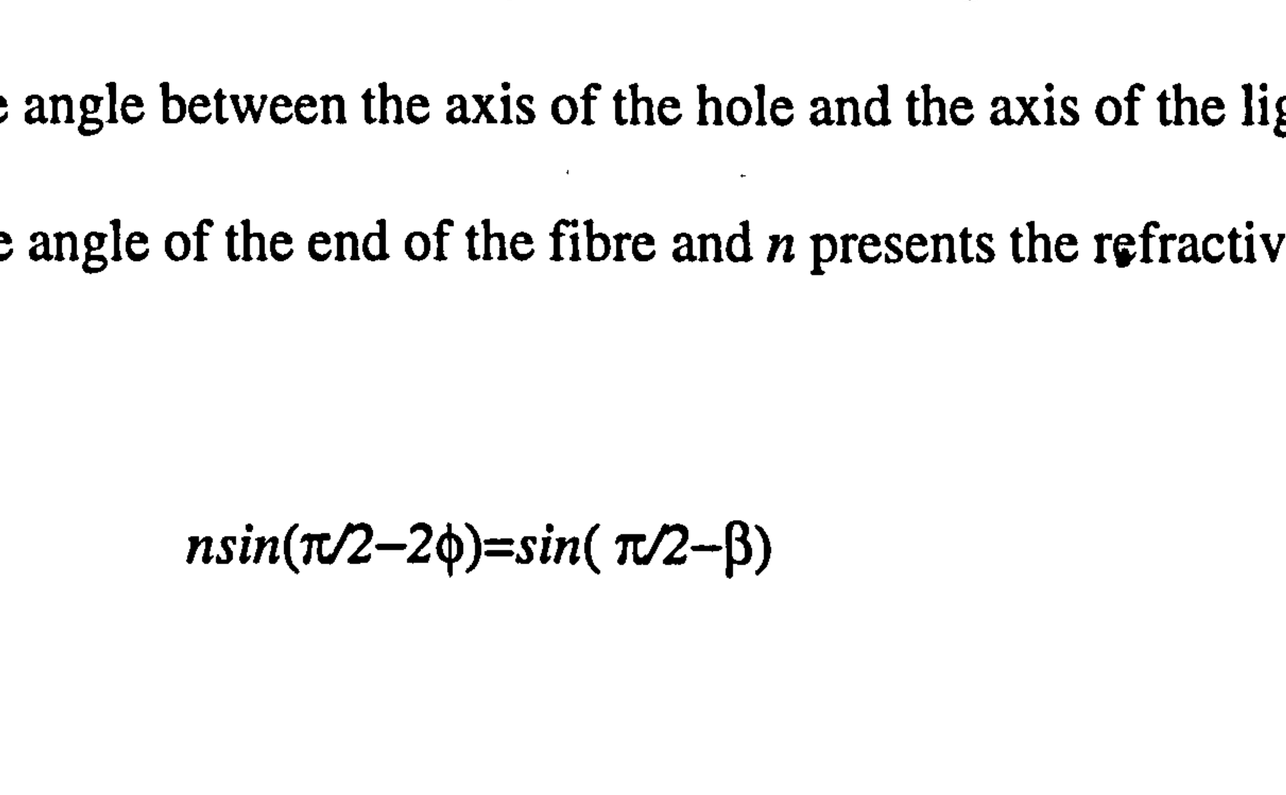

Figure 2-10 (a) General; (b) Relationship of angles

Thus ϕ can be defined by β from following equation:

$$n\cos(2\phi)=\cos(\beta) \qquad 2.3$$

Incoherent light was used to avoid speckle noise and a suitable green light filter was also used to reduce chromatic aberration.

2.2.2.2 Working distance

The microscope objective is restricted by the highest point of the injector (marked A in Figure 2-9 (a)). To overcome this restriction, a long working distance objective is needed. This kind of objective can provide enough clearance between the objective and the hole. An example of this clearance is 6 mm for measuring the injector holes.

2.3 Use of digital imaging

A digital image system has been used to make the measurements automatically. The main components of the system are a Charge Coupled Device (CCD) camera, an Analogue/Digital (A/D) converter, digital frame storage and a computer.

2.3.1 CCD camera

CCD cameras are widely used to capture images. The image is projected on the chip where there are several hundred thousand picture cells which convert the light intensity into an electrical signal. The typical size of each cell is approximately 10 × 10 micrometer. A typical size of the total sensor area of the CCD camera used is 6.4 × 4.8 mm [7].

2.3.2 A/D Converter

The A/D converter used in the system is called PIP board[1]. It is a plug in card which allows a PC computer to capture a video signal from an external source. The total image is converted into a 512×512 pixel matrix with 8 bits grey level. As the size of the CCD chip is 6.4×4.8 mm, the scales of the digital matrices are not equal along two directions. The aspect ratio is 0.707. This factor is important enabling accurate calibration of the system.

2.3.3 Speed of processing

It takes the CCD camera 1/30 second to capture a frame. The PIP card uses the same speed to digitalise the image. To write an image into a hard disc needs less one second for a 486PC 50 MHz computer. The time of image processing varies. It depends on the software language and computer used. For example, to locate the cross section in an image, a C++ programme running in a 486PC is approximately 60 times faster than a MATLAB programme running on Falcon, a computer of the Department of Engineering, University of Warwick. To run the same MATLAB program, Crocus, a computer of the Computer Service , University of Warwick, is at least ten times faster than Falcon.

2.3.4 Resolution

The resolution of the digital system is limited by spatial sampling. Both CCD sensor area and PIP board have a finite number of pixels. The overall system resolution is

---

[1] Matrox Electronic Systems Limited 1055 St. Regis Blud., Dorval, Quebec Canada H9P 2T4

limited by both the optical system and the digital system as it will be shown in section 2.4.5.

2.4 The measuring system

The objective of the hole dimension measurement is to measure the cross sections at different positions of the hole and to add these cross sections together to get the 3-D shape. The cross section measurement is achieved by using the optical sectioning microscopy (OSM) technique. From the OSM an in-focus-strip can be seen. By locating the centre of the strip, the cross section can be found.

2.4.1 Optical sectioning microscopy

Optical Sectioning Microscopy (OSM), a technique which reconstructs a 3-D shape from 2-D images, is used in biological specimen analysis. This technique uses the limited depth of field of the microscope. By focusing on different positions of the specimen, a series of 2-D images can be captured. These 2-D images are then reconstructed into a 3-D picture of the specimen. Reference [11] presents a review about current work(to 1984). The confocal microscope is also used in this area later as reviewed by [12] - [14].

There are two differences between biological specimen analysis and hole measurement:

1) Overlap: In biological specimens analysis the specimen is transparent and the out-of-focus information is superimposed on in-focus information. It is not the case in hole measurement.
2) Information region: In biological specimen analysis the specimen is usually in a large viewing area, while in the hole measurement the in focus surface occurs only in a limited area (annulus-like in-focus-strip).

Therefore a different approach is needed for the hole measurement.

2.4.2 The in-focus-strip

The optical section microscope has been used for this project. The internal surface of the hole is illuminated from the restricted end and viewed from the open end. It has the appearance of a shadow pattern in the image. The form of the shadow pattern is explained in Figure 2-11. It can be seen that the shadow is some sides of the peaks or valleys of the surface which cannot be illuminated directly. Furthermore, when the internal surface is investigated using a microscope, only a small part of the surface locates inside the depth of field. This part of the surface has a clear image while the rest of the surface is blurred. The clear focused part of the surface formed an annulus-like strip in the image, referred to as the in-focus-strip. A typical image is shown in Figure 2-12. The technique for measuring holes now looks possible using the method: if the centre of the in-focus-strip can be located, the cross section at that position of the hole therefore can be found. The hole is moved up or down to create a series of images which represents cross sections of different height position of the hole. A three dimensional shape of the hole can then be reconstructed. It was decided

to move the hole but not the microscope objective, in order that a constant magnification was maintained.

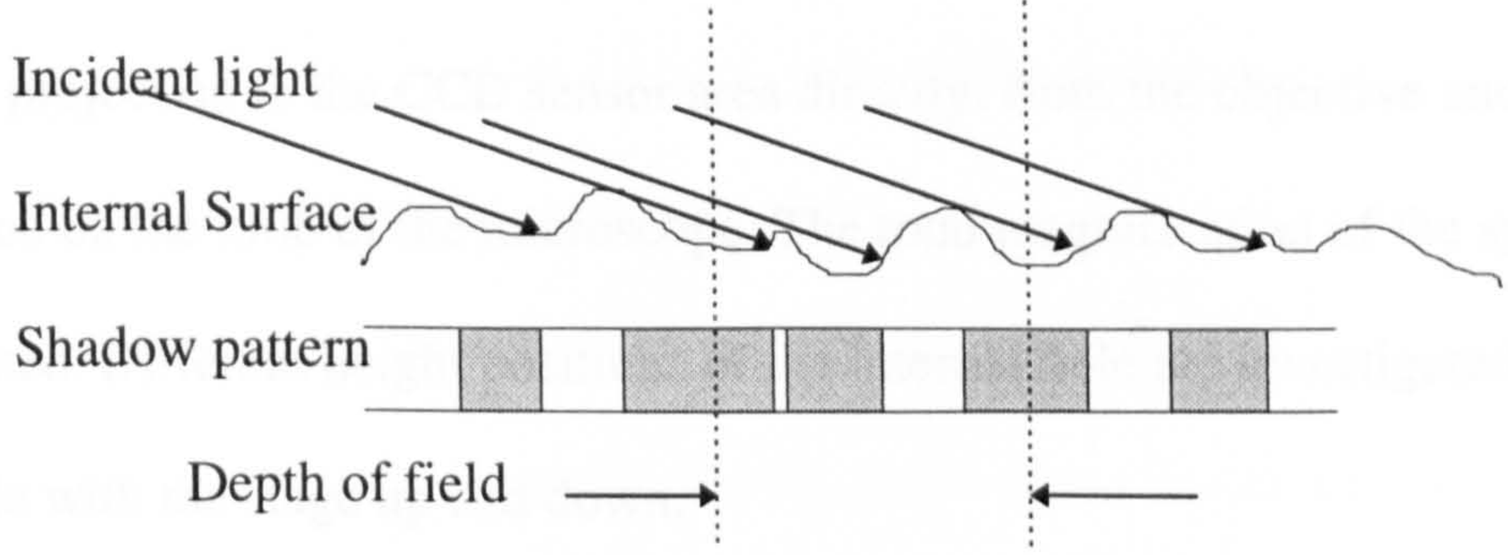

Figure 2-11 2-D shadow pattern and depth of field

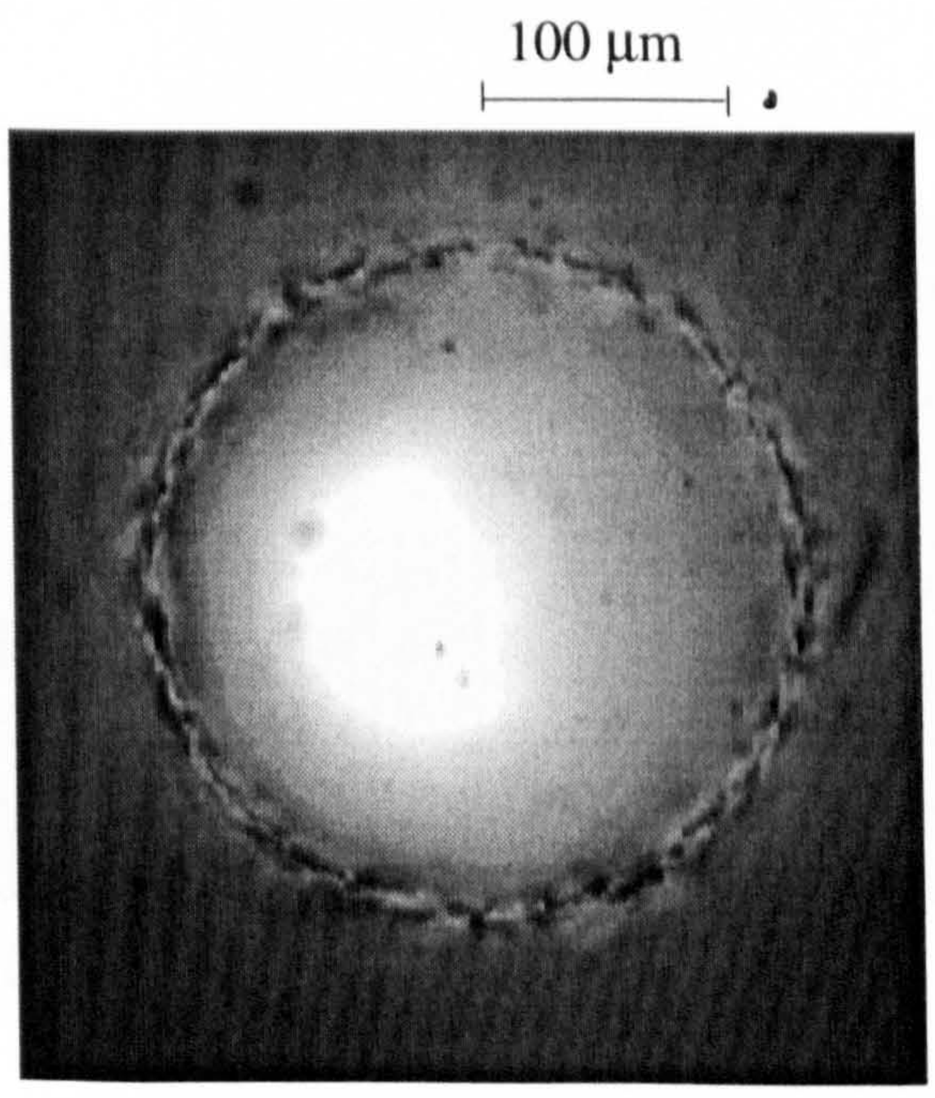

Figure 2-12 An image of the hole

2.4.3 The measuring system

The whole set-up is shown in Figure 2-9(b). A CCD camera is mounted onto the microscope to capture the image. The specimen with the hole is mounted on the stage. In order to reduce optical aberration of the system and simplify the system, both the eyepiece and the lens of the CCD camera are removed. The real image of the hole is project on to the CCD sensor area directly. Both the objective and the camera are fixed on the limb of the microscope. The total magnification of the system is then calibrated. Different height positions of the internal hole are investigated by moving the hole with the stage up and down.

The magnification of the system was calibrated by taking an image of a microscope calibrator. The image is shown in Figure 2-13. The scale increment is 10 μm.

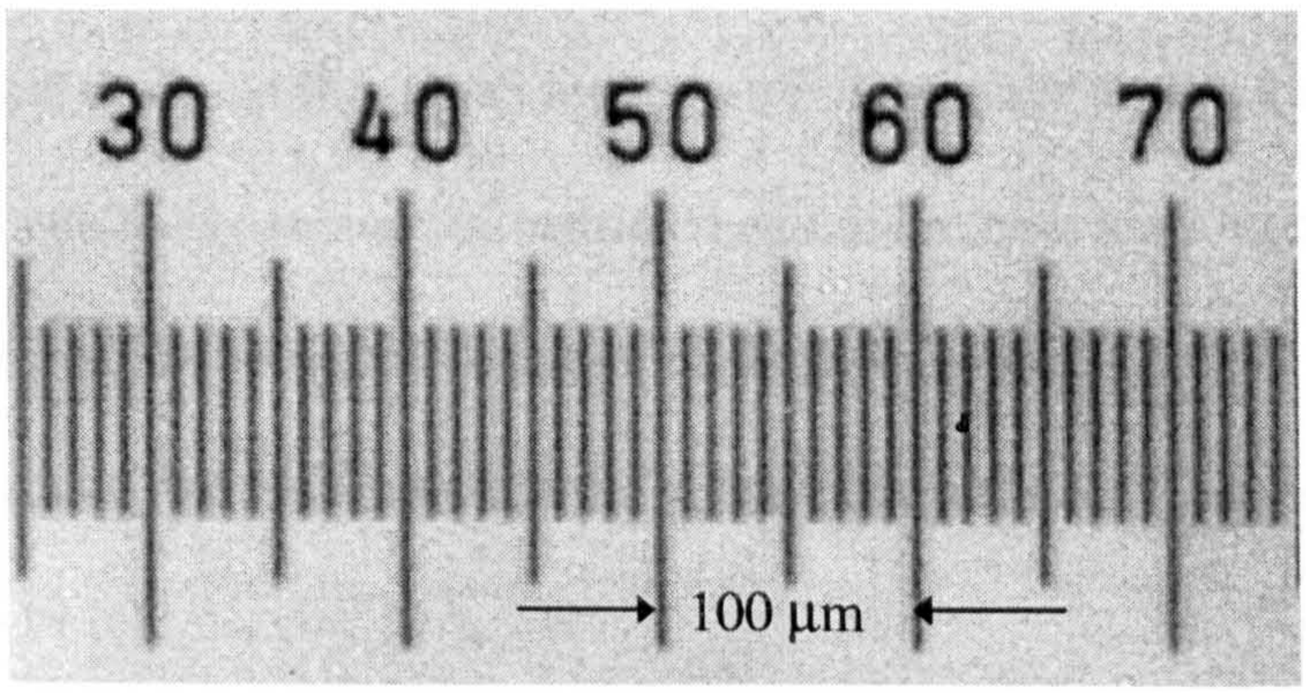

Figure 2-13 An image of the calibrator

2.4.4 Adjustment of stage

The functions of the stage are:

1) to hold the hole in a proper position (The position is discussed later).

2) to move the hole up and down to get the images of different height of the hole.

It needs only a one degree of freedom control to move the hole during the measurement. However, it needs a five degree of freedom stage to adjust the hole into a proper position. The proper position means that the axis of the hole is parallel to the axis of the optical system and the image of the hole is in the centre of the screen. This position can guarantee that:

1) The light can illuminate internal surface homogeneously.

2) The image of the hole can be kept in the centre of the screen during the measurement.

Referring to Figure 2-14, the procedure of the position adjustment is:

1) Move the open/restricted end of the hole inside the focal plane and move the hole inside the field of view;

2) Move the hole down/up though all the measurement range to check the position of the hole. If both the open and the restricted end of the hole are roughly in the centre of the field of view, the direction of the hole is correct;

3) Otherwise, rotate and move the hole to adjust the position of the hole as shown in as Figure 2-14 (c);

4) Repeat the procedure until the hole is in the required position.

The position adjustment is achieved manually. The vertical movement during the measurement is controlled automatically.

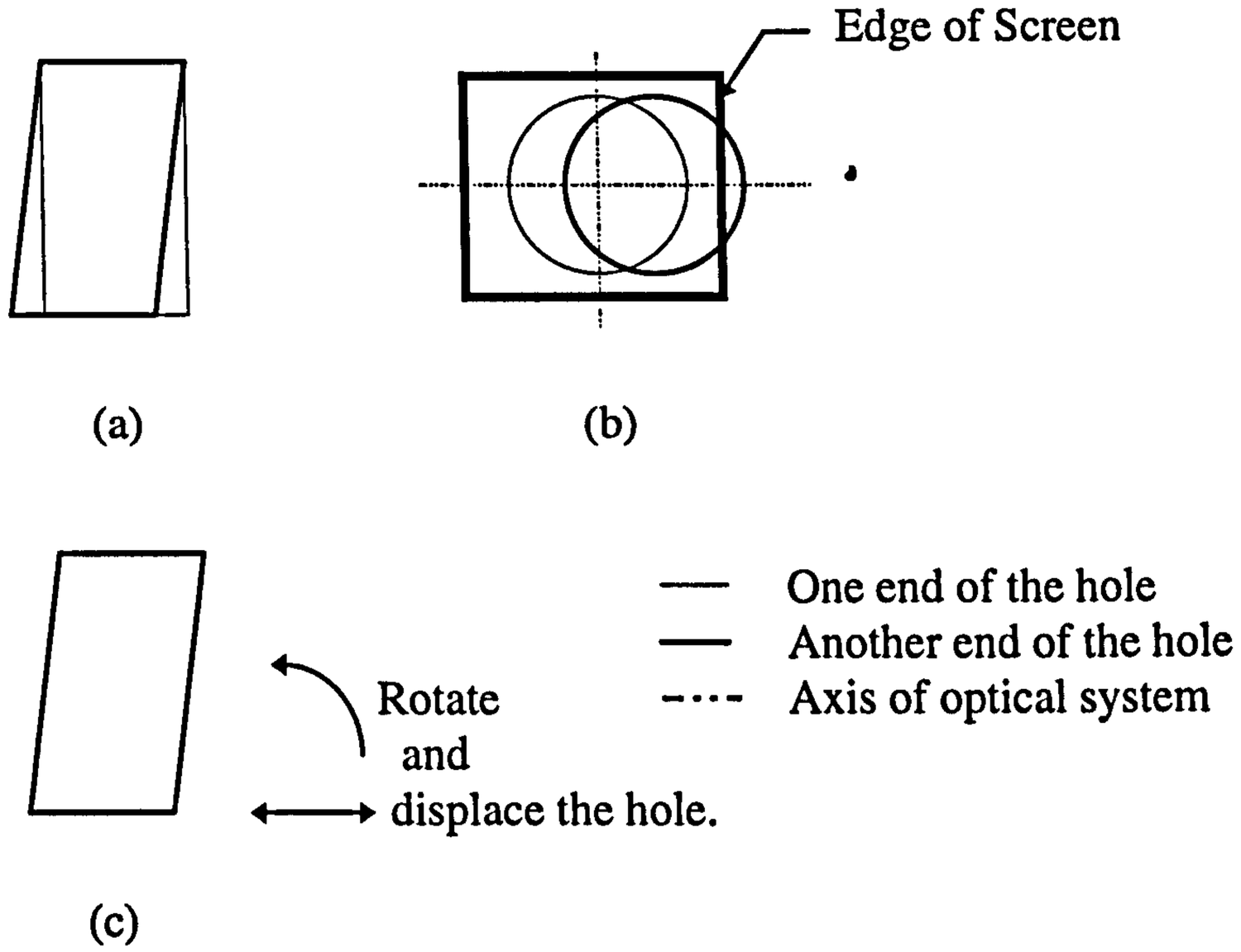

Figure 2-14 The procedure of hole position adjustment.

2.4.5 The resolution

Three parts of the system will influence the final resolution: the CCD camera, the A/D board and the objective. The resolutions of the CCD and the A/D board are matched. They divide the detection area (a 6.4 × 4.8 mm rectangle)into 512× 512 pixels. So the resolution is approximately 12.5 μm in the image plane. The diffraction limited resolution of the objective is, when considered in the image plane: $0.5\times\lambda\times M/N.A.$ where λ is the wavelength, say 550 nm; M is the magnification of the objective and N.A. is the numerical aperture of the objective. The calculated values are given in Table 2-1. Because the resolutions of the objectives in image plane are larger than the resolution of the camera and the A/D board, the resolution of the system is determined by the objective used.

Table 2-1 N.A. , Magnification and Resolution of objectives

N.A. of objective	Magnification	Resolution in image plane (μm)	Resolution on the sample (μm)
0.1	5	13.8	2.8
0.2	10	13.8	1.38
0.3	20	18.3	0.92

2.4.6 The software required

A software in C has been developed to control the stage movement accurately and set the A/D converter correctly. The stage should be controlled to move up and down in order to measure different positions of the hole. Gain and Off-set of the A/D converter should be set correctly to maximise the signal to noise level.

Software developed with MATLAB is used for image processing. Three requirements of this program are:

1) recognising the centre of the in-focus-strip in each image (main part);

2) working out the cross sections of different positions of the hole;

3) calculating the centre of the area and reconstructing a three dimensional shape of the hole.

The programmes will be discussed in the next chapter.

2.5 Verification of the technique

The technique of internal dimension measurement has been examined by measuring the thickness of a feeler gauge. The gauge is put vertically inside the system where the hole is mounted as shown in Figure 2-15 (a). Both sides of the feeler are illuminated. Two in-focus-strips can therefore be seen from the CCD camera, as

shown in Figure 2-15 (b). If the distance of these two strips can be proved as the same as the thickness of the feeler, the method of internal dimensional measurement is verified.

The magnification of the system has been calibrated (the image is shown in Figure 2-13). The thickness of the feeler can therefore be measured by counting the number of pixels between these two strips. The thickness of the feeler measured by the optical system is 0.254 mm (0.1 inch). It is the same as the maker specified. It is also double checked by a micrometer.

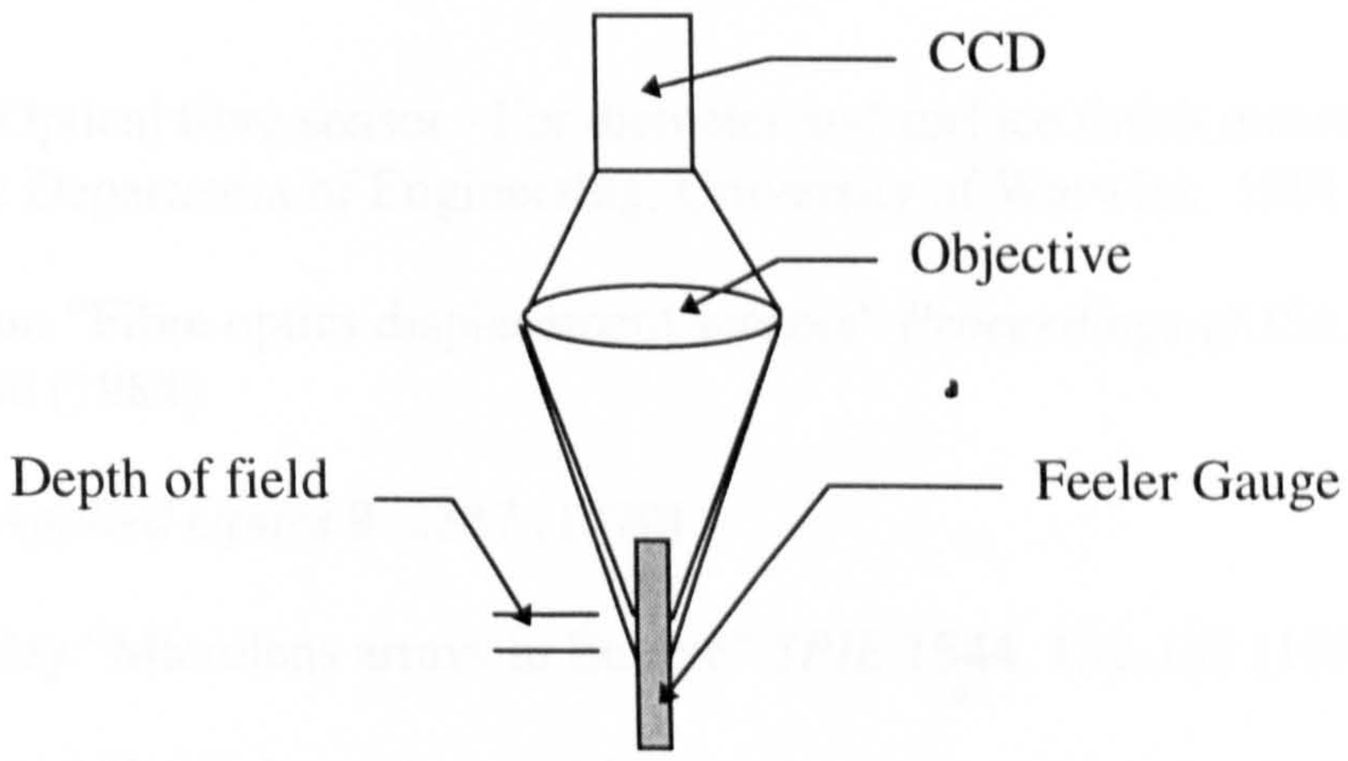

(a)

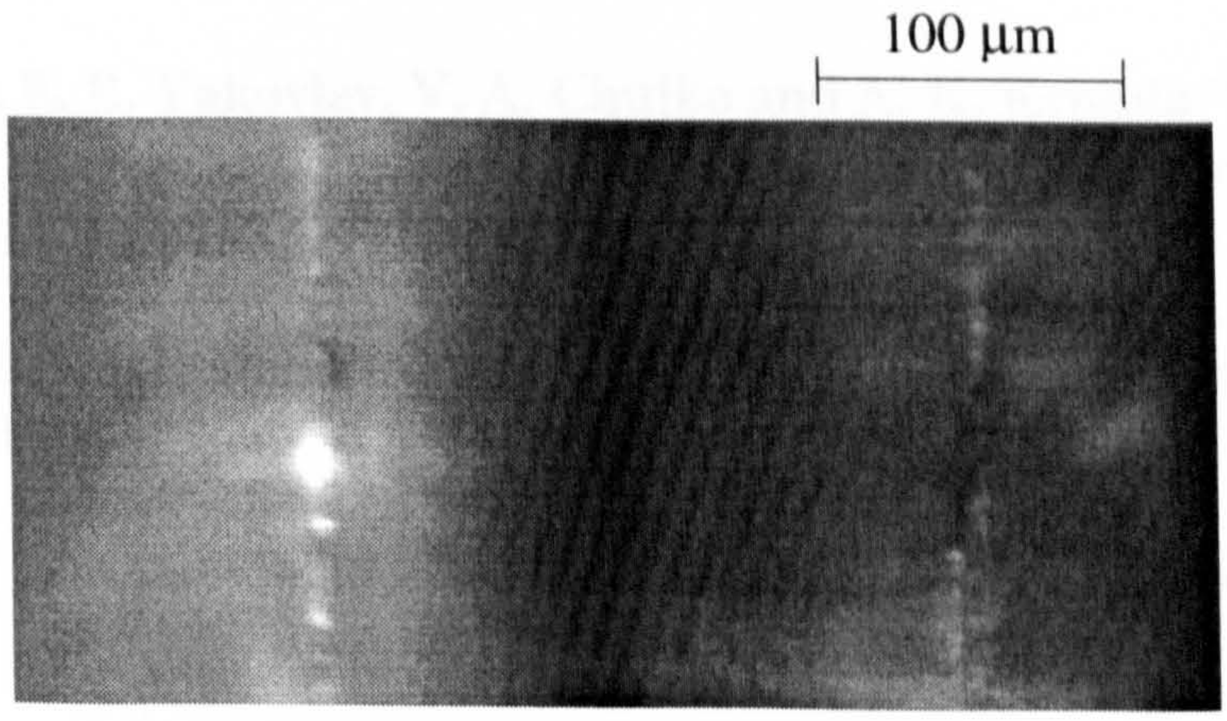

(b)

Figure 2-15 (a) The method to verify the technique

(b) Two in-focus-strips of feeler gauge

2.6 Conclusion

So far the final decision has been made for the small hole dimensional measurement. That is by the means of conventional optical sectioning microscopy, the cross section of certain height position of can be represented as an annulus-like in-focus-strip on the image. The location of the in-focus-strip can be defined by digital image processing techniques which are discussed in the following chapter.

Reference

[1] **K. P. Yu** "Optical fibre sensor - For diameter and surface finish measurement" *Thesis for MSc* Department of Engineering, University of Warwick 1991

[2] **D. A. Khron** "Fibre optics displacement sensors" *Proceedings of ISA*. Houston, TX **39** 331-340 (1984)

[3] **J. Simon** *Applied Optics* **9** 2337 (1970)

[4] **M. C. Hutley** "Microlens arrays in Europe" *SPIE* **1544** 134-137 (1991)

[5]**J. Bartley and W. Goltsos** "Laser ablation of refractive micro-optic lenslet arrays" *SPIE* **1544** 140-145 (1991)

[6] **V. P. Veiko, E. B. Yakovlev, V. A. Chujko and A. K. Kromin** "Laser heating and evaporation of glass and glass-borning materials and its application for creating MOC" *SPIE* **1544** 152-163 (1991)

[7] *Manu of 4710 Series Monochrome CCD Cameras* COHU Electronics Division San Diego CA, USA

[8] **K. Brenner** "Techniques for integrating 3-D-optical systems" *SPIE* **1544** 263-270 (1991)

[9] **D. Birchon** *Optical Microscope Technique* George Newnes Limited, London 1961

[10] **T. G. Rochow and E. G. Rochow** *An Introduction to Microscopy by Means of Light, Electrons, X-Rays, or Ultrasound* Plenum Press London 1978

[11] **D. A. Agard** "Optical sectioning microscopy: Cellular architecture in three dimensions" *Annual Review of Biophysics and Bioengineering* **13** 191-219 (1984)

[12] N. J. Severs, R. G. Gourdie, E. Harfst, N. S. Peters and C. R. Green "Intercellular-Junctions and the application of microscopic techniques - The cardiac gap junction as a case model" *J. Microscopy-Oxford* **169**(Pt3) 299-328 (1993)

[13] M. Laurent, G. Johannin, H. Leguyader and A. Fleury "Confocal scanning optical microscopy and 3-dimensional imaging" *Biology of the Cell* **76**(2) 113-124 (1992)

[14] J. M. Murray "Neuropathology in Depth - The role of confocal microscopy" *J. Neuropathology and Experimental Neurology* **51**(5) 475 -487 (1992)

3. Development of Software

As mentioned in section 2.4.6 (p.54), two aspects of the software are required for small hole measurement. One of them developed in C programme is used to control the stage movement accurately and to set the A/D converter correctly. The other part developed with MATLAB is used for image processing. The second part has been converted into C language to increase its speed of operation.

3.1 Stage control and A/D converter setting

3.1.1 Stage control

The stage is driven by a stepper motor only in the vertical direction. The stepper motor is supplied by RS Components Ltd. [1] . The step angle is 1.8^0. The step angle tolerance is $\pm$ 5.4 minutes. The motor is driven by a unipolar drive board provided by RS components Ltd as well. The clock and direction signal is sent from a parallel 8 bit input/output (I/O) board on the computer. And the I/O board is controlled by the software. This kind of stepper motor was chosen because it has been used in the laboratory for a long time. It seems always available and can satisfy the need of the stage control.

3.1.2 A/D board setting

In order to get maximum contrast and signal to noise ratio of the image, two settings must be checked and adjusted: Gain and Off-set [2]. In the Figure 3-1, the off-sets are set to be the same for (a) and (b), so as to (c) and (d); the gain are set to be the same for (a) and (c), so as to (b) and (d). Because there are only 8 bits of grey level in the digital image, the signal may be truncated as shown in (d), even the gain is set to be the same as that in (b). The board must therefore be set properly. The best procedure of the setting is:

1) to set the off-set until the darkest area in the image is reduced to the lowest grey level required.
2) then to set the gain of the board until the signal is maximised just before its cut off point.
3) If necessary the above two procedures can be repeated.

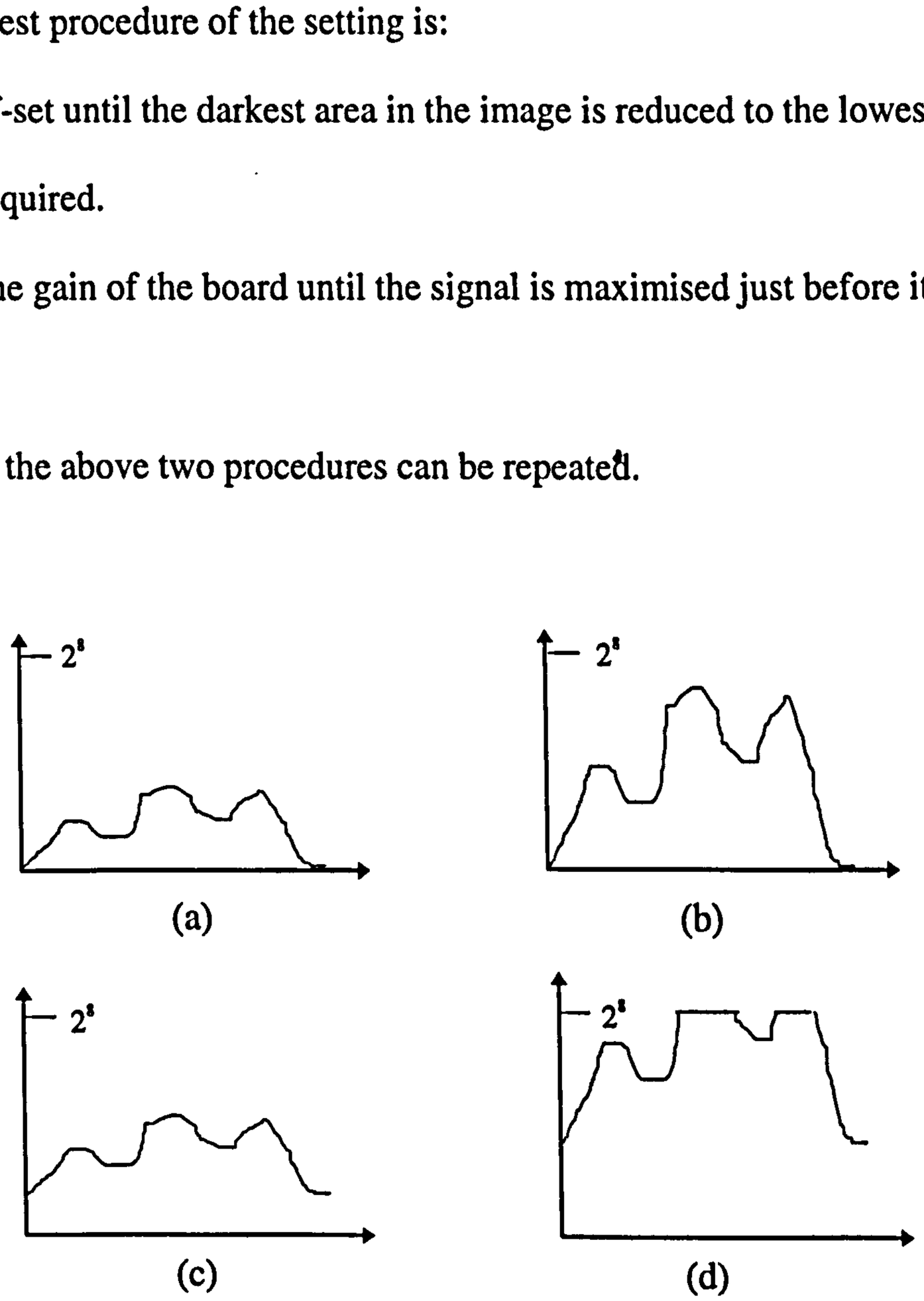

Figure 3-1 An example of gain and off-set settings

This procedure has been completed as an automatic operation. In the programme, the grey level at four corners are checked first, whose grey levels are always the lowest in the image. They are then set to the required level by changing the off-set of the board. The next step is to check the grey level in the centre of the image, where the brightest area in the image located. They are then adjusted to the maximum by setting the gain of the board.

To choose the lowest grey level, two factors should be considered.

1) The effective grey level range.

   The total grey level range is fixed (8 bits), the higher the lowest grey level, the smaller the effective grey level range.

2) The signal to noise level in the area.

   Because of the absolute error created by quantization does not change with the A/D board settings, the relative error is reduced if the grey level is increased (as it will be discussed in section 3.2.1.2).

The lowest grey level is chosen as 40. Thus, the dynamic grey level range is 255 - 40 = 215 and the signal to noise ratio (created by quantization) is higher than 40/1.

3.2 Digital image processing

The second aspect of the software can be further sub-divided into three parts:

1) locating the centre curve along the in-focus-strip.

2) calculating the area and the centre of every cross section.

3) working out the shape of the hole from a series of cross sections.

The first part is the most important and most time consuming. It involves digital signal processing. A review of digital signal processing and edge detection technique is given in this section. The details of the programme are then discussed.

3.2.1 Theoretical and mathematical basis for image processing methods applied[3][4].

Digital signal and image processing perform on a group of numbers representing the original signal and produce another group of numbers representing the processed signal. Afterward, the information of interest are emphasised. Image enhancement, restoration and segmentation are examples. The first treatment operation on the original image is referred as to digitise the analogue image both spatially and in grey level. This process is referred as Sampling and Quantization [4].

3.2.1.1 Sampling

The process to digitise image spatially is called sampling, it takes values $I(nT_x, nT_y)$ from $I(x,y)$ to represent the analogue image $I(x,y)$. Where T_x and T_y are the sampling period along x and y direction respectively. Figure 3-2 is the explanation of one dimensional sampling, where (a) is the signal before sampling and the solid lines in (b) are values of the signal after sampling. Because this process picks up finite data from the analogue signal, the signal

can only be fully recovered if its maximum frequency $\leq 1/2T$ (due to the Sampling Theorem or Whittaker-Shannon's Theorem [6]).

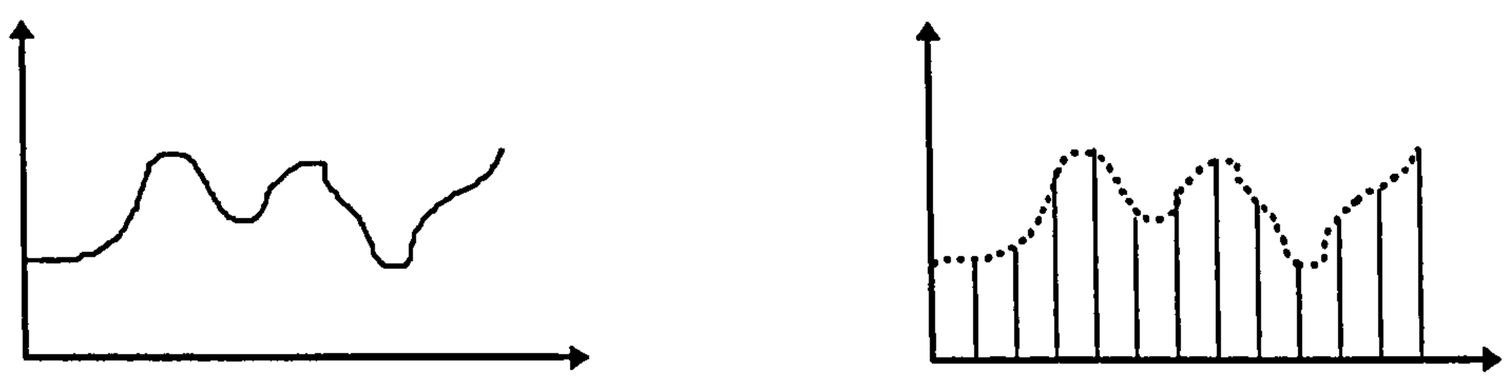

(a) (b)

Figure 3-2 One dimensional sampling

3.2.1.2 Quantization

Another digital process is called quantization, which represents the graduation of signal intensity by a set of finite steps. All signals that fall inside the same interval will have same value after this process, as shown in Figure 3-3. Figure 3-3(a) is the signal before quantization, whilst the solid lines in Figure 3-3 (b) are the values of the signal after the process. It is clear that during this process, some errors will appear. The accuracy increases with the number of steps. For certain steps, the relative error varies with the value of the signal. The lower the original signal, the larger the relative error. This is why the lowest grey level of the A/D board is not set to zero. In one dimensional analogue-digital conversion, the number of steps could be 2^{16} (an A/D converter with 16 bits resolution) or more. However, for a two dimensional image an increase in the number of steps means a sharp increase in memory and processing time. The size of the digitised image used is 262 K byte.

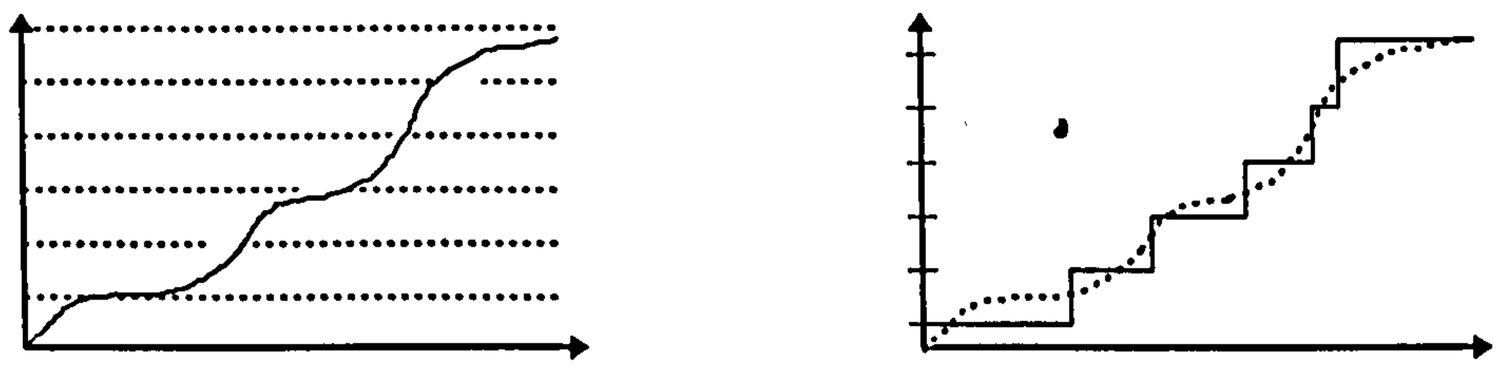

(a) (b)

Figure 3-3 An example of quantization

3.2.1.3 Digital filter and design

Digital filters of time-invariant discrete linear systems are very important tools in digital signal processing. The filter is described by fixed characteristics. The technique was developed to deal with one-dimensional signals at first, where time was the variable. The term time-invariant is used for convenience. In image processing, the variable is the spatial interval. The definition of the linear time-invariant system is [3]: If the system converts x(n), a set of input data, into a set of output data y(n), it therefore converts:

1) $x_1(n) + ax_2(n)$ into $y_1(n)+ay_2(n)$. (Linear)

2) $x(n-n_0)$ into $y(n-n_0)$. (Time-invariant)

Where a is any constant, n_0 is an integer which lets $x(n-n_0)$ exist.

The filters can be divided into two groups according to their structure. One is the Finite Impulse Response (FIR) filters which produce an output number by weighted summation of a finite set of input numbers. There are only a finite number of non-zero value coefficients in the weighted summation. The other

is called Infinite Impulse Response (IIF) filters which are governed by a convolution equation based on an infinite number of terms, so it needs an infinite memory theoretically. In practice, the memory is achieved by feeding the output back to the input. The filters can be expressed in the following recursive way:

$$\text{FIR:}\quad y(n)=\sum_{k=0}^{N-1}h(k)x(n-k) \tag{3.1}$$

$$\text{IIR:}\quad y(n)=\sum_{k=0}^{\infty}h(k)x(n-k)=\sum_{k=0}^{N}a_k x(n-k)-\sum_{k=0}^{M}b_k y(n-k) \tag{3.2}$$

Where $x(n)$ is the input; $y(n)$ is the output; $h(n)$ is the impulse response of the system; a_n and b_n are coefficients of the filters. The main difference between the two kinds of filters are listed in Table 3-1.

Table 3-1 Comparison of two kinds of filters: FIR IIR

	FIR	IIR
Phase	Linear	Non-linear
Stability	Always	No guarantee
Noise of quantization	Low	High
The order in same function	High	Low
Analogue equivalent	No	Yes
Difficult to synthesise	high	low

The filters are also grouped by their function of frequency. There are four groups: low pass, high pass, band pass or band stop. The last two are the combination of the first two. Their behaviours in the frequency region are shown in Figure 3-4, where region 1 2 and 3 represent passband, transition band and stopband respectively. f_p is the passband edge frequency. f_s is the

stopband edge frequency. Two other key parameters for the filters are passband and stopband deviation, which describe the uneven transformation of the filters in passband and stopband. The MATLAB package presents a convenient method for visualising the effect of the filters in both amplitude and phase. To design a filter a few specifications are needed: type of filter, passband edge frequency, stopband edge frequency and the order of the filter.

(a)

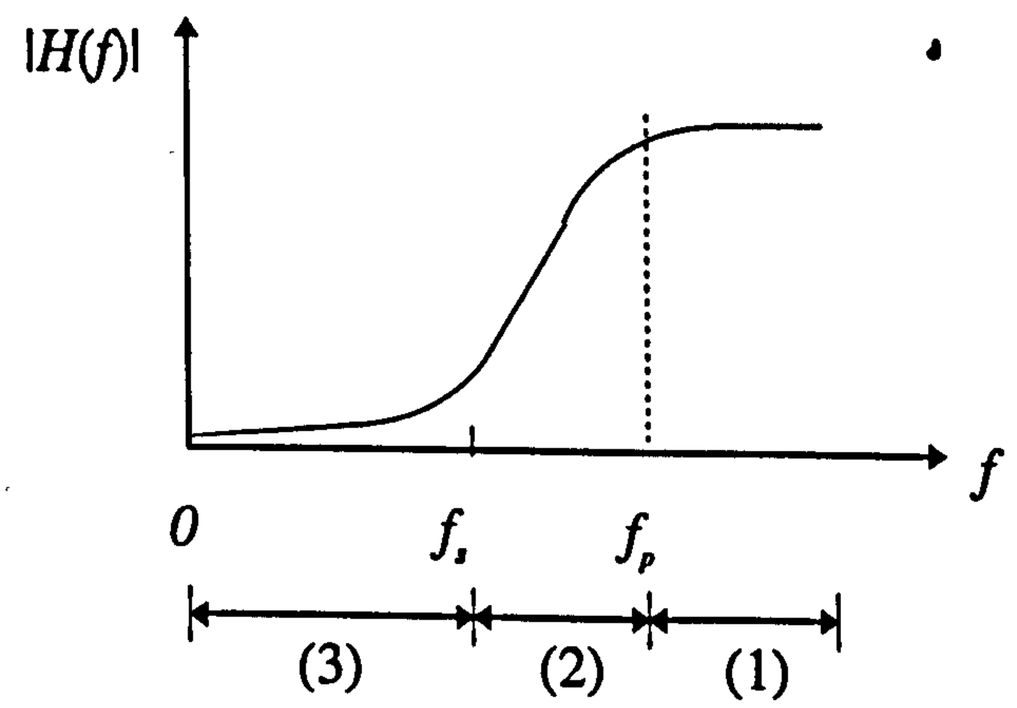

(b)

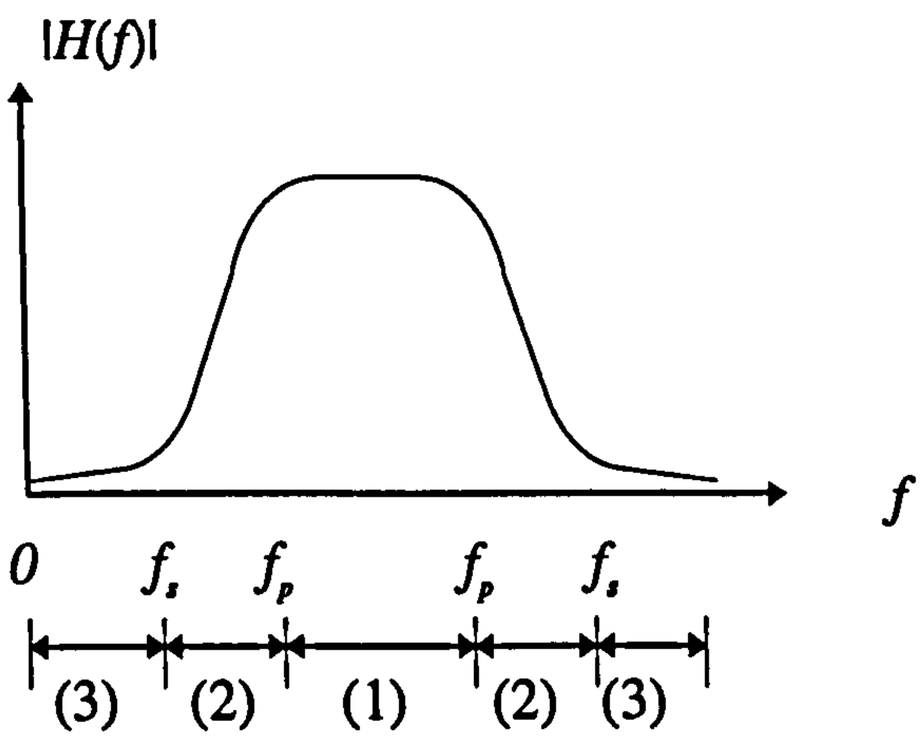

(c)

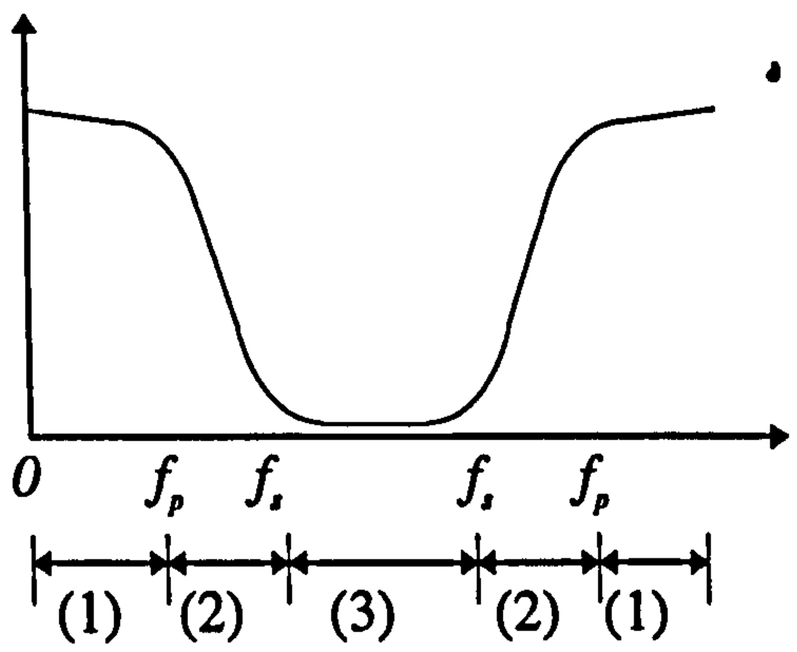

(d)

(1) Pass band; (2) transition band; (3) stopband

Figure 3-4 Illustration of filters (a) low pass; (b) high pass; (c) band pass and (d) band stop.

3.2.2 A review of edge detection

Edge detection is a main part of image segmentation, it subdivides an image into its constituent parts depending on the change of the grey level in the image [4]. Many techniques have been developed in edge detection for special purposes or for more general cases. In general the edge is where the grey level

changes most rapidly. In practice there are some models of the edge as shown in Figure 3-5 [7] [8]. Those models have their physical meanings: the ideal step edge (a) usually corresponds to the clean border of the object, The blurred (c) and ramp + step (b) edge comes from changes in the illumination of the scene. Whilst the pulse step (e), roof (f), delta (g) and staircase step (d) edges result from mutual illumination between objects and background.

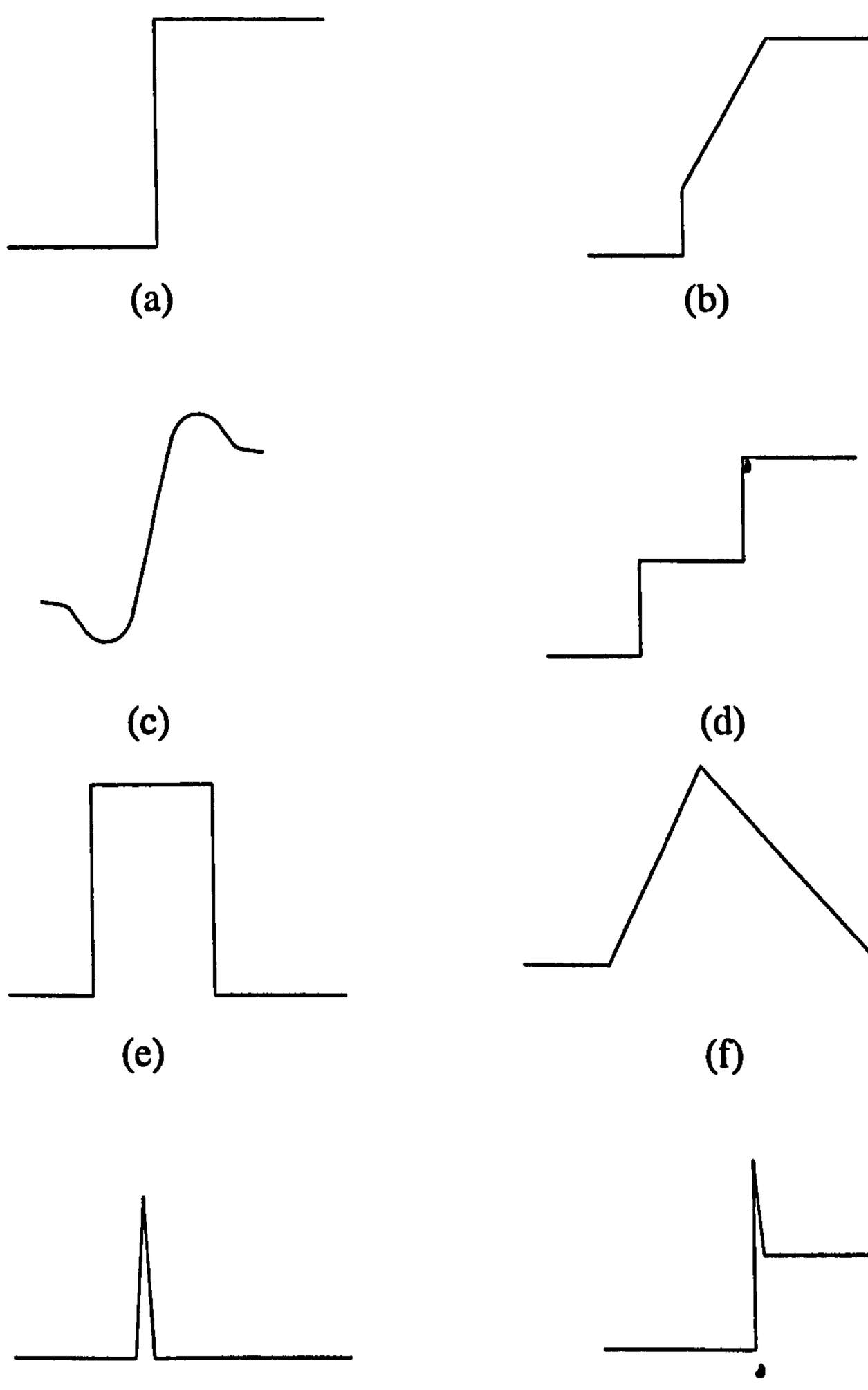

Figure 3-5 Edge models: (a) step, (b) step + ramp, (c) blurred, (d) stair case step, (e) pulse step (f) roof, (g) delta and (h) step+delta

Because the edge is where the intensity of the image changes rapidly. It is obvious to use the differential of the grey level to detect the edge. For example Gradient operators: $\nabla I=\partial I/\partial x+\partial I/\partial y$, where $I(x,y)$ is the image. In the digital image processing two kind of masks are used as each of the partial differential operator:

$$\partial I/\partial x = \begin{array}{|c|c|c|}\hline -1 & -2 & -1 \\ \hline 0 & 0 & 0 \\ \hline 1 & 2 & 1 \\ \hline \end{array} \qquad \partial I/\partial y = \begin{array}{|c|c|c|}\hline -1 & 0 & 1 \\ \hline -2 & 0 & 2 \\ \hline -1 & 0 & 1 \\ \hline \end{array} \qquad 3.3$$

The Laplacian operator is another example of finding the edge in an image from its intensity changes. The Laplacian of the image I(x,y) is $\nabla^2 I=\partial^2 I/\partial x^2+\partial^2 I/\partial y^2$. It can also be written discretely and in an approximate form by a 3×3 mask:

$$\nabla^2 I = \begin{array}{|c|c|c|}\hline 0 & -1 & 0 \\ \hline -1 & 4 & -1 \\ \hline 0 & -1 & 0 \\ \hline \end{array} \qquad 3.4$$

As the differential is sensitive to noise, the image requires a pre-filter before applying edge detection. On the other hand, pre-filter will blur weak edges (where the intensity does not change very sharp). The balance between removing noise, preserving the weak edges and the computation speed is always a compromise. A weighted sum of six edge quality(continuity, smoothness, thinness, localisation detection and noisiness) was proposed to be a metric of edge quality[34]. The quality of edge detection has also been discussed. The detectors are examined in the following five aspects: good detection, good localisation, robustness, efficiency and application to sparse data [35].

In general, the original image is smoothed first by using a low pass filter. A Laplacian-of-Gaussian operator (LoG) is proposed [9]. It smoothes the image $I(x,y)$ by convoluting it with a Gaussian function: $G(x,y,\sigma) = \exp(-x^2/2\pi\sigma^2)/\sigma\sqrt{2\pi}$. The edge is the solution of $\nabla^2(I(x,y)*G(x,y,\sigma)) = 0$. It is called zero crossings (ZC). σ is the scale of the filter. The larger the scale, the more the image is smoothed and blurred. Later works [10]-[18] attempt to increase the accuracy of localisation.

Because removing noise is always in conflict with retaining weak edges, using of a simple low pass filter or static threshold are not enough. Some other efforts are made. For example, an automatic thresholding method was studied[20]. The threshold is determined based on human visual perception. Another example is that the filter is optimised according to the local image structure to remove noise from output of LoG operator[21], a multi-scale approach has been studied by many researchers [7], [9], [22]-[26]. Those scales are selected to detect edges in different parts of the image. In edge-focusing techniques the scale is changed from coarse to fine [24]. A reversal method has also been tried[25]. It changes the scale from fine to coarse. A two-scale method is also considered [7], where the choice of scale is determined by the edge itself.

The image smoothing process has been further studied in scale-space, where the scale is not just a few values but a variable[27] [28] [29]. The application of image smoothing has been equivalent to the solution of the heat conduction

or diffusion. The temperature in an area is equivalent to the intensity in the image. The time in heat conduction is equivalent to the smoothing scale in image processing. Therefore the application of smoothing can be written as :

$$\partial I/\partial t = C\nabla^2 I \quad \text{with} \quad I(x,y,0) = I_0(x,y), \qquad 3.5$$

where C is diffusion conductance. It is interesting that the light intensity can be considered in this area as temperature distribution. The process of smoothing is the same as a heat conduction. It is obvious that this conduction will blur the edge with a constant C. To avoid edge blurring, a non-homogeneous diffusion conductance $C(x,y,t)$ has been introduced[30]. The diffusion equation of heat conduction is in the form of:

$$\partial I/\partial t = \nabla(C(x,y,t)\,\nabla I(x,y,t)), \quad \text{with} \quad I(x,y,0) = I_0(x,y) \qquad 3.6$$

As a function of this non-homogeneous diffusion conductance $C(x,y,t)$, the process of smoothing will not blur the edge. Because this non-homogeneous diffusion conductance will stop the 'heat' exchange from a high 'temperature' area to a low 'temperature' area. With a proper choice, the non-homogeneous diffusion conductance can even work like a 'heat' pump. It pumps the 'heat' from the low 'temperature' area to the high 'temperature' area. The result is that the edge has been enhanced. Further studies on this approach have been made to improve the method [31]-[33].

To filter the image, it is important to notice that there are two kinds of noise inside the image. One is the noise caused by the system, such as electronic noise, quantizition noise. The removal of this kind of noise is always needed.

The other kind of noise is dependent on what kind of details are of interest. For example, if the size of the object is required, the texture of the surface can be considered as noise (Detail of this example is given in Chapter 6), so choosing a method to filter this kind of noise depends upon the problem itself.

3.2.3 Optical sectioning image

Before starting to write the software, a close look at the image is helpful. The image is digitised with 525×512 in size and 8 bits in grey level (so the size of the file is 265 K bytes). In order to reduce the relative noise levels caused by electronic equipment and image quantization, the minimum grey level is set to 40.

3.2.3.1 Location of information

There is an annulus-like strip inside the image which is the image of the in focus part of the internal surface of the hole. It is shown in Figure 2-12 and defined as in-focus-strip. The other part of the internal surface is blurred as they are out of focus.

The annulus-like strip is approximately centro-symmetrical. The central part of the image is brighter than the rest, due to the hole being illuminated from the bottom. The main part of the image is the out-of-focus image of the surface, no shadow pattern can be seen in the area. Compared with the side of

the image, a small fraction of the image has the information of the cross section.

3.2.3.2 In-focus-strip - A random edge

The in-focus-strip divides the image into two parts. The image of the internal surface above the sectioning plane is outside the annulus-like strip. The image of the internal surface below the sectioning plane is inside the annulus-like strip. In this way the strip can be considered as an edge, but it is not a conventional edge as described in Figure 3-5. Figure 3-6 plots light intensity distribution across the strip. The strip is located from 230 to 260 (pixel column) in the plot as marked by a dashed square. Figure 3-7 shows a 2-D intensity distribution of an area where the strip is crossed. It can be seen that the intensity is randomly distributed inside the strip. Therefore the edge has been defined as a random edge.

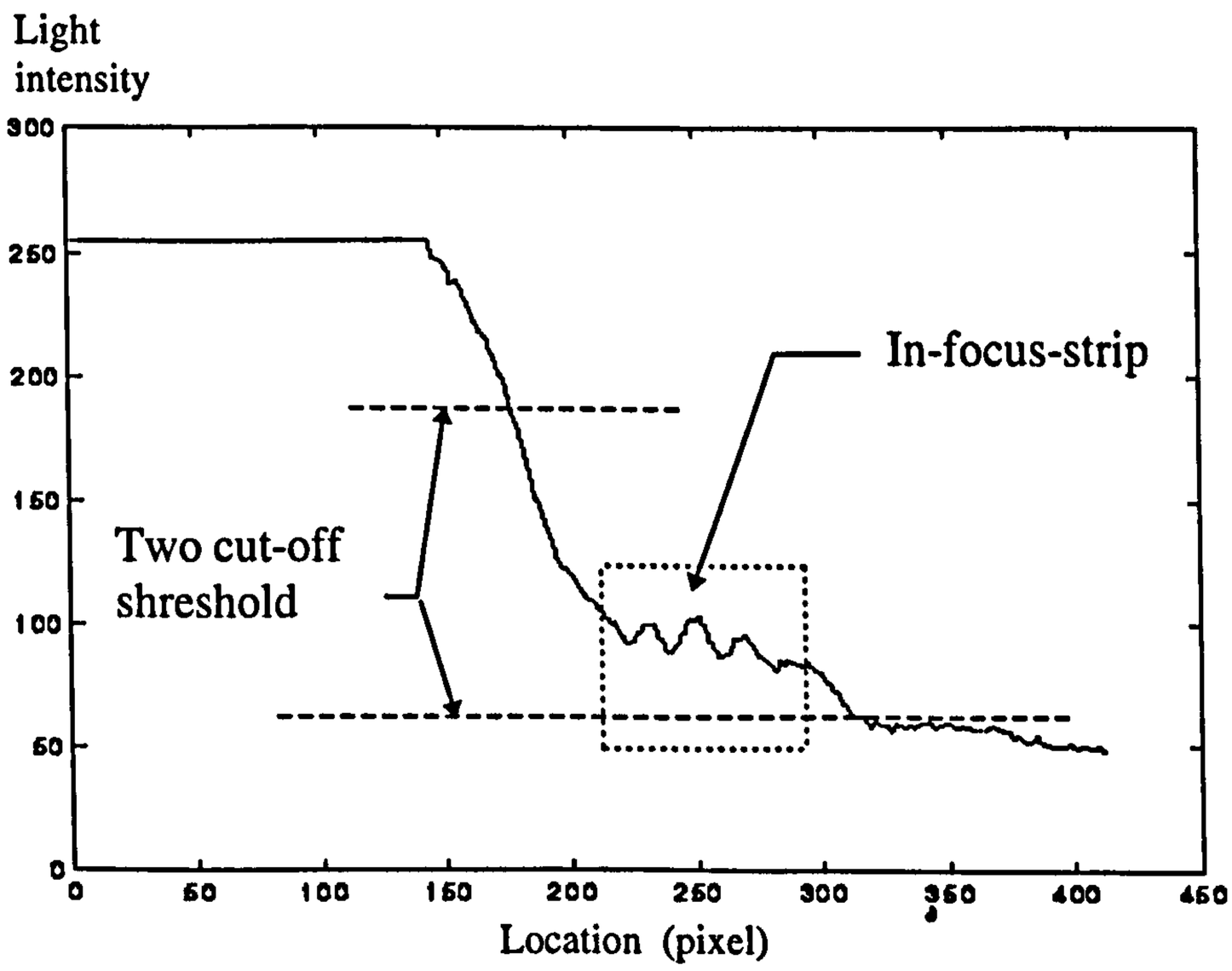

Figure 3-6 Light intensity distribution across the strip

A new approach is needed for random edge detection. The reasons are:

1. The intensity is randomly distributed inside the strip, there are many peaks inside the strip. The edge detectors, which are mentioned in section 3.2.2, find edges around every peak, the output fully fills inside the in-focus-strip instead a thin curve as shown in Figure 3-8. From this output the cross section cannot be find with high accuracy.
2. The random edge is only in a small fraction of the image, full size image processing is not efficient.

The new image processing, which is designed to locate the centre of the in-focus-strip in a small area, is described in the following sections.

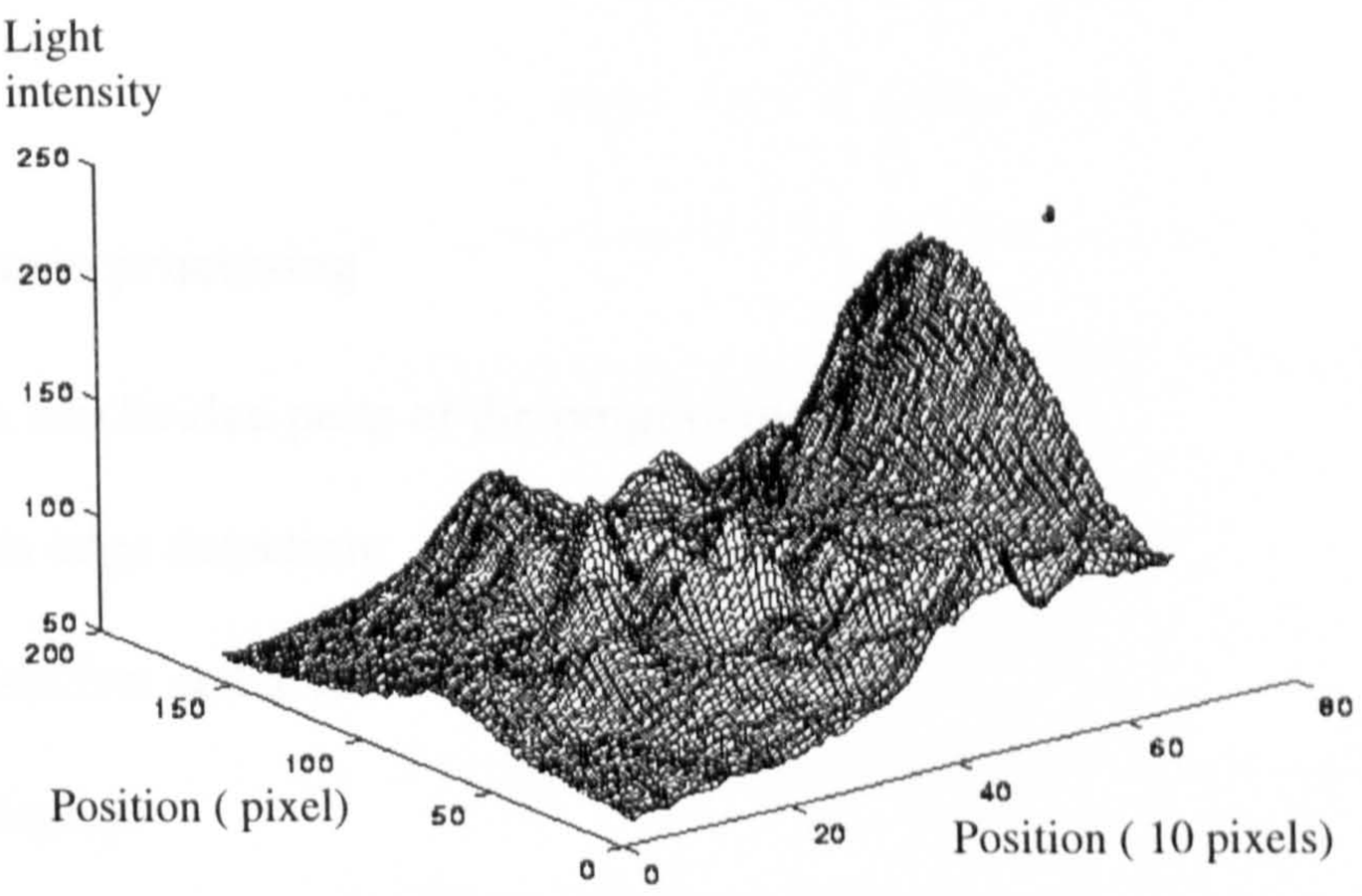

Figure 3-7 A 2-D plot of the strip

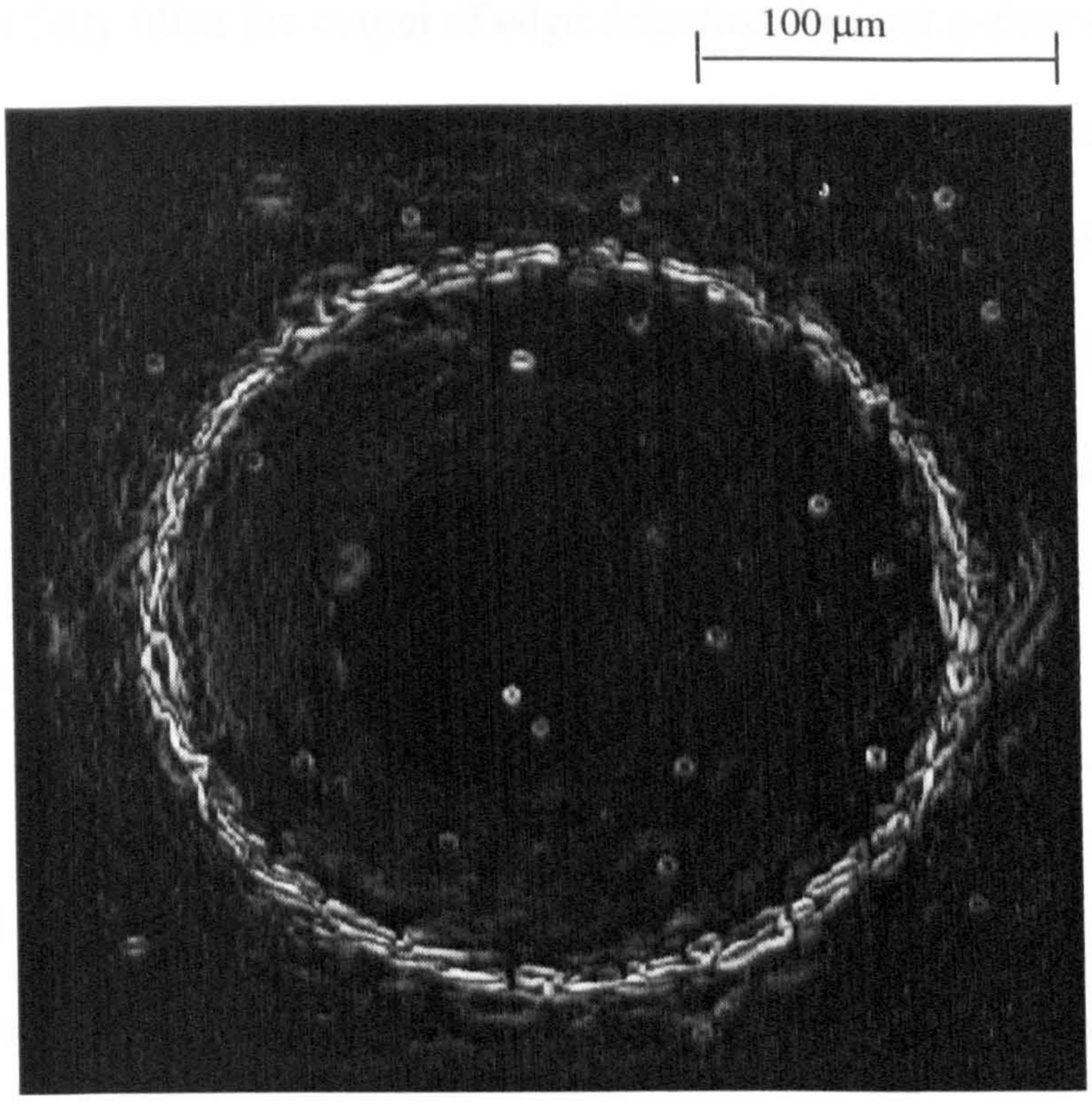

Figure 3-8 The output of an edge detector applied to a random edge

3.2.4 Image processing

The three subdivided parts of the programme are:

1) random edge detection;

2) cross section and area calculation;

3) 3-D display.

3.2.4.1 Random edge detection

It can be seen from Figure 3-6 that the intensity distribution has some peaks inside the in-focus-strip. This is because the strip is the shadow pattern of the internal surface. The edge detectors reviewed in section 3.2.2 are not suitable to locate the centre of the strip. The result of applying them to the in-focus-strip will be still a

strip, which is fully filled the output of edge detection, but not a clear curve. A random edge detection approach is more suitable. It can locate the centre of the in-focus-strip. The basic method of random edge detection is similar to the approaches reviewed in section 3.2.2: smoothing the data and using differential operators. The whole process of random edge detection is collecting data, removing illumination profile, applying differential and smoothing operation, locating the centre and finding the centre curve of the in-focus-strip.

1. Collecting data

The information of the cross section is in a small fraction of the whole images. Instead of dealing with the whole image, special data is used. The data is collected along a line which starts from the centre of the image, crosses the strip to the outside of the image as plotted in Figure 3-6. It can be seen that the random edge has its special feature(many peaks) in the data. The data can be optimised around the strip by setting two thresholds to cut the brightest and the darkest parts off.

2. Removing the illumination profile

The collected data contains two parts: the shadow pattern signal and the illumination profile. The differential of the data is not only a function of shadow pattern signal but also the illumination profile(the higher the profile, the larger the differential). In random edge detection, only the differential of the shadow pattern is interested. A low pass filter, whose stopband frequency is smaller than the frequency of shadow pattern signal, can be used to extract the illumination profile. A 5th-order Butterworth filter is used in the

programme for its simplicity. The shadow pattern signal can then be found from the following equation:

$$S_1 = (S_0 - \text{lowpass}(S_0)) / \text{lowpass}(S_0), \qquad 3.7$$

where S_0 is the original data, S_1 is the shadow pattern signal as shown in Figure 3-9. In S_1, both the absolute and relative values of illumination profile have been removed.

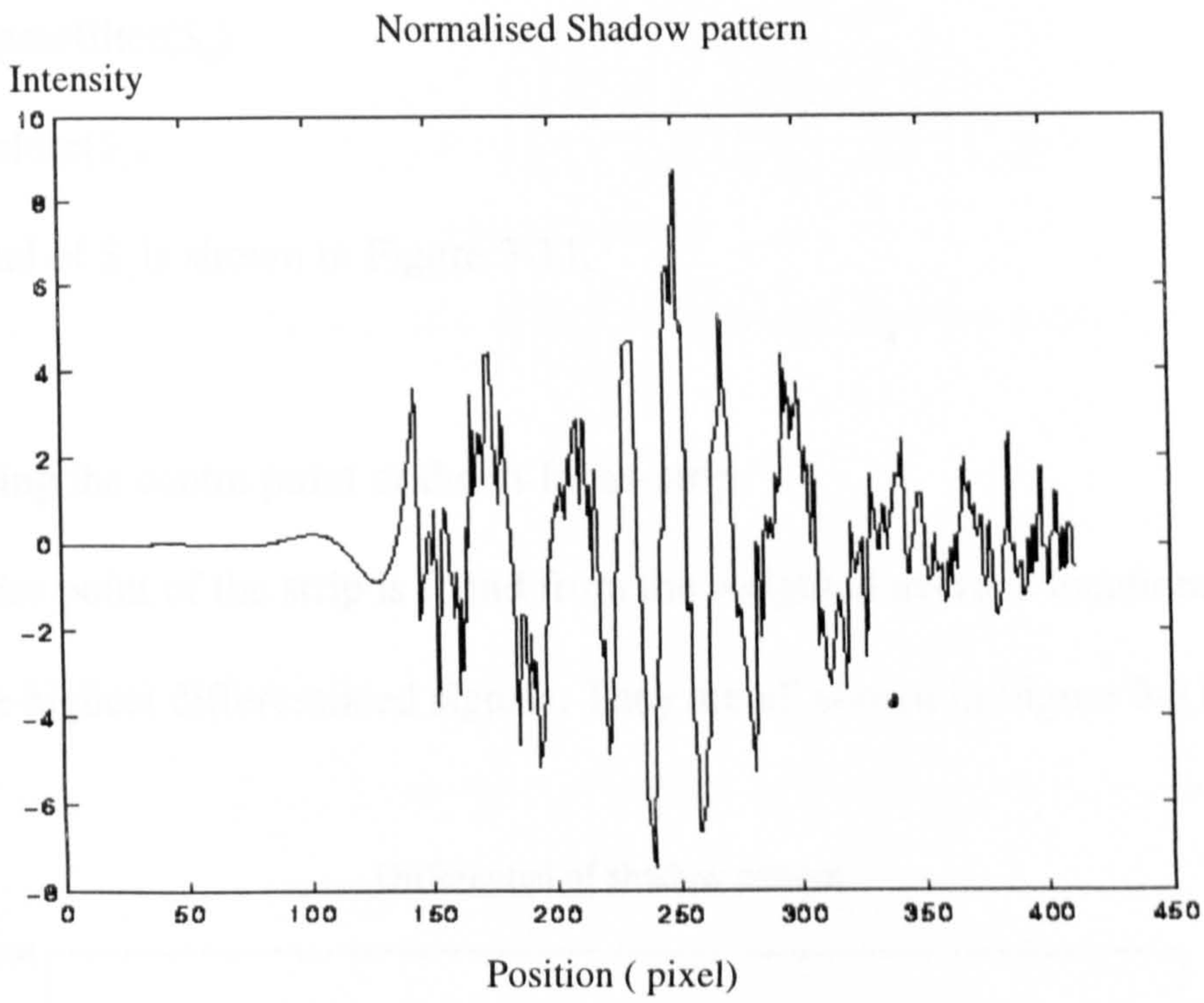

Figure 3-9 Normalised shadow pattern

3. Applying differential and smoothing operation

Differential and smoothing operations are always used in edge detection. In a linear and time-invariant system, it does not matter which one is used first. In the programme, the differential operation is applied to the S_1, the shadow pattern signal first. The result S_d is shown in Figure 3-10. The smoothing operation is then applied to S_d. The result is represented by S_s. The smoothing

operation is achieved by a 3rd-order Butterworth non-phase-shift filter. This non-phase-shift filter can smooth the signal without shifting the location of peaks. In order to compare the strength of the differentials, the absolute value S_a of S_s is calculated. The whole processing from original data to S_a can be written as :

S_m= (S_o- lowpass(S_o))/ lowpass(S_o)

S_d= differential of S_m

S_s = lowpassfilter(S_d)

S_a = absolute(S_s)

The signal of S_a is shown in Figure 3-11.

4. Locating the centre point of the in-focus-strip.

The centre point of the strip is found from the weighted average locations of the three highest differentiated signals. They are all shown in Figure 3-11.

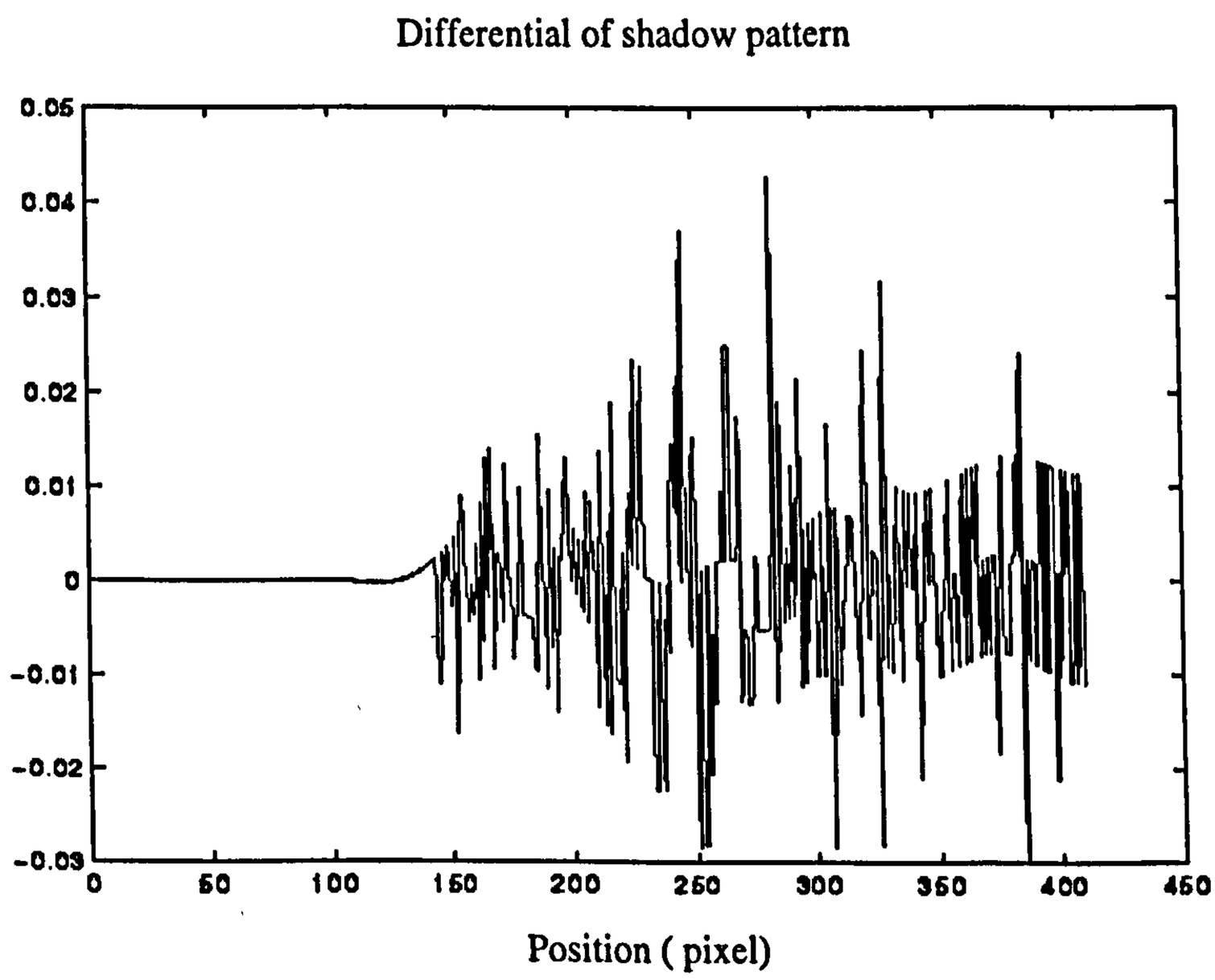

Figure 3-10 Differential signal of shadow pattern

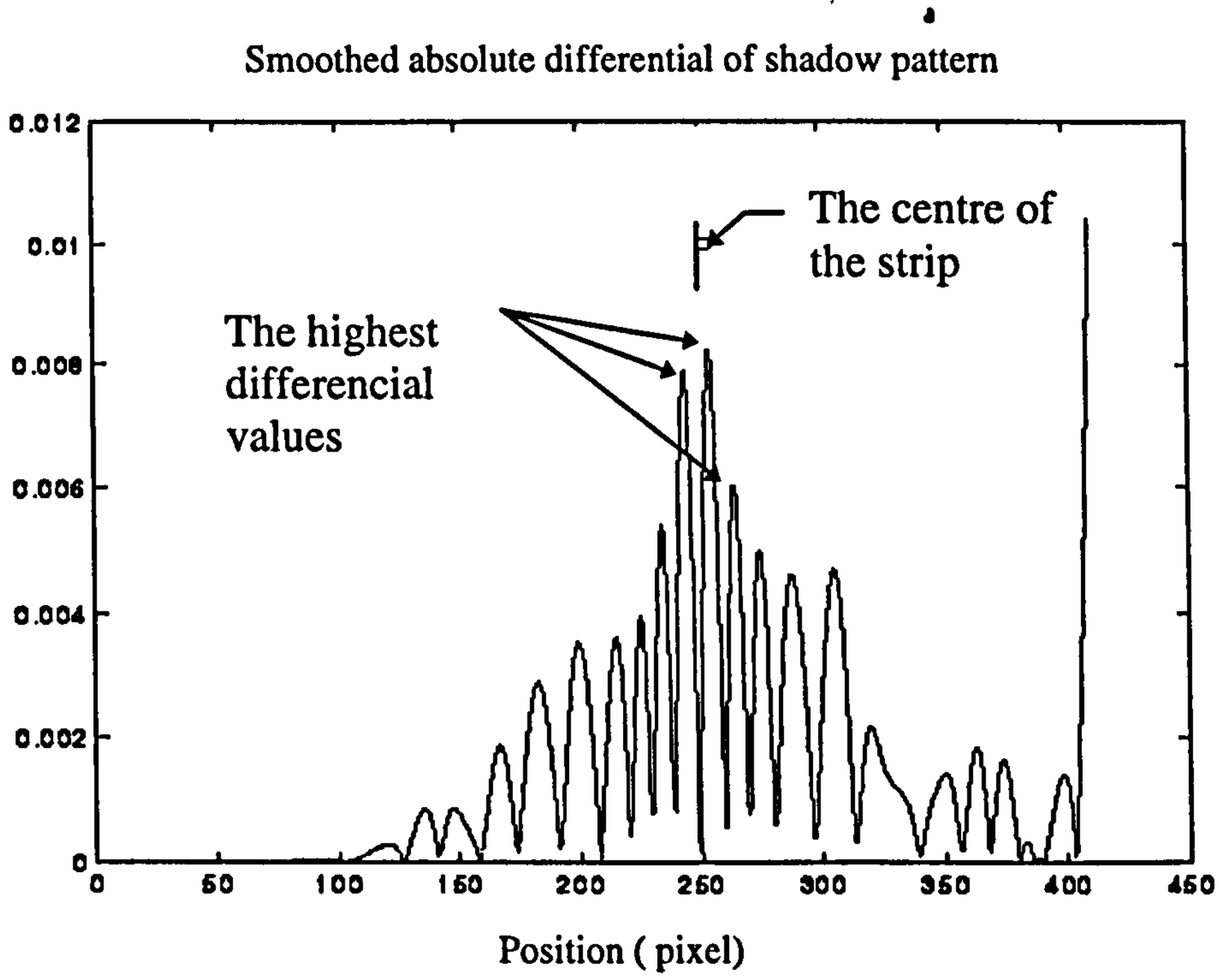

Figure 3-11 Smoothed absolute differential signal and the centre point of the strip

5. Finding the centre curve

The centre curve of the in-focus-strip is a series of centre points along the strip. The points can be found by the following method:

1) Define a series of lines which start from the centre of the image to the outside separated with a pre-set angle.

2) Repeat the above process on each line.

Now a crude centre curve is found. Part of the curve is shown Figure 3-12. This crude centre curve is then smoothed by another filter. A fine centre curve of the strip can be achieved as shown in Figure 3-13. Figure 3-14 represents a full view of the centre curve of the in-focus-strip. That is the cross section of

the hole at relative height. The accuracy of the measurement is the half width of the in-focus-strip. In this case, it is ± 3 μm.

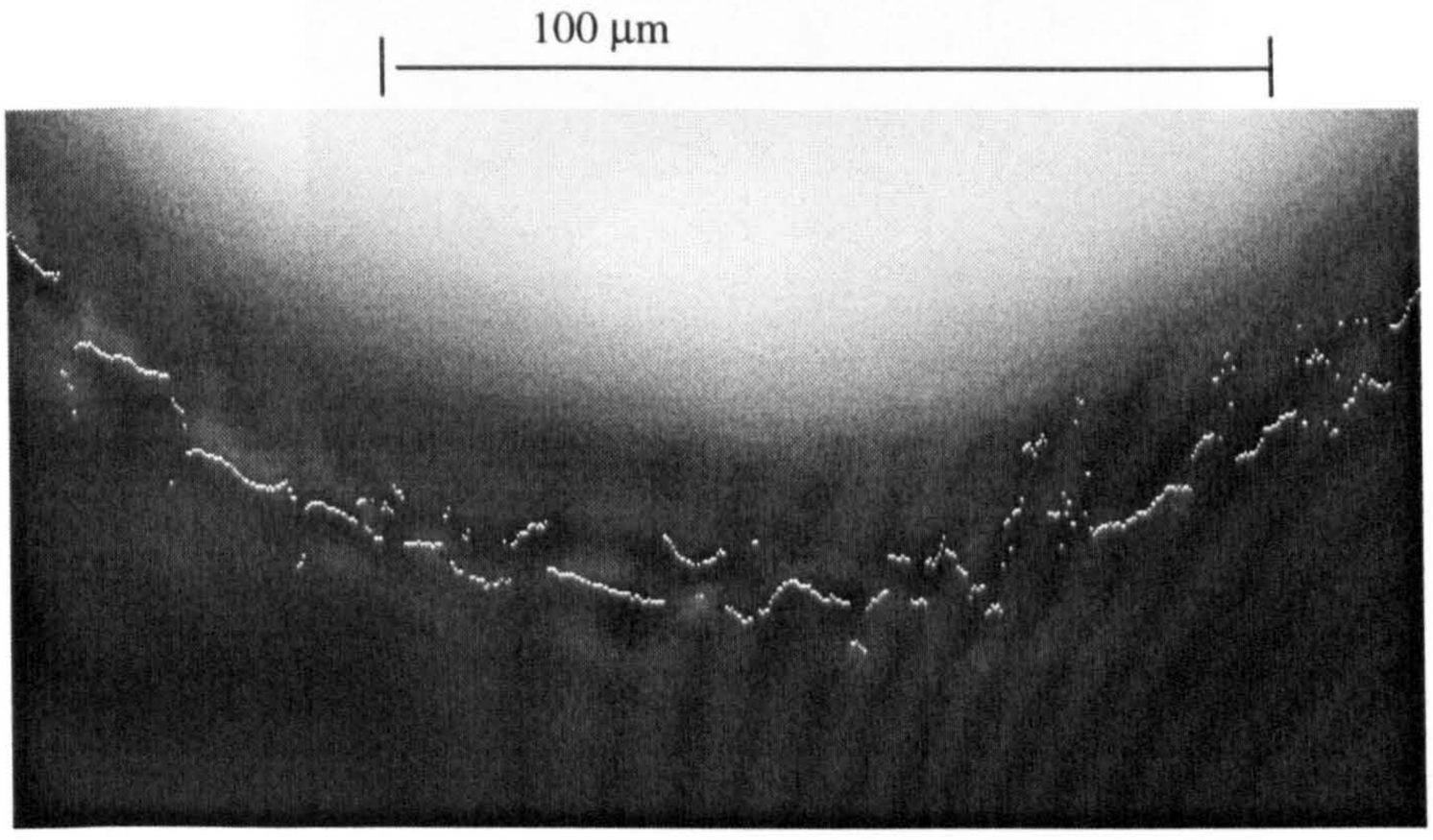

Figure 3-12 Part of rough centre curve

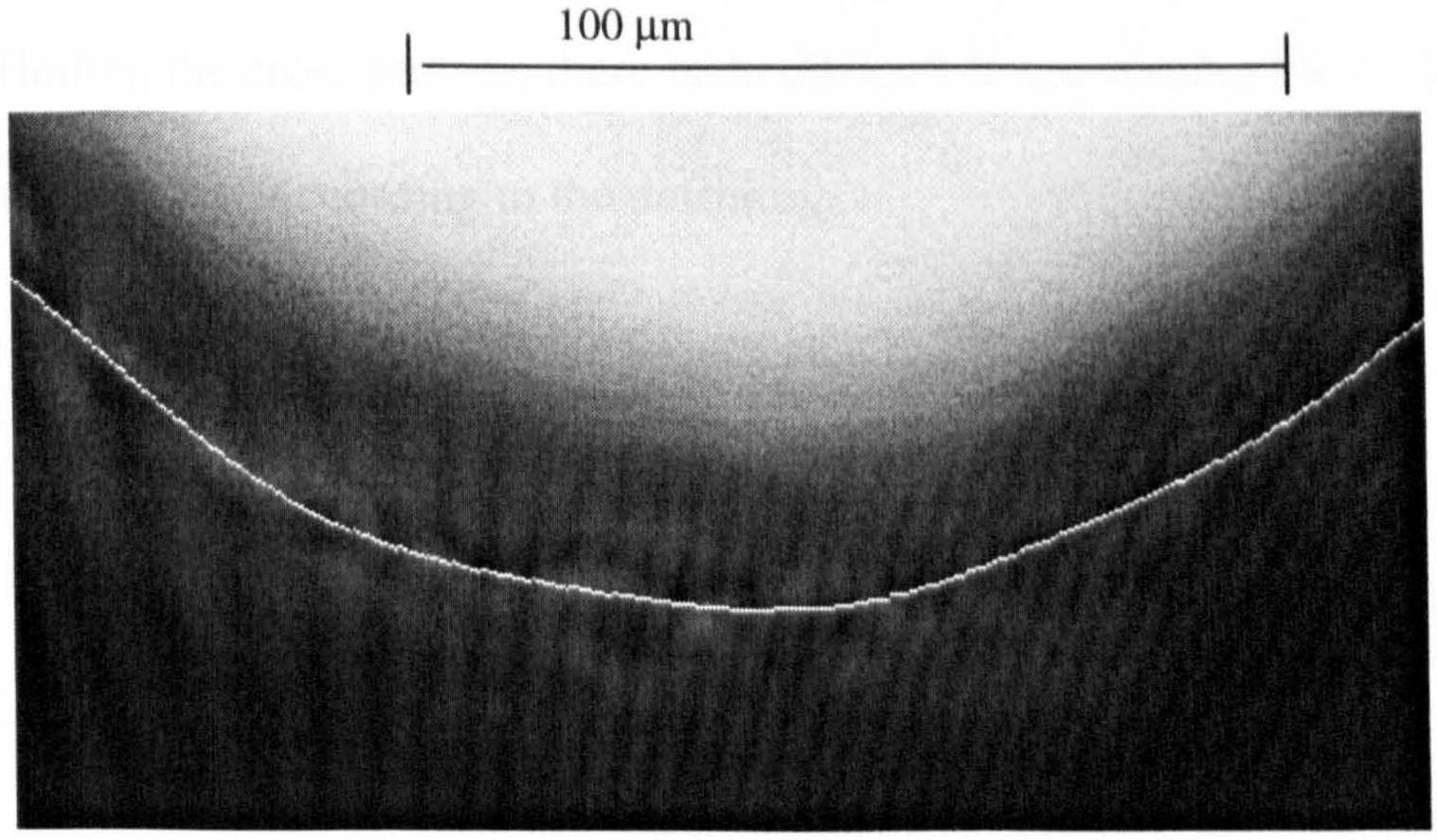

Figure 3-13 Part of centre curve

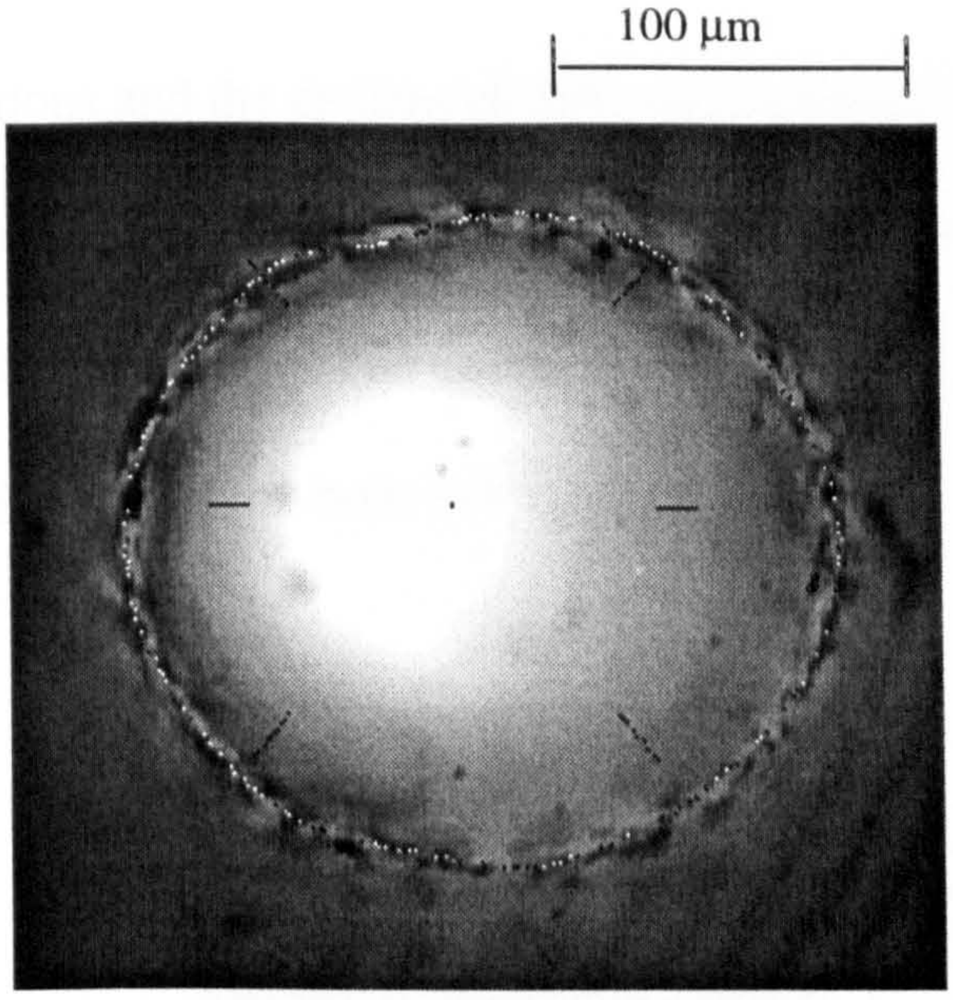

Figure 3-14 A full view of the result of random edge detection

3.2.4.2 Area and centre of the cross section

After finding the cross section, there is no difficult in calculating the area and the centre $(X_c\ Y_c)$. According to the definition:

$$area = \iint ds$$

and

$$\iint (X - X_c) ds = 0 \qquad \text{Eq 3.8}$$

$$\iint (Y - Y_c) ds = 0$$

thus:

$$X_c = \iint X ds / A \qquad \text{Eq 3.9}$$

$$Y_c = \iint Y ds / A$$

3.2.4.3 The three dimensional shape of the hole

So far, the cross sections and the centres of different positions inside the hole can be measured. They can be added to reconstruct a 3-D shape of the hole. Figure 3-15 shows this 3-D shape. The centre co-ordinates, (X_c, Y_c), enable an estimate of the straightness of the hole to be made.

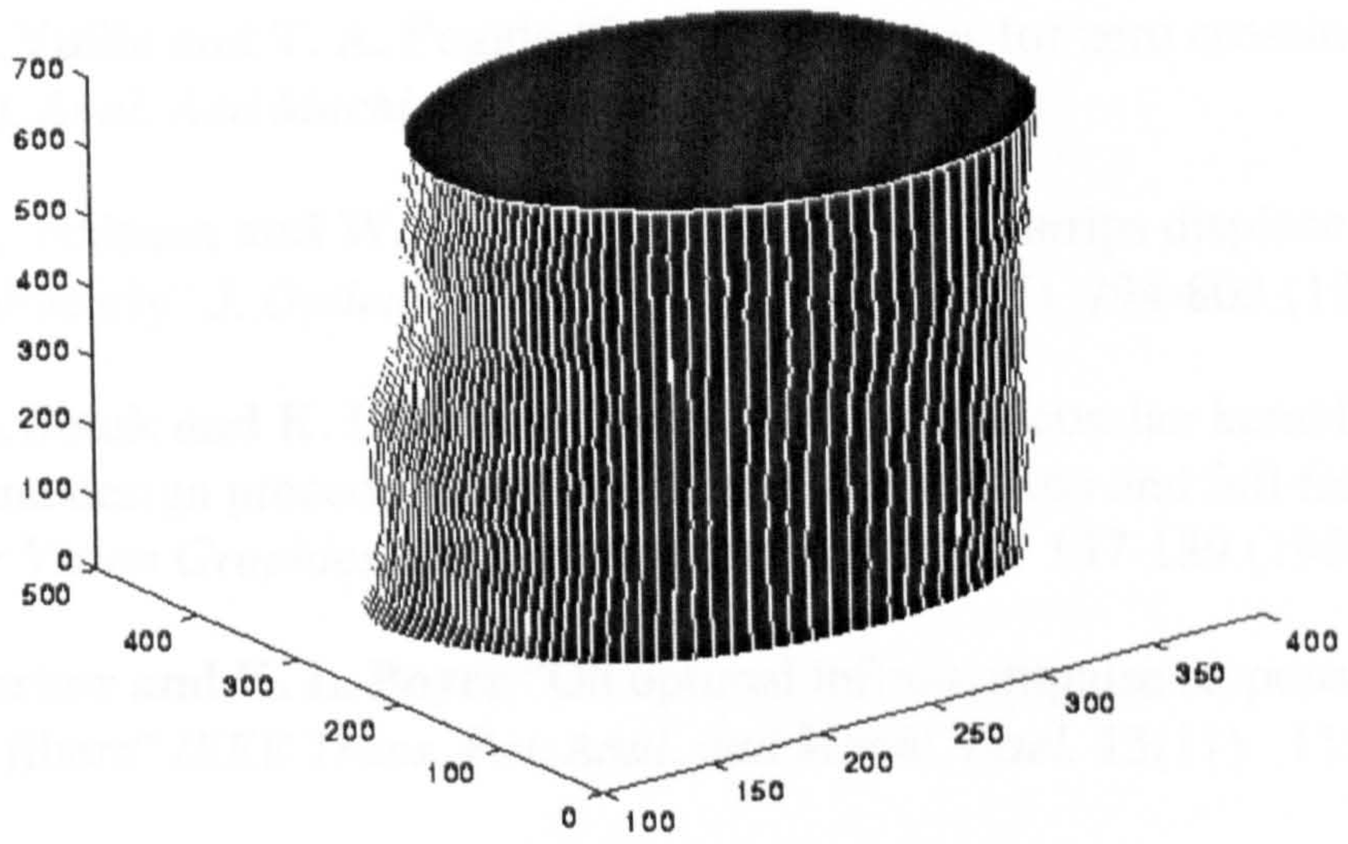

Figure 3-15 3-D shape of the hole, (μm)

References

[1] *RS Data Library 8199* " Stepper Motors" Nov. 1987

[2] *PIP-EZ MS DOS Software Library for the PIP Video Digitizer User Manual* MATROX Electronic Systems Limited Nov. 1987

[3] E. C. Ifeachor and B. W. Jervis *Digital Signal Processing-A Practical Approach* Addison-Wesley Publishing Company workingham1993

[4] R. C. Gonzalez and R. E. Woods *Digital Image Processing* Addison-Wesley Publishing Company, Reading, Mass., Workingham 1992

[5] K. Beauchamp and C. Yuen *Digital Methods for Signal Analysis* George Allen & Unwin London1973

[6] **J. W. Goodman** *Introduction to Fourier Optics* McGraw-Hill 1968

[7] **D. Ziou and S. Tabbone** "A multi-scale edge detector" *Pattern Recognition* **26**(9), 1305-1314 (1993)

[8] **P. Perona and J. Malik** " Detecting and localizing edge composed of steps peaks and roofs" *Proceeding of The third International conference on computer vision* ch.126 pp52-57 (1990)

[9] **D. Marr and H. Hildreth** "Theory of edge detection" *Proc. Roy Soc. London, B207,* 187-217 (1980)

[10] **A. L. Yuille and T. A. Poggio** "Scaling theorems for zero crossings" *IEEE Trans. Pat. Anal. And Machi. Intel.* **10**(1) 15-25 (1986)

[11] **A. C. Naiman and W. Makous** "Undetected grey strips displace perceived edges nonlinearly" *J. Optical Society of America A* **10**(5) 794-803 (1993)

[12] **G. E. Sotak and K. L. Boyer** "The Laplacian-of-Gaussian kernel: A formal analysis and design procedure for fast accurate convolution and full frame output" *Computer Vision Graphics and Image processing* **48**(2) 147-189 (1989)

[13] **S. Sarkar and K. L. Boyer** "On optimal infinite impulse response edge detection filters" *IEEE Trans. Pat. Anal. and Machi. Intel.* **13**(11) 1154-1171 (1991)

[14] **Y. Lu and R. C. Jain** "Reasoning about edges in scale space" *IEEE Trans. Patt. Anal. Machi. Intel.* **14**(5) 720-727 1992

[15] **S. Raman, S. Sarkar and K. L. Boyer** "Tissue boundary refinement in magnetic resonance images using contour-base scale space matching" *IEEE Trans. Med. Image* **10**(2) 109-121 (1991)

[16] **O. A. Zuniga and R. M. Haralick,** "Gradient threshold selection using facet model" *Pat. Recog.* **21**(5) 493-503 (1988)

[17] **J. F. Haddon** "Generalized threshold selection for edge detection" *Pat. Recog.* **21**(3) 195-203 (1988)

[18] **L. Wu and Z. H. Xie** "Scaling theorems for zero-crossings" *IEEE Trans. Patt. Anal. Mach. Intel.* **12**(1) 46-54 (1990)

[19] **J. F. Canny** "A computational approach to edge detection" *IEEE Trans. Patt. Anal. Mach. Intel.* **8**(6) 679-698 (1986)

[20] **D-C Tseng and M-Y Huang** "Automatic thresholding based on human visual perception" *Image and Vision Computing* **11**(9) 539- 548 (1993)

[21] **A. A. Masoud and M. M. Bayoumi** "Using local structure for the reliable removal of noise from the output of LoG edge detector" *IEEE Trans. Syst. Man and Cyber.* **25**(2) 328-337 (1995)

[22] A. Rosenfeld and M. Thurston "Edge and curve detection for visual scene analysis" *IEEE Trans. Computer.* **20**(5) 562-569 (1971)

[23] J. O. Eklundh, T. Elfving and S. Nyberg "Edge detection using the Marr-Hildreth operator with different sizes" *Proc. 6th Int. Conf. On Pattern Recognition* Munich, Germany, 1109-1112 (1982)

[24] F. Bergholm "Edge focusing" *IEEE Trans. Patt. Anal. Mach. Intel.* **9**(6) 726-741 (1986)

[25] V. Lacroix "The primary raster: a multiresolution image description" *Proc. 10th Int. Conf. Pattern Recognition* 903-907 (1990)

[26] D. J. Williams and M. Shah "Edge contours using multiples scales" *Computer Vision and Graphics Image Process* **51**() 256-274 (1990)

[27]A. Witkin "Scale-space filtering" *Proceeding of Int. Joint Conf. Artificial Intelligence* Karlsruhe, West Germany, 1019-1021 1983

[28] J. Koenderink "The structure of image" *Biol. Cybern* **50** 363-370 (1984)

[29] J. Babaud, A. P. Witkin, M Baudin and R. O. Duda "Uniqueness of the Gaussian kernel for scale-space filtering" *IEEE Trans. Patt. Anal. Mach. Intel.* **8**(1) 26-33 (1986)

[30] P. Perona and J. Malik "Scale-space and edge detection using anisotropic diffusion" *IEEE Trans. Patt. Anal. Mach. Intel.* **12**(7) 629-639 (1990)

[31] M. Nitzberg and T. Shiota "Nonlinear image filtering with edge and corner enhancement" *IEEE Trans. Patt. Anal. Mach. Intel.* **14**(8) 826-833 (1992)

[32] G. Gerig , O. Kubler, R. Kikinis and F. A. Jolesz "Nonlinear anisotropic filtering of MIR data" *IEEE Trans. Medical Imaging* **11**(2) 221-232 (1992)

[33] X. P. Li and T. W. Chen "Nonlinear diffusion with multiple edginess thresholds" *Pattern Recognition* **27**(8) 1029-1037 (1994)

[34] R. N. Strickland and D. K. Chang "Adaptable edge quality metric" *Optical Engineering* **32**(5) 944-951 (1993)

[35] M. Gokmen and C-C Li "Edge detection and surface reconstruction using refined regularization" *IEEE Trans. Patt. Anal. Mach. Intel.* **15**(5) 492-499 (1993)

4. Applications

The industrial background of measuring the dimension of small holes has been given in Chapter 1. The holes produced by spark erosion or pulsed laser. The shape of the hole is not cylindrical: the measurement of the internal surface finish and straightness becomes a problem. The method described in Chapter 3 can be used to deal with these measurements: it measures the cross sections of different positions within the hole and finds the areas of these cross sections. It also calculates the centre of every cross section and connects those centre points and cross sections to give a 3-D view of the hole. In this chapter the applications of the method to different problems are described. The software used for the different applications is basically the same: to locate the centre curve of the in-focus-strips of every image as described in Chapter 3. In the following sections only the special aspects are described.

4.1 Measurement of Cummins diesel injector hole

4.1.1 About the injector

The injector is shown in Figure 1-2. The dimension of the top part of the injector is represented in Figure 4-1. The hole is approximately 0.2 mm in diameter and 0.6-0.8 mm in depth (depends on the models). The angle between the axis of the hole and the axis of the injector is approximately 70 degrees. The cavity at the

bottom of the hole is quite small. It is approximately 1.2 mm in diameter as shown in Figure 1-6.

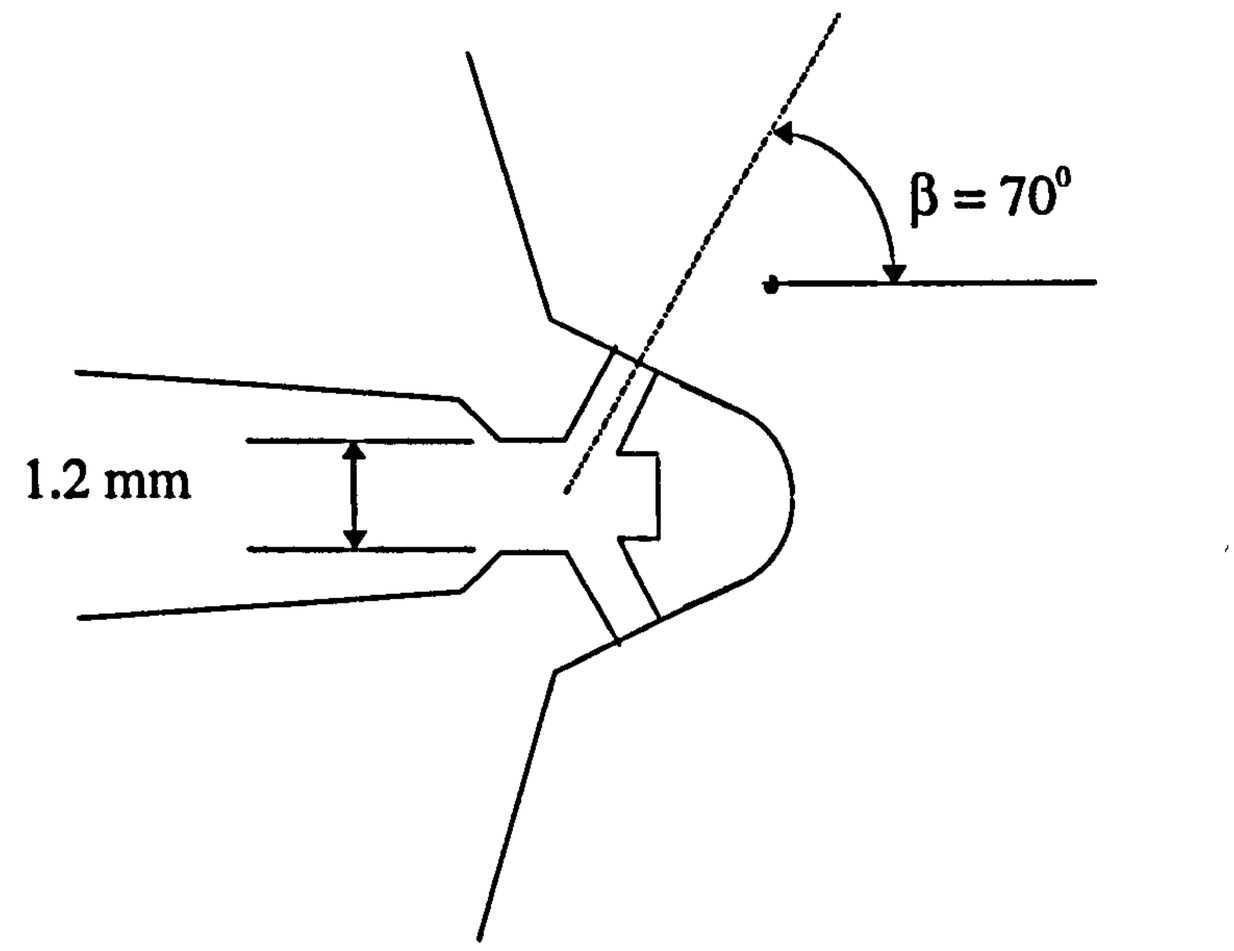

Figure 4-1 The dimensions of the tip part of the injector

4.1.2 Illumination.

As mentioned in the section 2.2.2.1, in order to view the internal surface, the light has to illuminate the hole from the restricted end. To achieve this, a flexible light guide[1] (a polymer fibre with 1 mm in diameter) is used. The end of the flexible light guide is roughly polished into a defined angle, so that the internal surface can be evenly illuminated. The refractive index of the flexible light guide n= 1.5 and $\beta = 70^0$. From Eq 2.3(p.46) it can be calculated that the angle of fibre φ is equal to 38.4^0.

[1] Ultrafine Ltd, Brentford Middx UK

4.1.3 The position of the hole

All the optical components in this system are fixed and do not move during the measurement, the only movable part is the injector which is fixed on a 5 degree of freedom stage. The axis of the optical system is the reference of the measurement. The image of the hole is always located inside the detection area. This position of the hole is adjusted prior to the measurement as described in Section 2.4.4. Figure 4-2 shows the 5 degree of freedom stage. The stage has two tables. Table one can be moved in three transversal directions controlled by both manual and computer means with the accuracy of 1 μm. Table two is mounted on top of table one, it can rotate in two directions by adjusting R1 and R2.

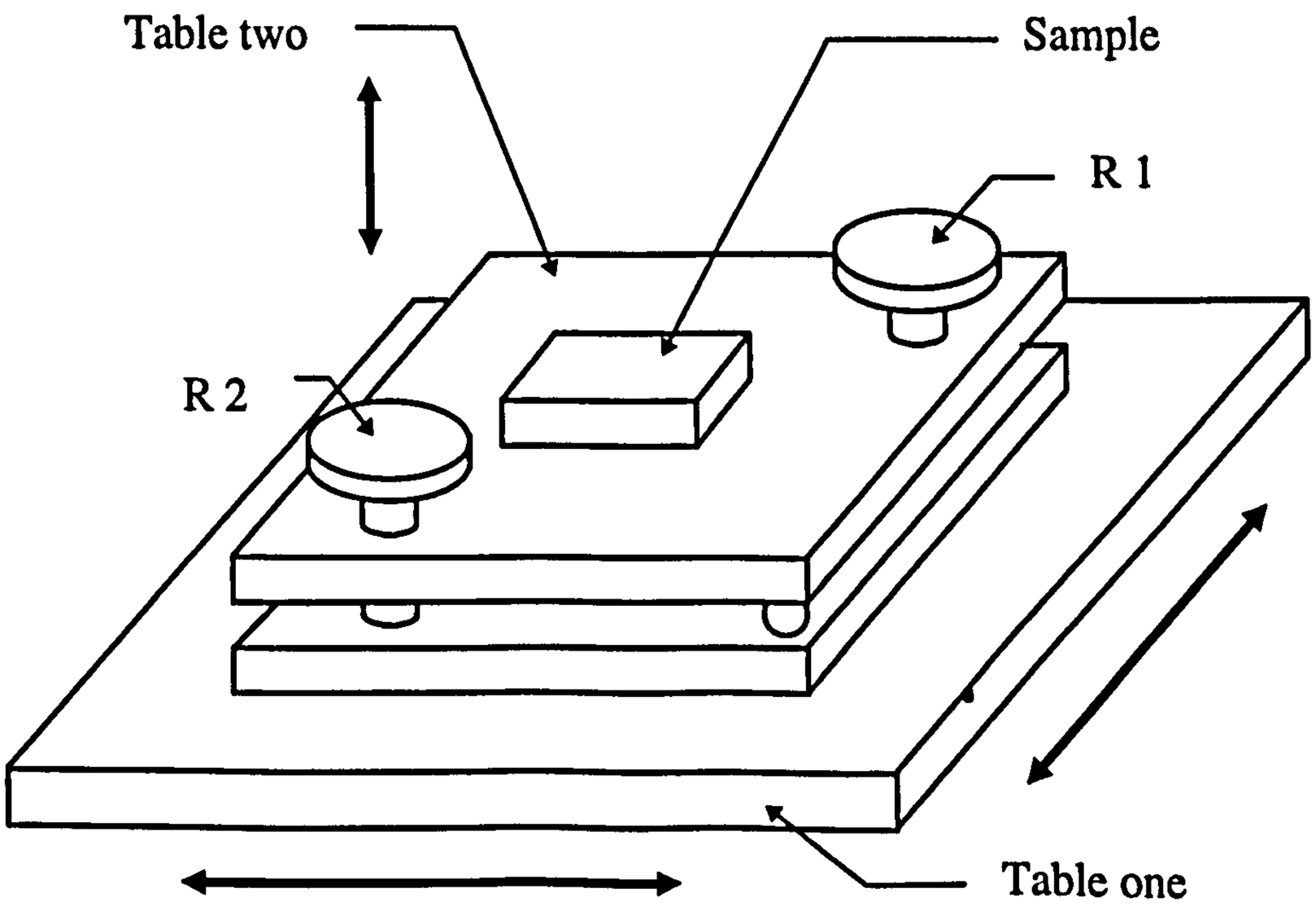

Figure 4-2 The 5 degree of freedom stage: Table one can be moved transversally. Table two is mounted on table one and can rotate in 2 directions by adjusting R1 and R2.

4.1.4 The objective lens

The magnification of the objective used in this measurement is × 5. The numerical aperture is 0.05. Due to the physical limitations of the diesel injector, at least a 6 mm working distance is required to view the hole, because that the point A in Fig 2-9(a) (p. 44) will stop the objective moving close to the hole.

4.1.5 Results

Figure 4-3 is the 3-D shape of the hole based on 22 cross sections with an interval of 25 μm. The centres of these cross sections are also connected to give a measure of the straightness. The accuracy of this measurement is determined by how well the centre curve of the strip is located. Location of the centre curve of the strip using the method achieved with a one third strip width error. In this measurement, the width of the strip is approximately 20 μm. Thus, the accuracy is ± 3 μm as drawn in Figure 4-4.

A way to increase the accuracy is to use a more powerful objective with a larger N.A. This kind of objective increases the accuracy in two ways:

1) By reducing the depth of the field (DOF), the width of the in-focus-strip is reduced.

2) As the in-focus-strip is wider within the image, the error of the centre curve location can be reduced compared with the width of the strip.

Figure 4-5 gives an example, where the DOF is reduced to 15 μm, and the error is reduced to one tenth of the width of the strip. Therefore the accuracy is increased

to ± 1.5 μm. The disadvantage is that only a part of a hole can be deal with in every image. It is further discussed in Chapter 7.1.1.1.

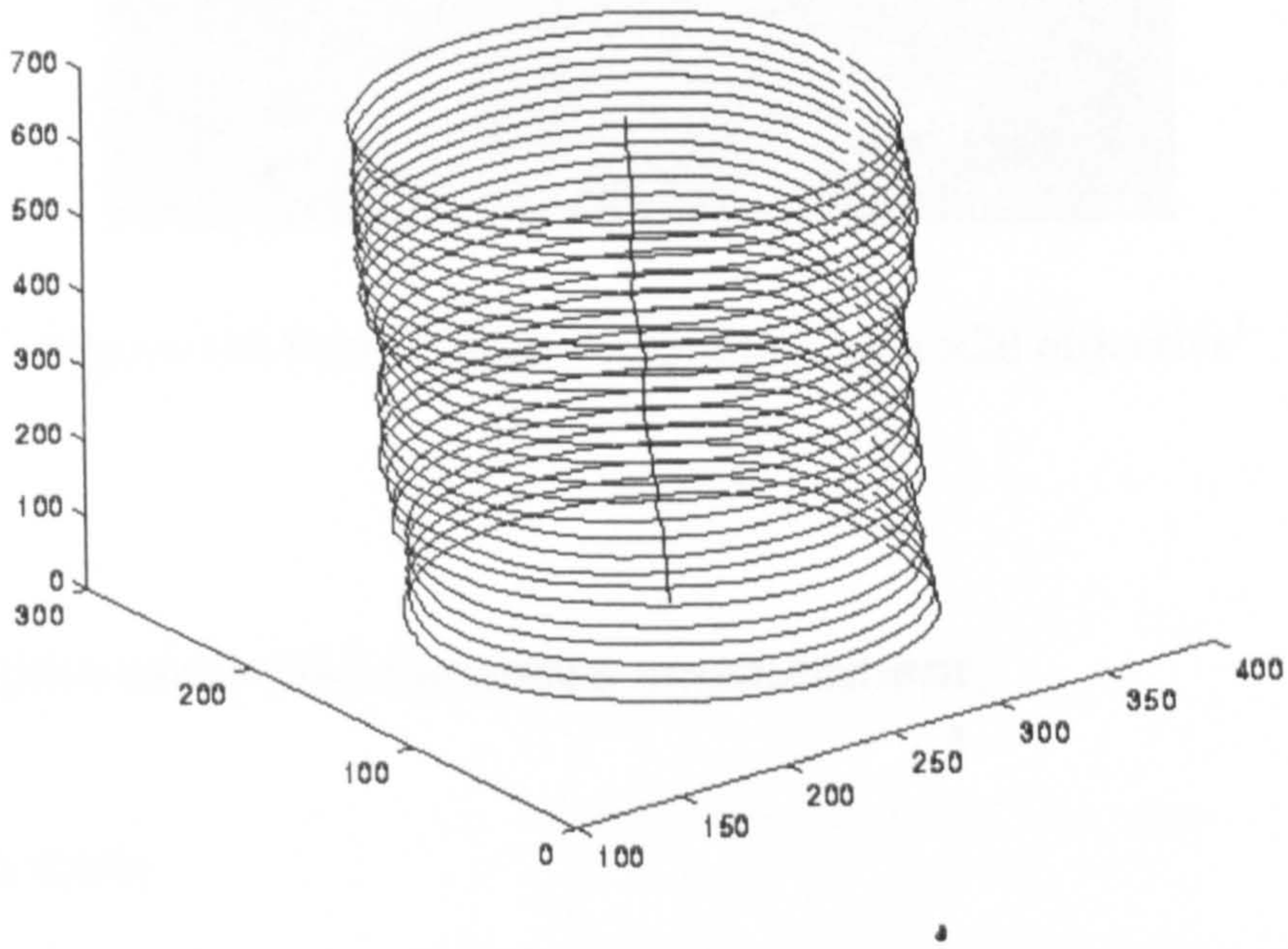

Figure 4-3 Shape of the hole (μm)

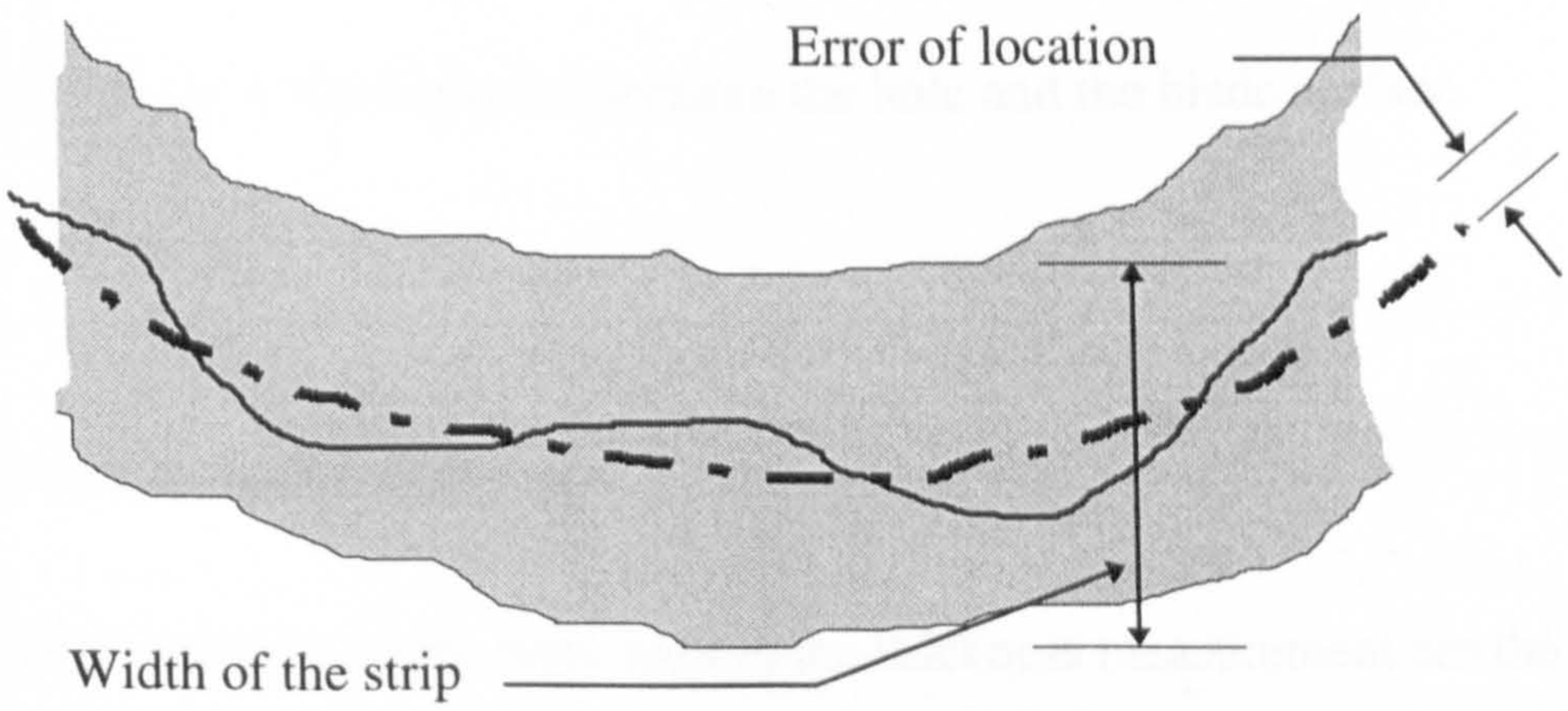

Figure 4-4 Random edge detection and errors

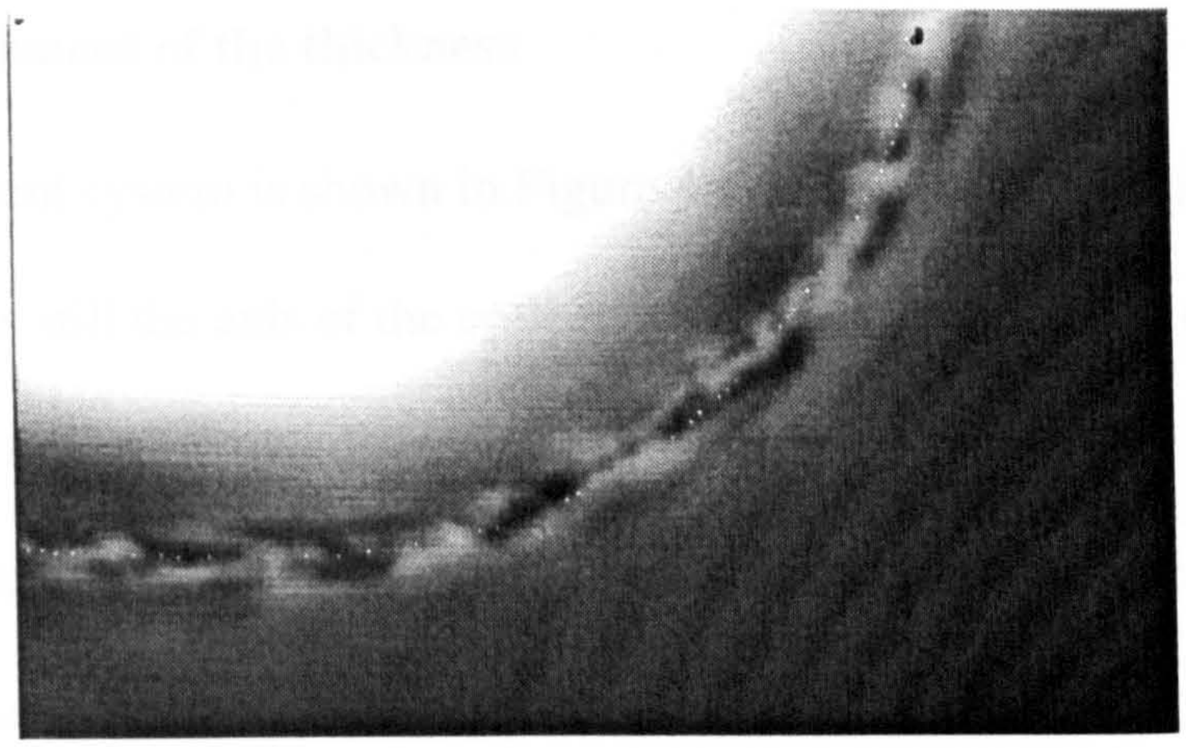

Figure 4-5 Part of the hole obtained by a ×20 objective[2]

4.2 Turbine blade wall thickness measurement

4.2.1 The blade

The turbine blade shown in Fig 1-3 is used in a Rolls-Royce jet engine. The holes are used to carry coolant through a turbine blade. They are approximately 6 mm long and 0.25 mm in diameter. A special requirement in this problem is the measurement of the thickness between the hole and the blade surface.

4.2.2 Illumination and stage

The illumination and the stage used in the thickness measurement are the same as that used for the diesel injector measurement. Because of the angular difference between the turbine blade and the fuel injector, the end of the flexible light guide is polished to a different angle.

---

[2] Leica, Milton Keynes, UK

4.2.3 Measurement of the thickness

The measurement system is shown in Figure 4-6. The reference of the measurement is still the axis of the optical system. The thickness is measured by measuring the following two distances:

1) D_o, the distance from the outside surface of the blade to the optical axis.

2) D_i, the distance from the inside surface to the optical axis.

The thickness, D_t, of the internal surface to the outside blade is therefore equal to $D_o - D_i$.

There are several ways to measure D_o. A displacement transducer[3] which was available in the laboratory was used for this measurement. The range is 15 mm with a resolution of 1 μm. The transducer was fixed into the system. The needle of the probe was laid inside the object plane. When the hole was moved up and down, the needle only moved inside the object plane. It therefore measured the distance D_o.

The second distance is measured by random edge detection which has been used in the cross section measurement of injector hole. After detecting the centre curve of the random edge, the distance from the curve to the axis of the system, which is the distance from the internal surface to the axis D_i, can be determined. For this measurement, only part of the hole was viewed. Thus a more powerful objective ($\times 20$ and $NA = 0.3$) is used. However, this objective could not increase the accuracy very much. The reason is that the hole will limit the numerical aperture

---

[3] TESA Swiss

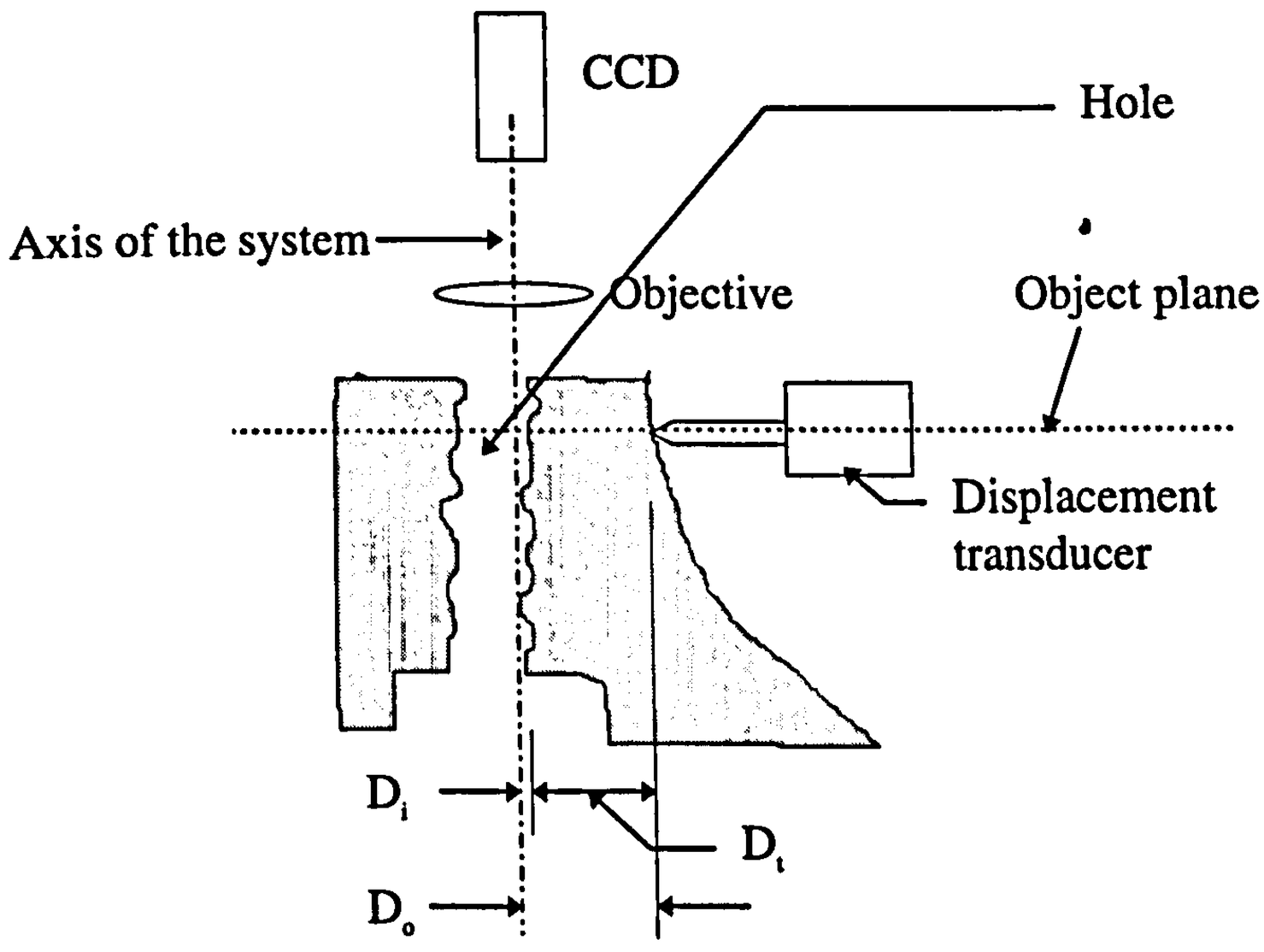

Figure 4-6 Wall thickness measurement system

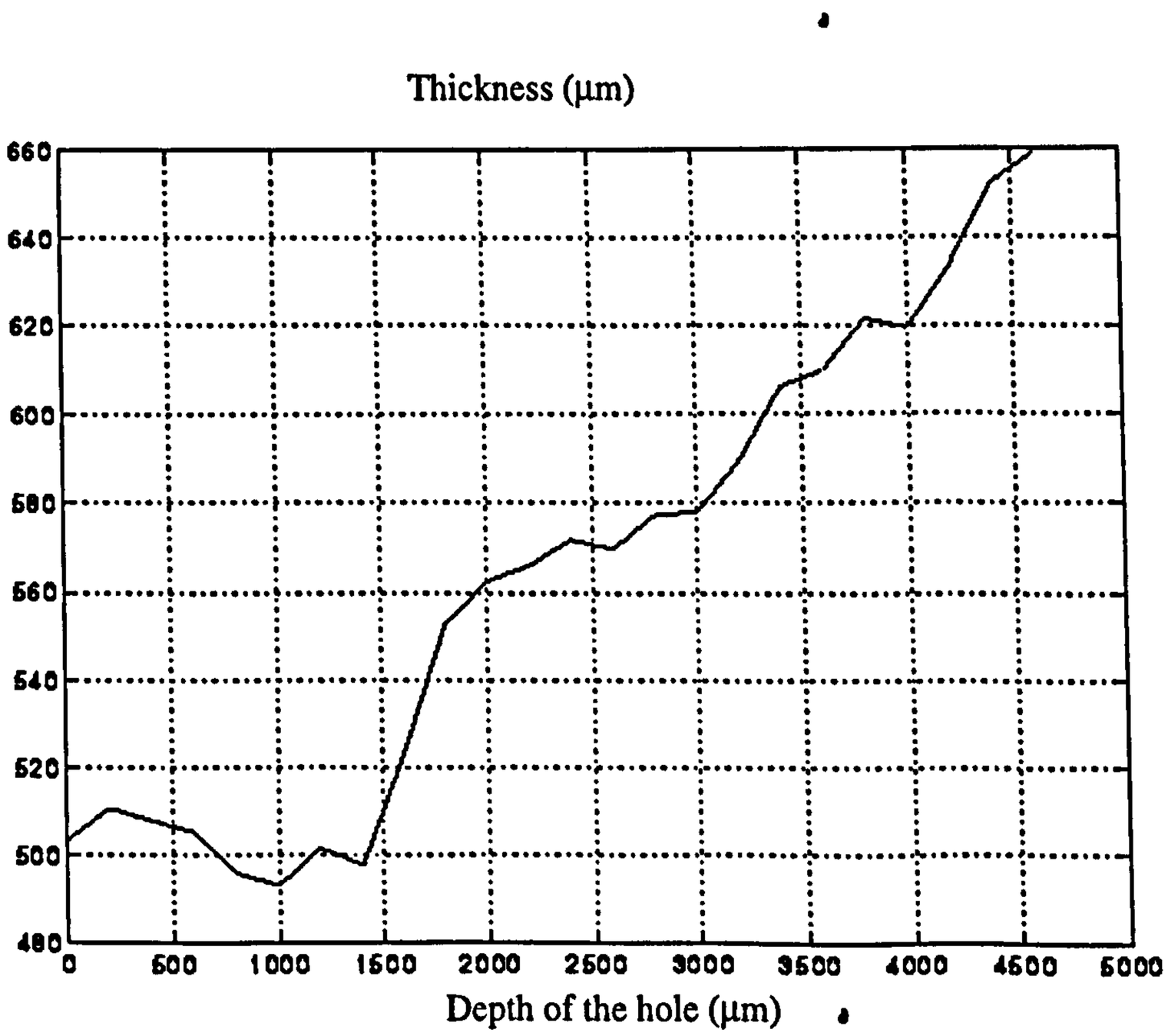

Figure 4-7 The thickness of the wall

of the optical system. It is also discussed in section 5.1.1.1. Figure 4-7 is the result: the thickness of the wall of a hole.

4.3 Courtaulds' synthetic spinnerette hole measurement

4.3.1 The injector

The injector of Courtaulds' synthetic spinnerette is used to extrude polymer into yarn. The shape and size of the hole of the injectors need to be measured. The hole is cone-like with diameter range from 0.08 to 0.7 mm and 1.4 mm in depth. Fortunately both ends of the hole are freely accessible. Figure 4-8 shows the injector. Because of the large diameter range, it is not practice to measure them with one magnification. The most important part of the hole for designers is the smaller diameter side. It is therefore measured.

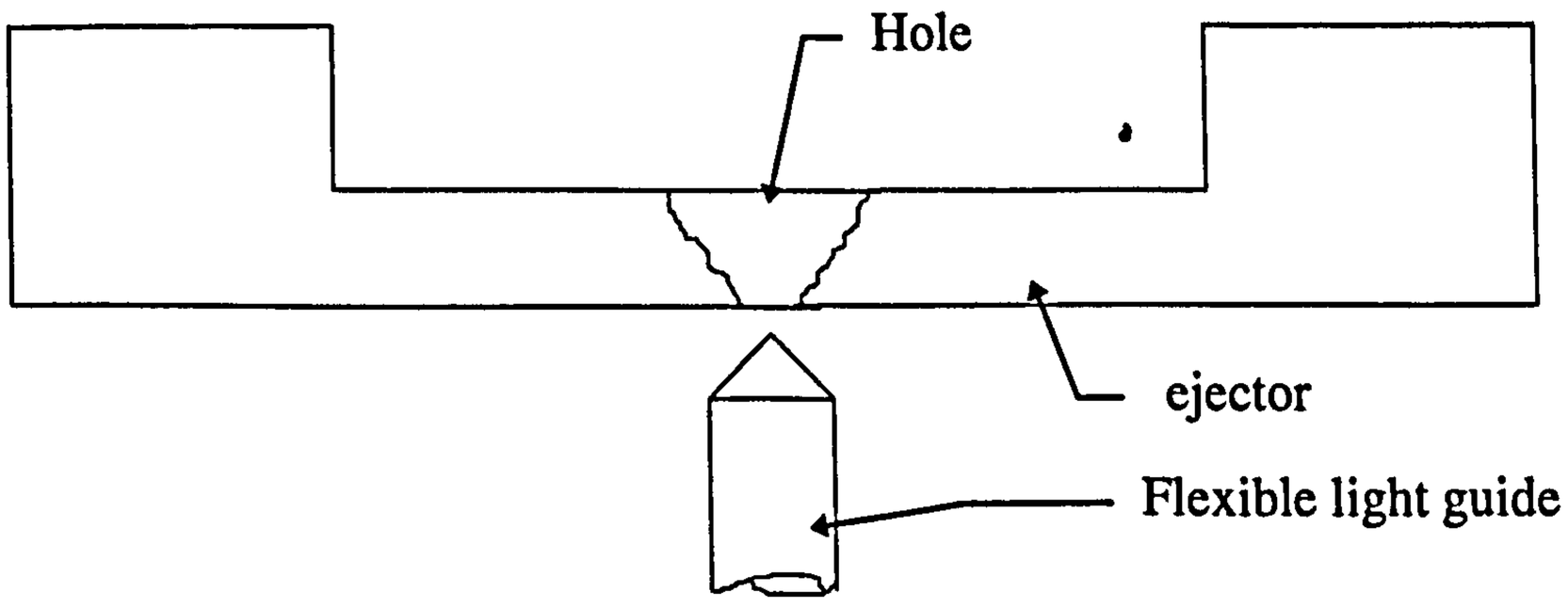

Figure 4-8 The hole of Coutaulds' injector

4.3.2 Illumination

In order to illuminate the internal surface evenly, a special end of the light guide is designed to investigate the Courtaulds' spinnerette holes. To achieve this, the end of the fibre is not polished but cut into a cone-like shape. In this way, the light can be diverted in a larger cone and the fibre can be placed close to the end of the hole. The different end shape of the light guide influences the illumination. Two kinds of illumination are shown in Figure 4-9, where θ is the half apical angle of the cone. The light γ always goes forwards to illuminate the hole. The light η goes forward only if the end of the light guide is sharp enough (Figure 4-9(b)). Referring to the triangle ABC in Figure 4-9 (a), an approximate judgement can be made: if the angle ACB larger than $\pi/2$, the light η goes forward, if it is smaller than $\pi/2$, the light η goes backward (Figure 4-9 (a)).

Because

$$\angle CBA = \theta\ ,\ \angle BAC = 2\theta,$$

then :

$$\angle ACB = \pi - 3\theta.$$

Therefore, to get good illumination, θ should be smaller than $\pi/6$.

4.3.3 Results

The 3-D shape of the hole is shown in Figure 4-10. It covers a depth of 0.4 mm.

Figure 4-11 gives the relationship between the depth of the hole and its diameter.

The accuracy is ± 3 μm, the same as that of injector measurement.

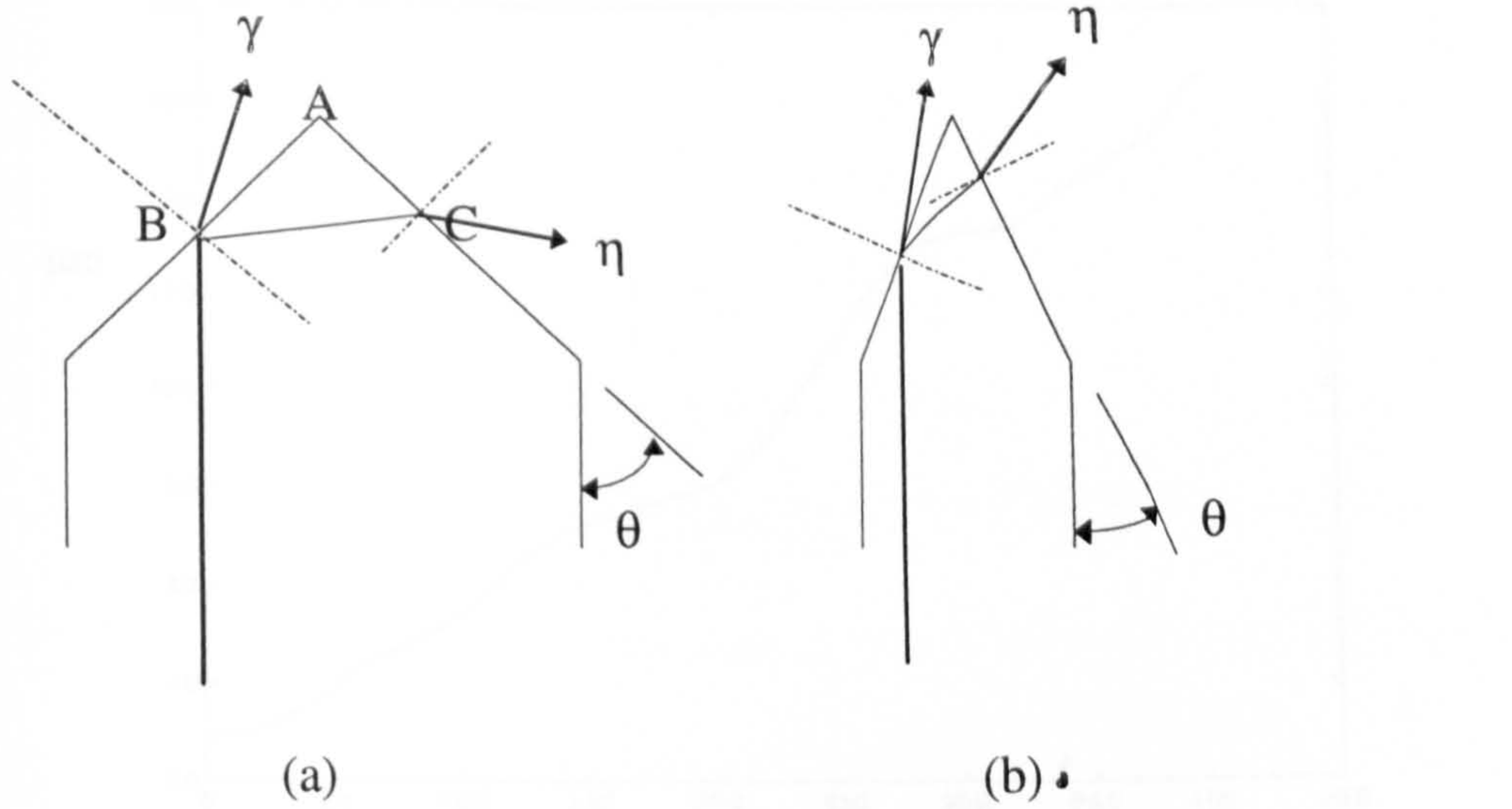

(a) (b)

Figure 4-9 The explain of the illumination: (a) When θ is larger then π/6 some light is diverted back. (b) When θ is smaller then π/6 all light is diverted forward.

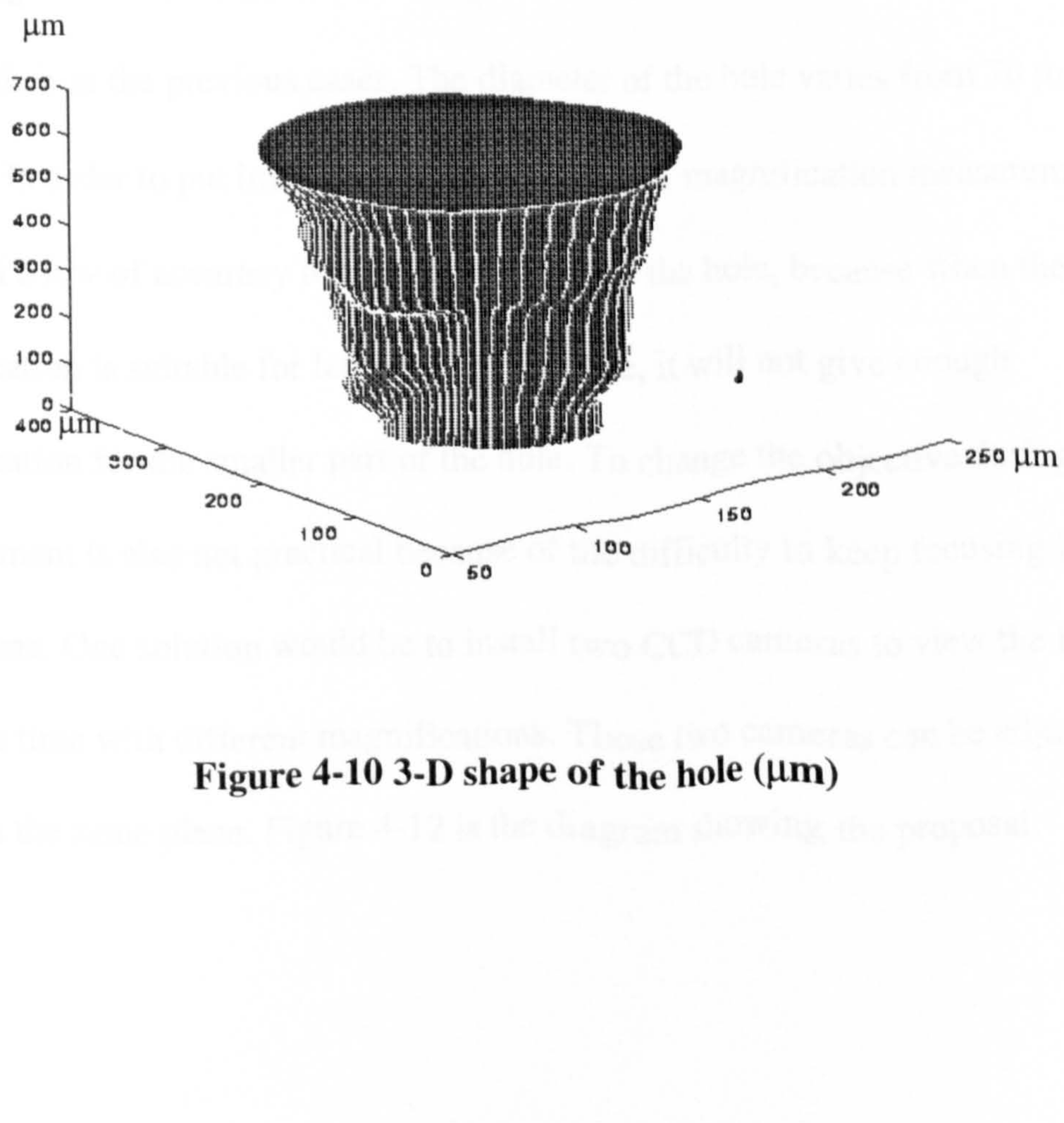

Figure 4-10 3-D shape of the hole (μm)

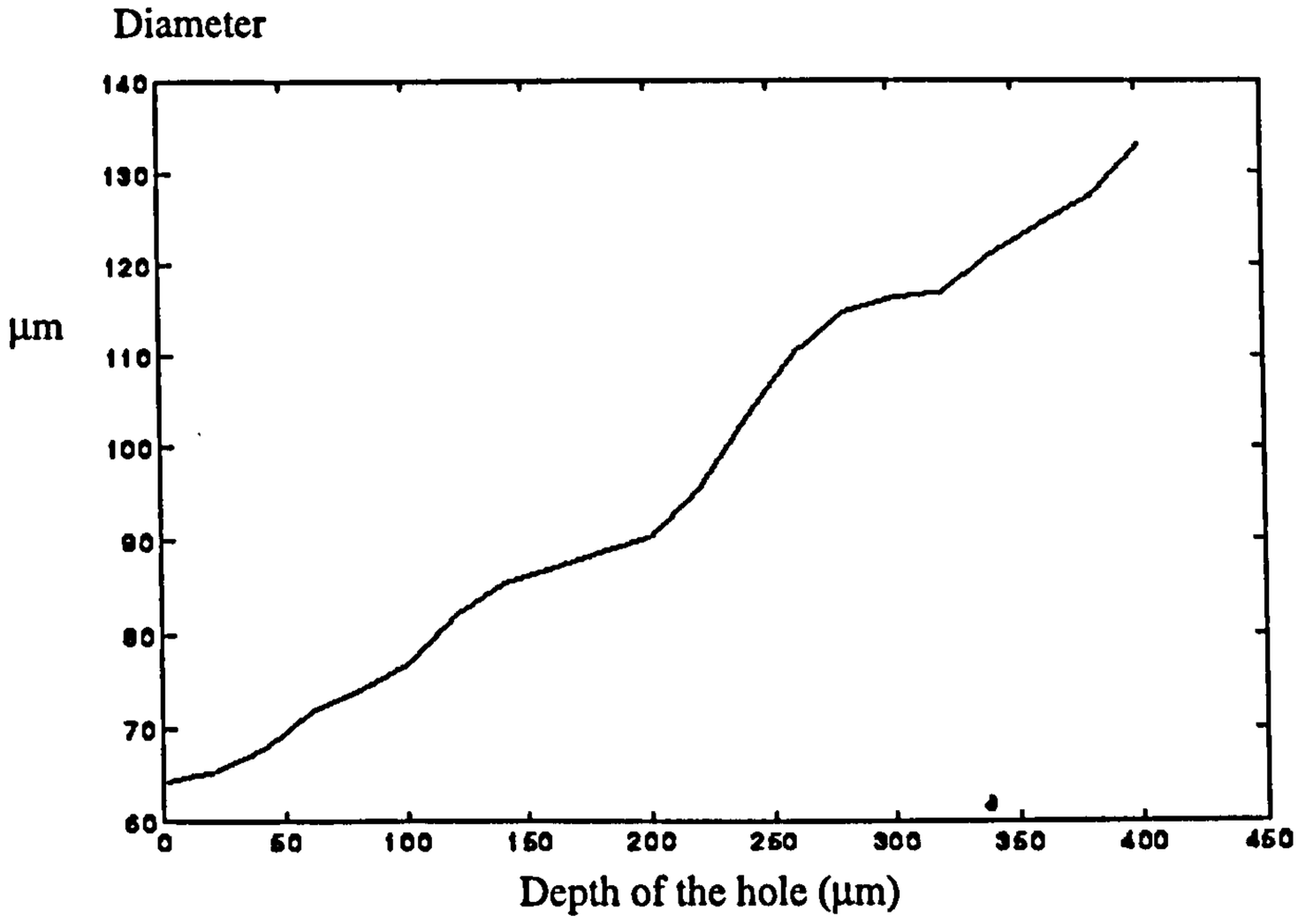

Figure 4-11 The plot of diameter- depth

4.3.4 Limitations and further work

The change of diameter makes the complete hole measurement more difficult to achieve than in the previous cases. The diameter of the hole varies from 70 μm to 500 μm. In order to put image inside the screen, one magnification measurement results in a low of accuracy for the smaller part of the hole, because when the magnification is suitable for large part of the hole, it will not give enough magnification for the smaller part of the hole. To change the objective during the measurement is also not practical because of the difficulty to keep focusing in the same plane. One solution would be to install two CCD cameras to view the hole at the same time with different magnifications. These two cameras can be adjusted to focus on the same plane. Figure 4-12 is the diagram showing the proposal.

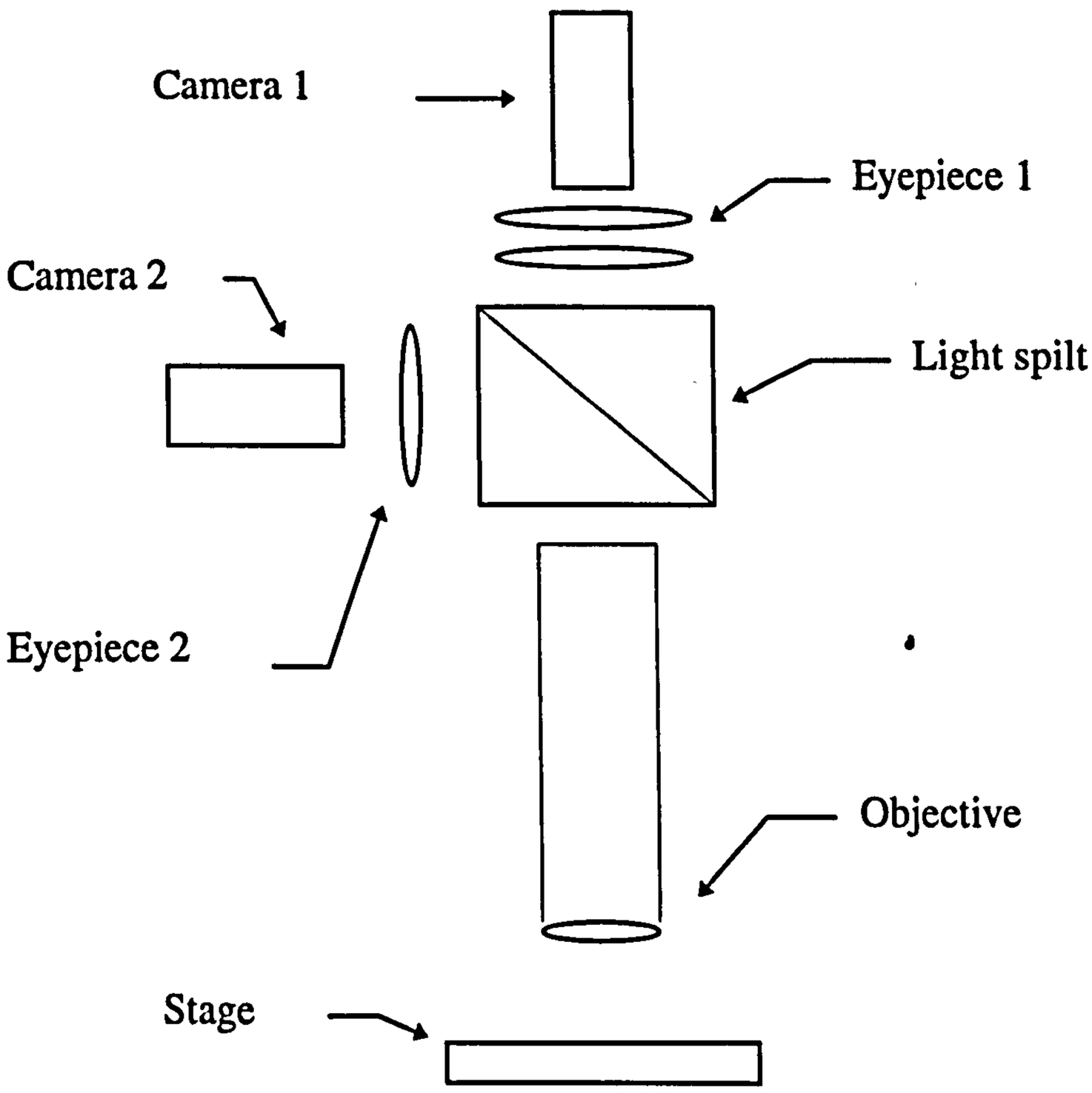

Figure 4-12 A proposal to measure cone-like holes

5. Reconstructing shadow image and measuring surface roughness inside a hole

The next step in this thesis has been to measure the internal surface roughness of a hole. To achieve the measurement, a shadow image of the internal surface is first reconstructed. A microscope is used to investigate the internal dimension of the hole. However, only a narrow strip of the internal surface can be imaged clearly because of the limited depth of field (DOF). This strip is called the in-focus-strip, as mentioned in section 2.4.2. A method that is able to reconstruct the shadow of the internal surface of the hole is developed and described in this chapter.

Shape from shading (SFS) is a research field involving the recovering of the shape of an object from its shading image. A review of SFS is also given in this chapter. This technique has been studied for the possibility of internal surface finish measurement.

A statistical method finally developed to calculate the surface roughness parameters R_a and R_q of the surface from the shadow image. The method was examined by comparing the result with a stylus measurements of a know flat surface made by spark erosion.

5.1 Reconstructing the shadow image of the internal surface of a hole

The shadow image is constructed from a set of in-focus-strips. The form of the strip is described in chapter 2. The optical set-up used is similar to that used in the cross section measurement as shown in Figure 2-9. However, because only part of the internal surface is imaged, a more powerful objective is used (×20). In this section, the character of a single strip image and the image processing applied to it are discussed.

5.1.1 In-focus-strip in single image

In order to understand the nature of the strip image, it is necessary to take account of the limitation imposed by the viewing microscope. Figure 5-1 explains the form of in-focus-strip. The strip is the image of that internal surface which located inside the DOF. The following analysis is based on the theory of microscopy[1].

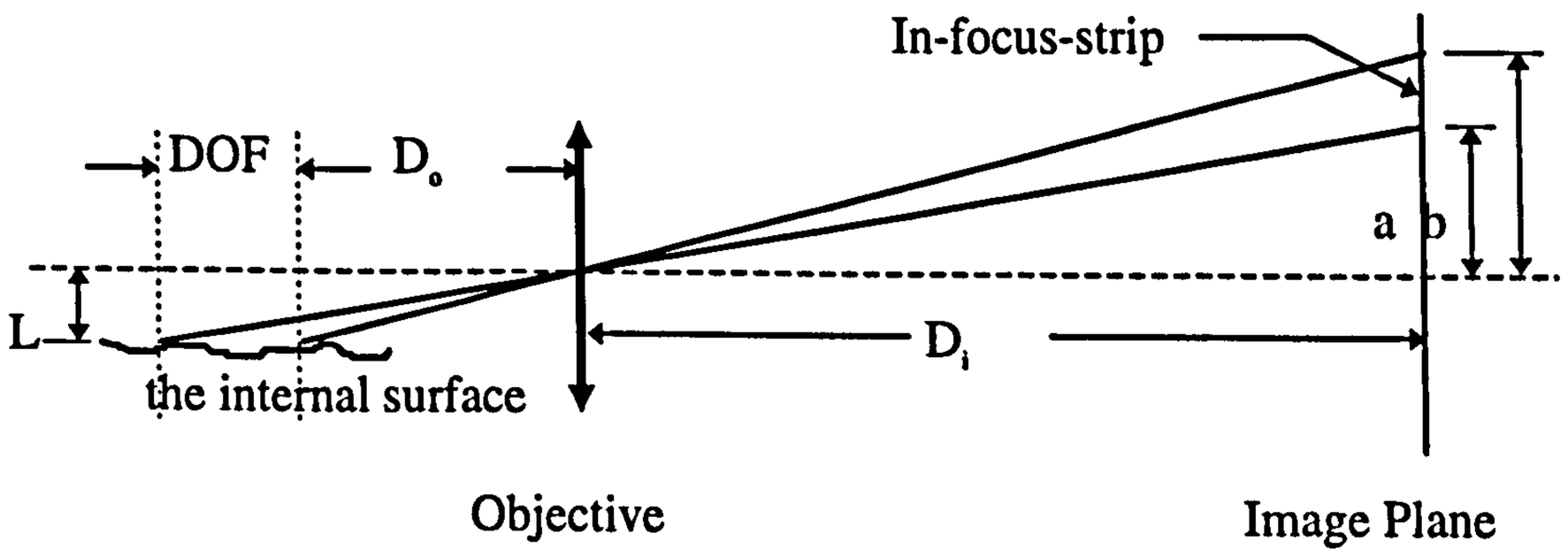

Figure 5-1 The formation of the in-focus-strip

5.1.1.1 Effective numerical aperture

The numerical aperture (*N.A.*) of an objective is defined as $N.A. = n\ sin(\theta)$, where n is the refractive index of the medium; θ is half the apical angle of the cone of light rays accepted by the objective, as shown in Figure 5-2 (a). The *NA* is an important aspect of the optical system. It can be seen from Figure 5-2 (b) that the *N.A.* of the system is reduced by the top of the hole when the deeper part of the hole is investigated. If $N.A._{effective}$ is used to represent the real *N.A.* of the system, it can be found that the relationship between the *N.A.* of the objective and the $N.A._{effective}$ is:

$$N.A._{effective} = \begin{cases} N.A. & x \le R / \sqrt{(1/N.A.)^2 - 1} \\ R / \sqrt{x^2 + R^2} & x > R / \sqrt{(1/N.A.)^2 - 1} \end{cases} \qquad \textbf{5.1}$$

where R is the radius of the hole, and x is the depth from the end of the objective to the focus plane.

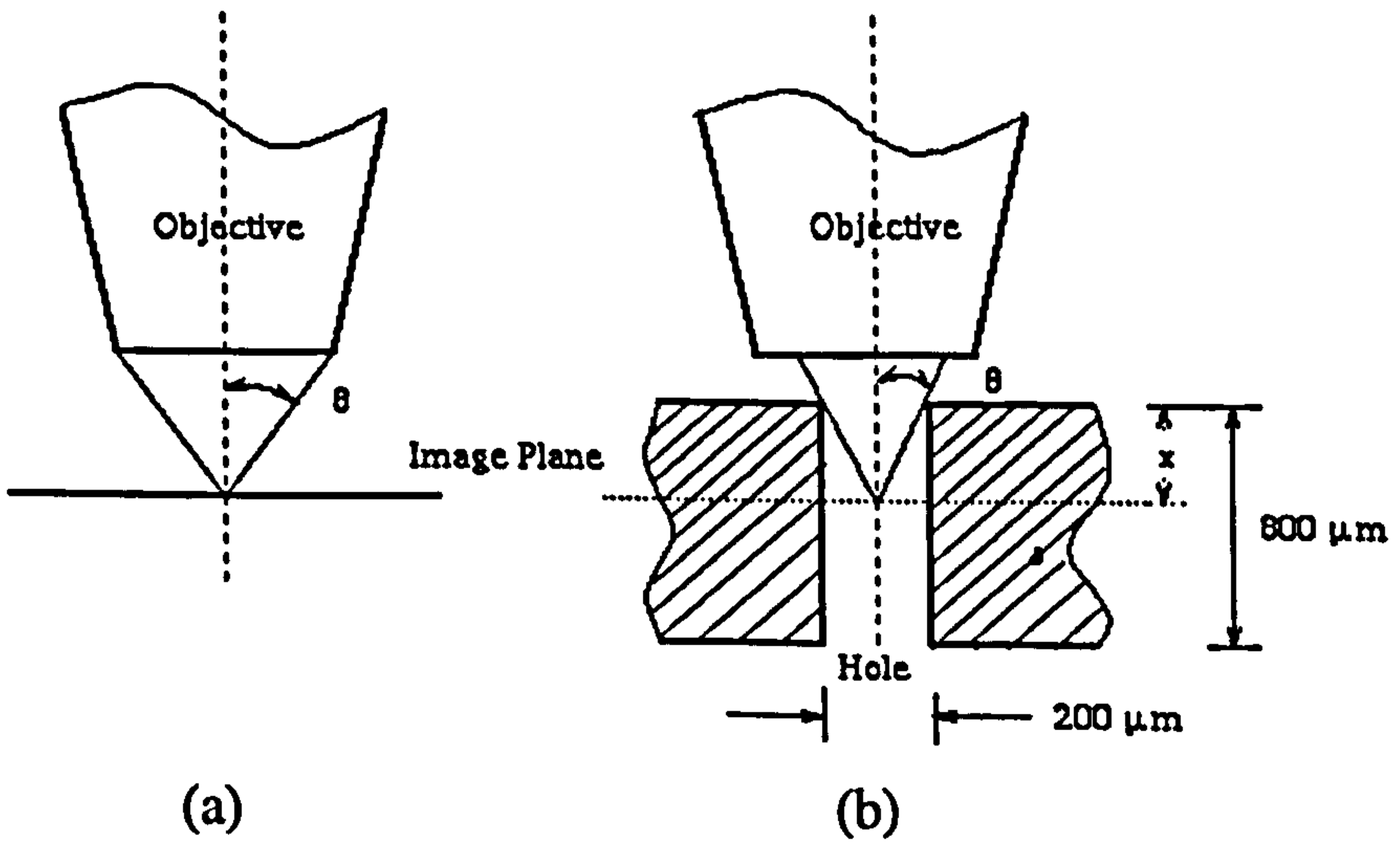

Figure 5-2 (a) N.A. of an objective (b) N.A. reduced by hole

5.1.1.2 Depth of field and width of the strip

Figure 5-1 shows the relationship between DOF, width of the in-focus-strip (*b-a*) and the dimension of the system, where:

- *DOF* ---------- Depth of field;
- *L* ---------- the distance from the internal surface to the axis of the optical system;
- D_{on} ---------- the nearest object distance inside DOF;
- D_{of} ---------- the farthest object distance inside DOF;
- D_o ---------- $(D_{on} + D_{of})/2$, the average object distance;
- D_i ---------- the image distance;
- *b - a* ---------- the width of the in-focus-strip on the image.

In the measurement, the depth of the field (DOF) is approximately 25 μm and D_o is approximately several millimetres. That is $DOF << D_o$. Referring to Figure 5-1, the relationship between the DOF and the width of the strip on the image can be found in following way:

$$a = D_i L / (D_o + DOF/2) \qquad 5.2$$

$$b = D_i L / (D_o - DOF/2) \qquad 5.3$$

Therefore

$$b - a = \frac{LD_i}{D_o^2 - (DOF/2)^2} DOF \approx \frac{LD_i}{D_o^2} DOF$$

$$\cdot = M \frac{L}{D_o} DOF, \qquad 5.4$$

where M is the axial magnification of the optical system.

5.1.1.3 Change of horizontal magnification inside the DOF

The magnification changes with the object distance, as shown in Figure 5-1. If M_n and M_f represent the nearest and farthest magnifications, then

$$M_n = D_i / D_{on} \qquad 5.5$$

$$M_f = D_i / (D_{on} + DOF) \qquad 5.6$$

Because D_{on} is always bigger (several mm) than DOF (approximately 25μm), Eq 5.4 can be written as :

$$M_f = M_n (1 - DOF/D_{on}) \cong M_n \qquad \text{Eq } 5.7$$

It is therefore reasonable to assume that the magnification of the image is uniform over the range of the depth of field of the optical system.

5.1.1.4 The summation of the in-focus-strip

For the Cummins' injector measurement, the radius R of the hole is approximately 0.1 mm, the N.A. is 0.30, DOF is approximately 25 μm and D_o is approximately 7 mm. thus:

- Eq 5.2. gives the relationship between DOF and the width of the strip in the image.
- There is no resolution reduction caused by the size of the hole. If only the top part of the hole is investigated (the depth is less than 0.318 mm).

- The change of horizontal magnification inside the DOF can be ignored because d/D_{on} is less then 0.01 in the system.

5.1.2 Reconstructing the shadow image

The shadow image is reconstructed from a set of in-focus-strips. The strips contain different parts of the surface located inside the DOF (approximately 25 μm). These strips are added sequentially to form a contiguous surface shadow image. In order to make a smooth image, some overlap is needed. The cross-correlation operation is used to define where two neighbouring strips should be connected together. To simplify the process, the strips are straightened out. The whole process of reconstructing the shadow image is described in the following sections.

5.1.2.1 Overlapping

The internal surface is sampled in steps of 10 - 20 μm (DOF is approximately 25 μm). There is therefore overlap between two neighbouring strips. The smaller sample step is found to performed well.

5.1.2.2 Centre curves

The centre curves of every in-focus-strip are located by random edge detection. They give the location of the strips inside the image. The average arc of the curves is then calculated. It is further used in the next step.

5.1.2.3 Strip straightening operation

The arc of the internal surface is not important for the surface roughness measurement and may complicate the calculations, the strips are therefore straightened. The straightness is based on the average arc found in the previous step. After this processing the strip looks like that shown in Figure 5-3, where the white curve is the centre of the in-focus-strip.

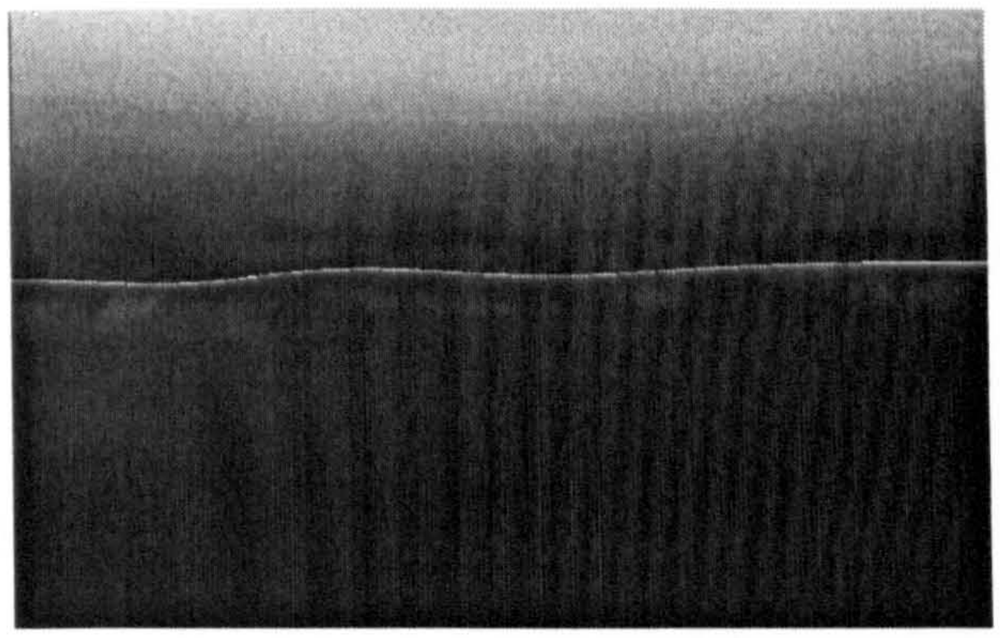

Figure 5-3 A strip after straightening

5.1.2.4 Connecting

The cross correlation operation is employed to connect the sequent in-focus-strips together. Figure 5-4 illustrates the method of connecting, where the light shadowed areas are the two strips. If all the strips are named as the topmost, the second, ... the bottom most, the connecting can start from either the top or the bottom side. In the following description, the connection starts with the two top strips.

The next step is data collection. A set of grey levels $f_i(x)$ is sampled from the topmost strip along a curve which is 5 μm offset from the centre. The curve is on

the side close to the second strip. Because of the overlap, the shadow pattern details around and below this curve must also appear in the next strip. Therefore the part of the image which is below this curve ($f_1(x)$) is truncated (the hatched area in Figure 5-4(a)).

In the second image, a 2-D grey level data $f_2(x,y)$ (The heaving shadowed area in Figure 5-4 (b)) is sampled within the strip on the side close to the topmost strip. The variable x is measured along the strip. The variable y is measured across the strip. A 2D cross correlation function $C(\tau,y)$ of f_1 and f_2 is then calculated:

$$C(\tau, y) = \frac{\int_{\Sigma} f_1(x-\tau) f_2(x, y) dx}{\sqrt{\int_{\Sigma} f_1^2(x-\tau) \int_{\Sigma} f_2^2(x, y)}} \qquad 5.8$$

where Σ is the integral region. The region is 9/10 of the image size along the strip. A region of one tenth image size is left for the variable τ in case the two strips need a horizontal shifting. An example of $C(\tau,y)$ is shown in Figure 5-5. The location (τ_o, y_o) of the maximum value of $C(\tau,y)$ indicates where $f_1(x)$ can be found in the second strip, that is $f_2(x-\tau_o,y_o)$. Both $f_1(x)$ and $f_2(x-\tau_o,y_o)$ are plotted in Figure 5-6. The part of the second image which is above $f_2(x-\tau_o,y_o)$ can be found in the remaining part of the topmost image and is therefore truncated (the hatched part in Figure 5-4 (b)).

The two images are then connected into a new contiguous wider topmost strip along their truncation edges. The horizontal shifting between the two images is

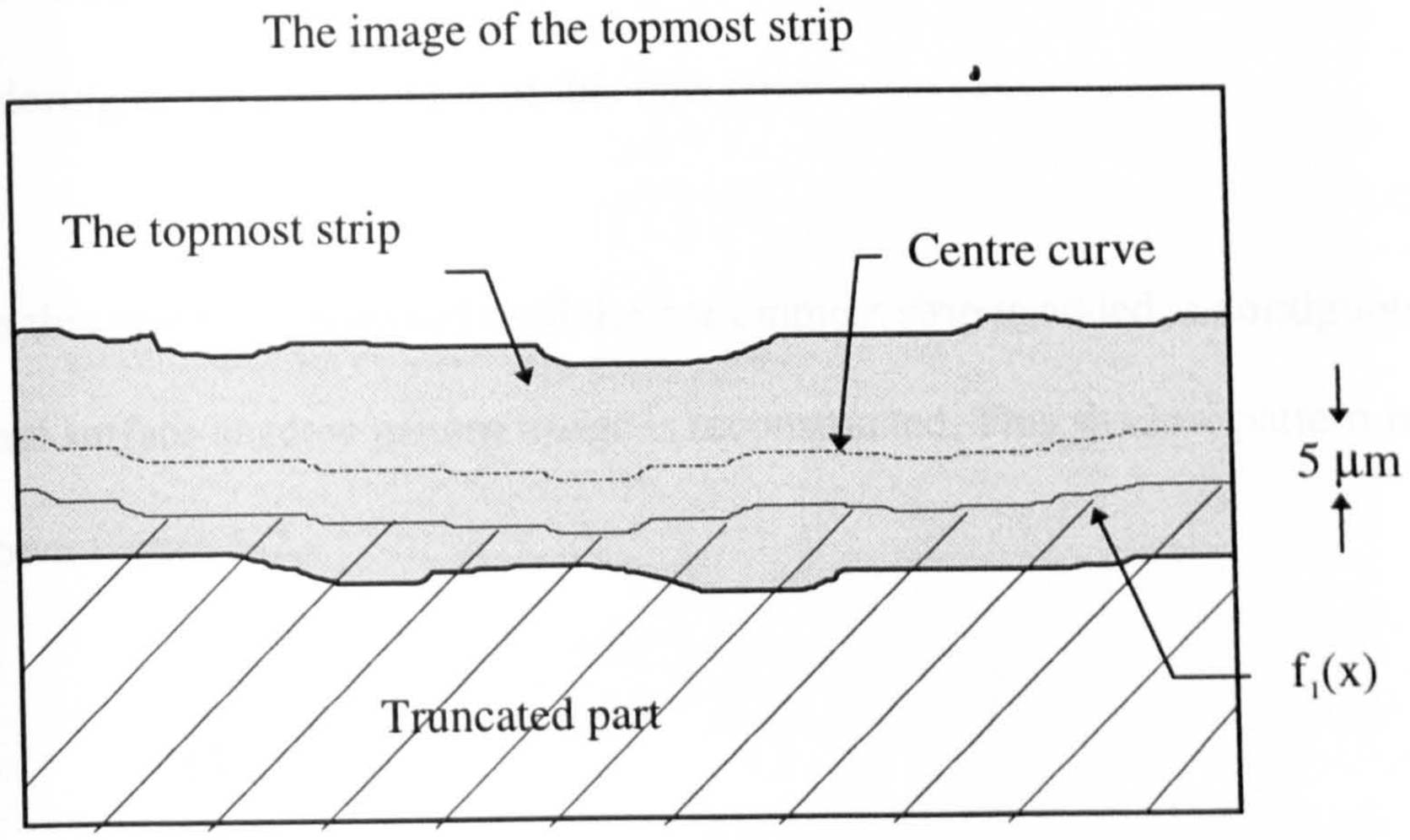

(a)

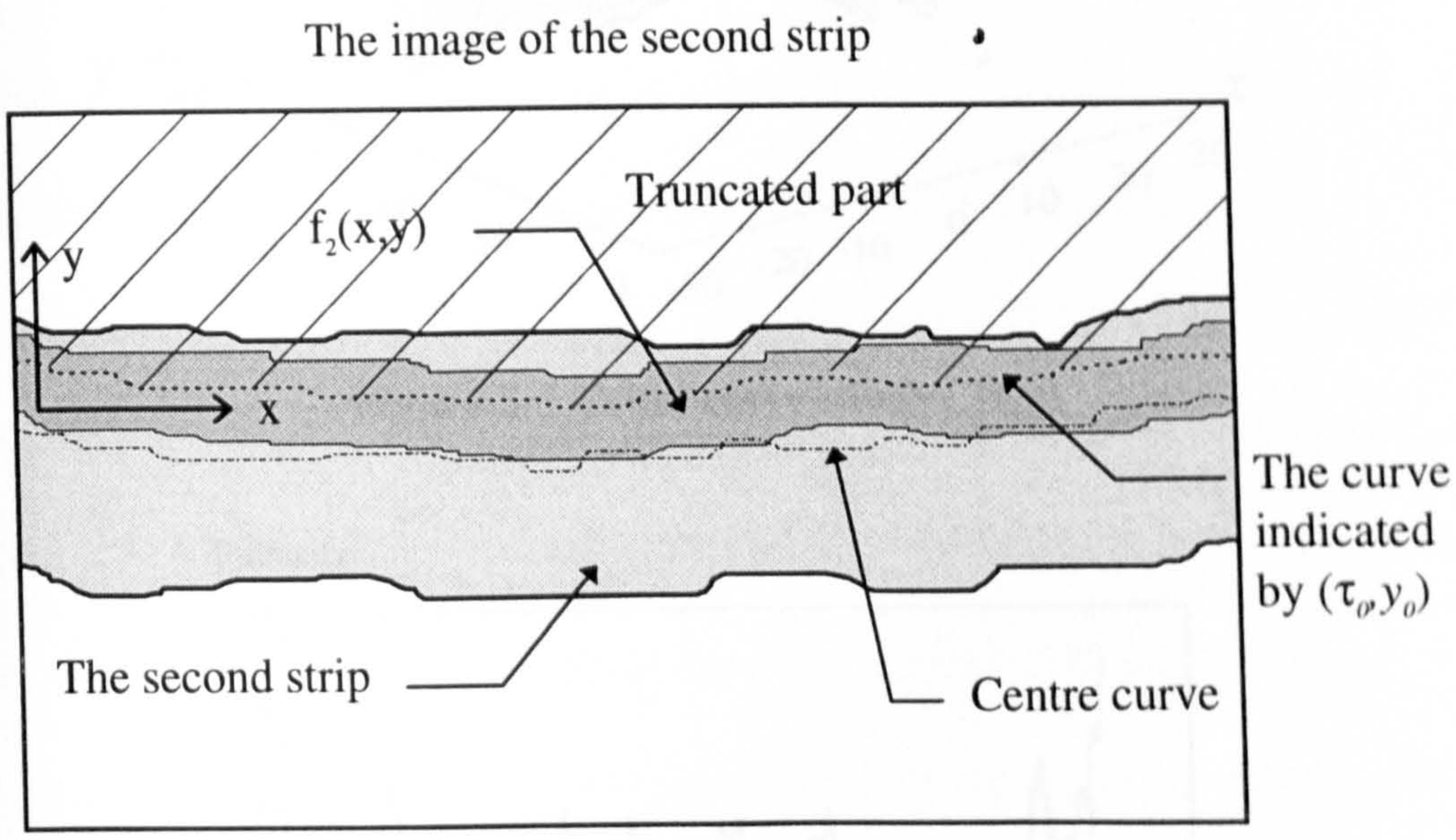

(b)

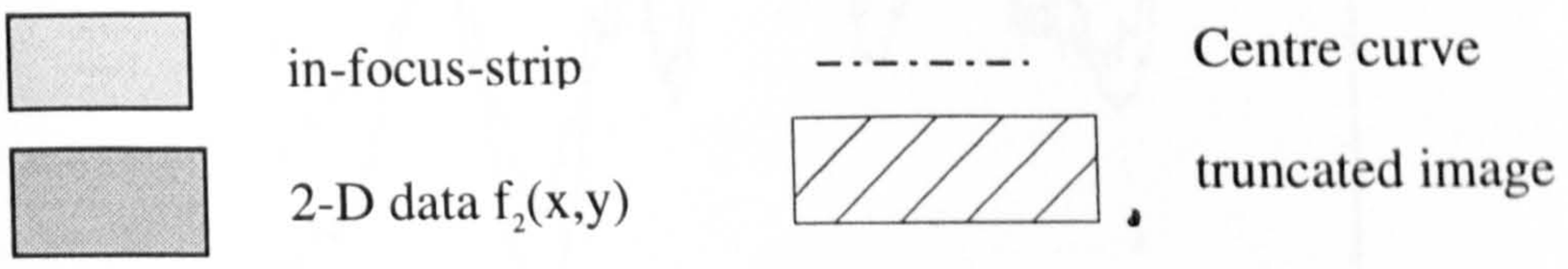

Figure 5-4 Illustration of connecting process

indicated by τ_0. Within the new wider strip, the centre curve of the second strip is considering as the centre curve of this new strip.

When this process is repeated until the bottommost strip is added, a contiguous internal surface shadow pattern image is reconstructed. This shadow pattern image is shown Figure 5-7.

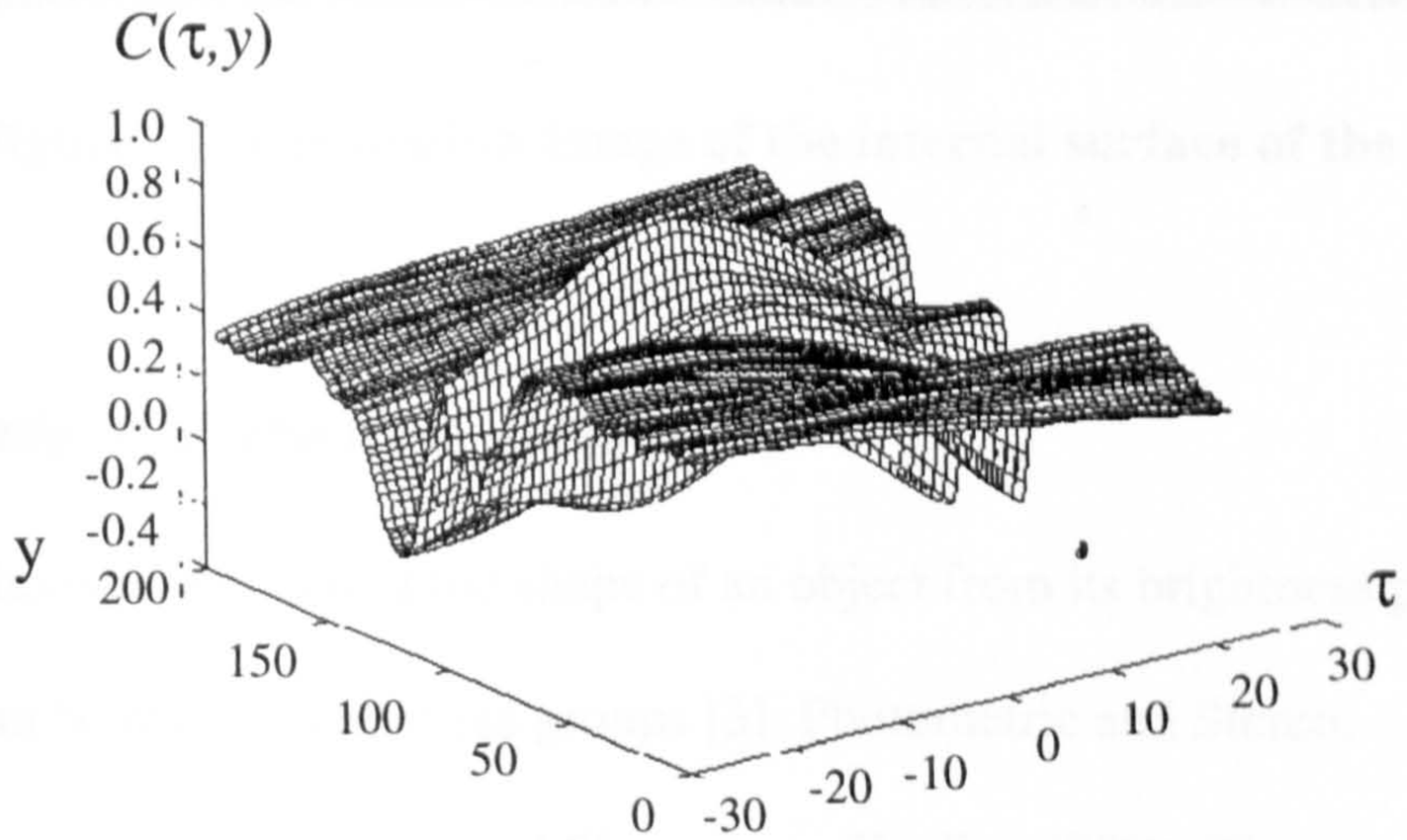

Figure 5-5 Cross correlation C(τ,y)

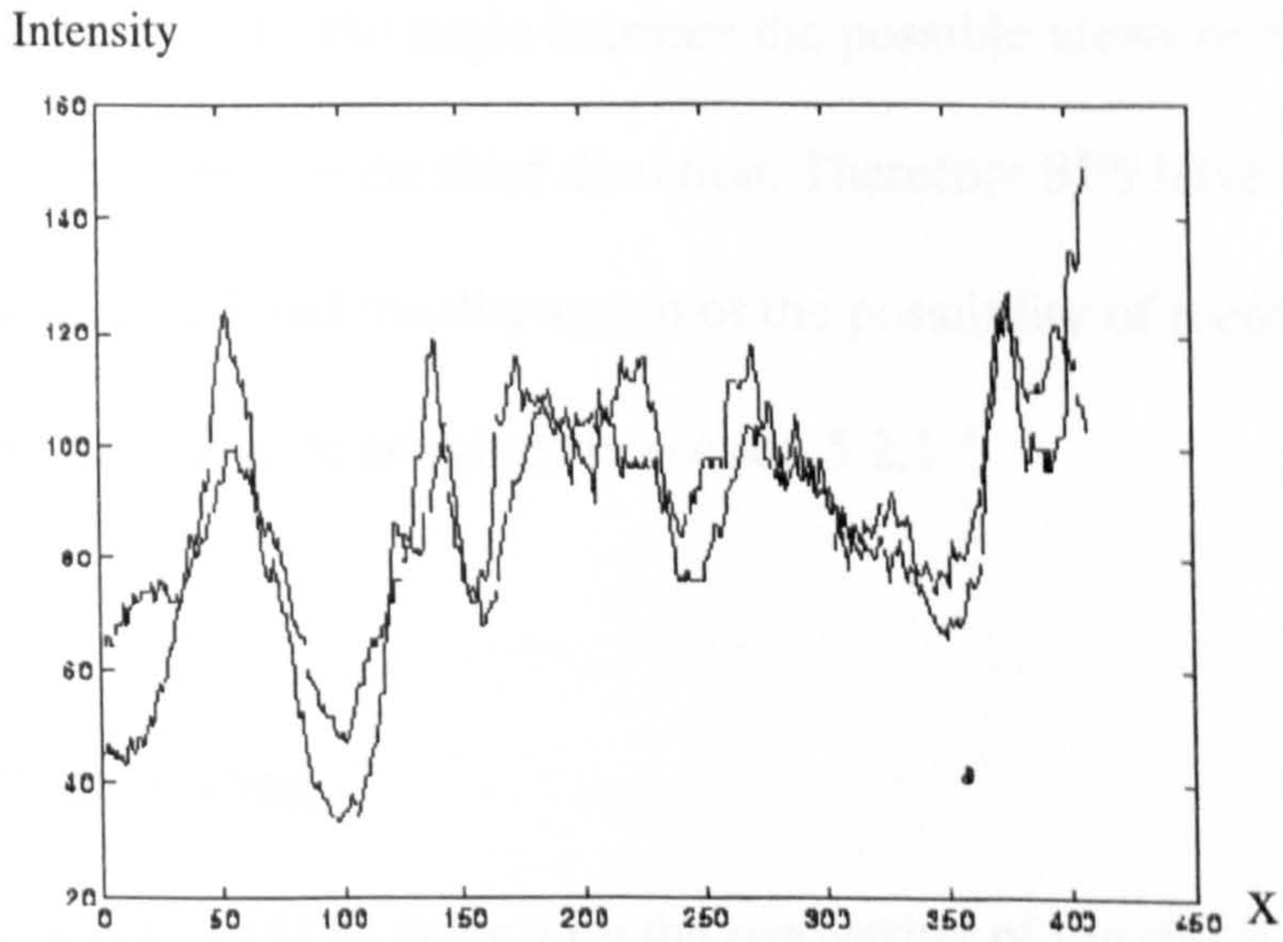

Figure 5-6 Comparison of $f_1(x)$ and $f_2(x-\tau_0,y_0)$.

Figure 5-7 The shadow image of the internal surface of the hole

5.2 Study of shape from shading

The methods of recovering the shape of an object from its brightness pattern image can be divided into three groups [3]: Photometric and Stereo, Photogrammetry and Stereo, and Shape from Shading (SFS). The stereo methods need either two illumination sources or two viewing directions. However, because of the limitation of the hole, the angle between the possible views or light sources is not wide enough to resolve the third direction. Therefore SFS have been studied. A review of SFS and the discussion of the possibility of recovering the internal shape of a small hole are given in section 5.2.1.

5.2.1 Shape from shading

The shape from shading (SFS) deals with the recovering of the shape of an object from its 2-D brightness image. In the following some assumptions have to be made:

- The light source and the observer are far from the object,
- and the albedo ρ (intrinsic reflectivity of the surface) is uniform.

Mathematically SFS studies show how to find $z(x,y)$ from the image irradiance equation[3]:

$$I(x,y)= \rho\, R(n_s, n_o, n, z, p, q) \qquad \text{Eq 5.9}$$

Where

- $I(x,y)$ -------- the brightness of the image,
- $z(x,y)$ -------- the height of the surface,
- $\mathbf{n}_s$ -------- the directions of light source,
- $\mathbf{n}_v$ -------- the direction of viewer,
- $\mathbf{n}$ -------- the surface normal
- p -------- $\partial z/\partial x$
- q -------- $\partial z/\partial y$.
- R -------- the reflectance map.

Different reflecting models have different kinds of *R*, and need different recovery methods.

5.2.1.1 Reflecting models

Different reflecting models have different kinds of *R*. They are used to reduce the complication of solving the equation 5.9 and representing special real surfaces, so they have special physical meaning. The models are:

- Linear Reflectance Map:

This model simply assumes that R has the following form:

$$R(p, q) = f(ap+bq), \qquad 5.10$$

where a and b are constants.

- Rotationally Symmetric Reflectance Map:

The rotationally reflectance map can be written as:

$$R(p, q) = f(p^2+q^2), \qquad 5.11$$

This happens when the light source is distributed in a rotationally symmetric pattern around the viewer.

- Lambertian Reflectance Map:

The Lambertian surface is a widely used model which assumes that the surface is equally bright from all viewing directions. The $R(p, q)$ of the Lambertian surface is written as

$$R(p,q) = \frac{1+pp_s+qq_s}{\sqrt{1+p^2+q^2}\ \sqrt{1+p_s^2+q_s^2}} \qquad 5.12$$

or simply

$$R(p, q) = \mathbf{n}_s \bullet \mathbf{n} \qquad 5.13$$

where p_s and q_s are the components of $\mathbf{n}_s$:

$$n_s = \frac{(p_s, q_s, -1)}{\sqrt{(p_s^2 + q_s^2 + 1)}} \qquad 5.14$$

- Specular surface model:

  In the contrast to the Lambertian surface, Specular surface assumes all the reflection occurs in a very narrow range around the direction of specular reflection. The reflectance map can be written as:

$$R(p, q) = \delta(|(n_s - n_v) \bullet n| + |(n_s \times n_v) \bullet n|), \qquad 5.15$$

- Healey-Binford model:

  Between the Lambertian and specular surfaces, there is a model proposed by Healey-Binford [4]:

$$R(p,q) = e^{-(\frac{\alpha}{m})^2} \qquad 5.16$$

  Where α is the angle between the surface normal **n** and the bisector of the viewing direction $\mathbf{n}_v$ and light source direction $\mathbf{n}_s$, m indicates the surface roughness. The smaller the value of m is, the more rough the surface is. By using **h** as the bisector direction:

$$h = (n_v + n_s)/|n_v||n_s| \qquad 5.17$$

then

$$\alpha = cos^{-1}(\mathbf{n} \bullet \mathbf{h}) \qquad 5.18$$

5.2.1.2 The recovery of the shape from shading

The objective of SFS is to recover the shape of a surface from its single grey level image. In other words, to find $z(x,y)$ from Eq 5.8. This equation is an ill-defined problem because there are more than one unknown and only one equation[3].

However, attracted by the capability of the human visual system to extract shape from a single shading image, a lot of research has been done on this subject. B. K. P. Horn wrote probably the first book about this area[3]. His another book is a collection of the researches[5]. A review of related mathematical methods in SFS is given by N. Hurt[6]. The methods include dealing with the uniqueness[9] in SFS; differential geometry of SFS; variations and other algorithms. The solution of the irradiation equation Eq 5.9 is treated as a first order Hamilton-Jacobi equation [10] [11]. Local shading analysis which involves second order differentials of the image grey level has been discussed in SFS [12] - [14]. Their authors were likely to encountered the noise when they calculate second order differentials. Instead of recovering the shape exactly, a variational calculation approach has been used to find a best estimation of the shape [15] - [17]. It has a better ability to avoid integration and image brightness errors than that of exactly recovering methods. Besides the above theoretical studies, many algorithms have been developed for more accuracy, speed and robustness recovering techniques. The linear approximation approach is used for its simplicity[18]. The average p and q error is 0.45 after 40 iterations. Another method assumes the surface is constructed by triangular elements [19], 10% error of depth is achieved. The situation where both camera and light source are near the surface is also studied [20]. A heuristic approach is suggested even having less mathematical background [21]. A robust algorithm can give a good estimation of the shape even when some noise is added in the image [22]. The mean absolute errors of brightness (difference between the intensities of original and the results images in grey level unit) and of depth (difference between the original and result object) vary from 3.5

to 19.06 and 0.13 to 1.75 respectively according to the noise added. An approach which can deal with a complex wrinkled surface has been proposed[23]. In this approach both height and gradient are represented.

5.2.2 The problem of measuring the surface of a small hole

There are two reasons why SFS is not suitable for analysis the surface of a small hole.

1) The blockage occurs in both illumination and observation of the internal surface, so that some area is not illuminated nor viewed. The image which has been reconstructed is a shadow image instead of a shading image. This discontinue shading information will distort the shape recovery, because SFS reconstructs the shape from the relationship between neighbouring pixels.

2) As the internal surface of the hole is generally a random surface, statistical parameters might be the best method of characterising it.

5.2.3 Lambertian and Healey-Binford model

Nearly all the SFS studies use Lambertian reflectance maps. Healey-Binford model has been treated separately[18]. It is proved in this section that both the Lambertian and Healey-Binford model can be recovered by the same method.

The irradiance equation of Lambertian model is $I(x,y)= \rho\ \mathbf{n}\bullet\mathbf{n}_s$ The irradiance equation of Healey-Binford model is $I(x,y)= \rho e^{-(\frac{\alpha}{m})^2}$. However, Healey-Binford model can be also written in the following form:

$$cos(m\sqrt{}\ (log\rho - logI(x,y))\ ) = \mathbf{n} \bullet \mathbf{h} \qquad \textbf{Eq 5.19 .}$$

because the left side of Eq 5.19 only varies with (x,y). If $I_{h\text{-}b}(x,y)$ is used to represent $\rho cos(m\sqrt{}\ (log\rho - logI(x,y)))$, Eq 5.19 can be written as:

$$I_{h\text{-}b}(x,y) = \rho\ \mathbf{n} \bullet \mathbf{h}, \qquad 5.20$$

the same as Lambertian irradiance equation. Therefore if $\rho cos(m\sqrt{}\ (log\rho - logI(x,y)))$ is used instead of $I(x,y)$ and **h** is used instead of $\mathbf{n}_s$, all the methods used in Lambertian model analysis can be used in the Healey-Binford model analysis.

5.3 *Statistical analysis*

The shadow image reflects the shape of the internal surface. Without blockage, the Shape From Shading (SFS) is the technique used to recover the shape of the object. With the blockages, the intensity of the shadow image is not always related to the slope of the surface and the situation is more complicated. On the other hand, it is better to use statistical parameters for a random surface finish analysis. These statistical parameters can be calculated from the shadow image as explained in the following sections.

5.3.1 Shadow model

To simplify the analysis, the following assumptions are made for shadow model:

- There are shadows at the side of the peaks or valleys towards the observer. It guarantees the existence of shadows.

- *The peaks or valleys are far enough apart so that the size of the shadow can be measured without blockage. This means that the shadow size measured is only related to the height or depth of the peaks or valleys.*
- *The distribution of the height of the peaks and the depth of the valleys are the same. In fact, from a shadow image, it cannot be recognised that if the shadow is caused by peaks or valleys. If the peaks and valleys are evenly distributing, all the shadows can be considered to be caused by peaks or valleys without influencing the analysis. (In the following analysis only peaks are considered)*

Figure 5-8 shows the relationship between height of peak, shadow size and other factors. Where l is the shadow size on the surface; z is the height of the peak; l_v is the shadow size measured from the image. The relationship is given by:

$$l_v = z(1+tg(\theta_2)/tg(\theta_1)) \qquad 5.21$$

The probability of $l_v > L$ can be measured from the shadow image. It is represented as $P_l(l_v < L)$. The distribution of $z < Z$, which is defined as $P_z(z < Z)$, can be therefore found from the following equation[24]:

$$P_z(z<Z) = P_l(l_v<L) = P_l(l_v < Z(1+tg(\theta_2)/tg(\theta_1))) \quad \text{Eq 5.}$$

Thus:

$$p_z(z) = \frac{dP_z(z)}{dz} = \frac{dP_l(l)}{dl_v}\frac{dl_v}{dz} = p_l(l_v(z))(1+tg(\theta_2)/tg(\theta_1)) \qquad 5.23$$

where $p_z(z)$ is the probability density of the height distribution of the surface, $p_l(l_v)$ is the probability density of the shadow size of the shadow image.

5.3.2 The amplitude parameters of the surface

The three common useful amplitude parameters of a surface are R_q, R_a and R_t.

They are defined as:

$$R_q = \int p_z(z)(z-\bar{z})^2 dz$$
$$R_a = \int p_z(z)|z-\bar{z}|dz \qquad 5.24$$

Where $\bar{z}$ is the mean height of the surface.

R_t is defined as the maximum peak to valley height of the profile in the area.

Because of the third assumption of shadow model, $R_t/2$ equals to $\bar{z}$.

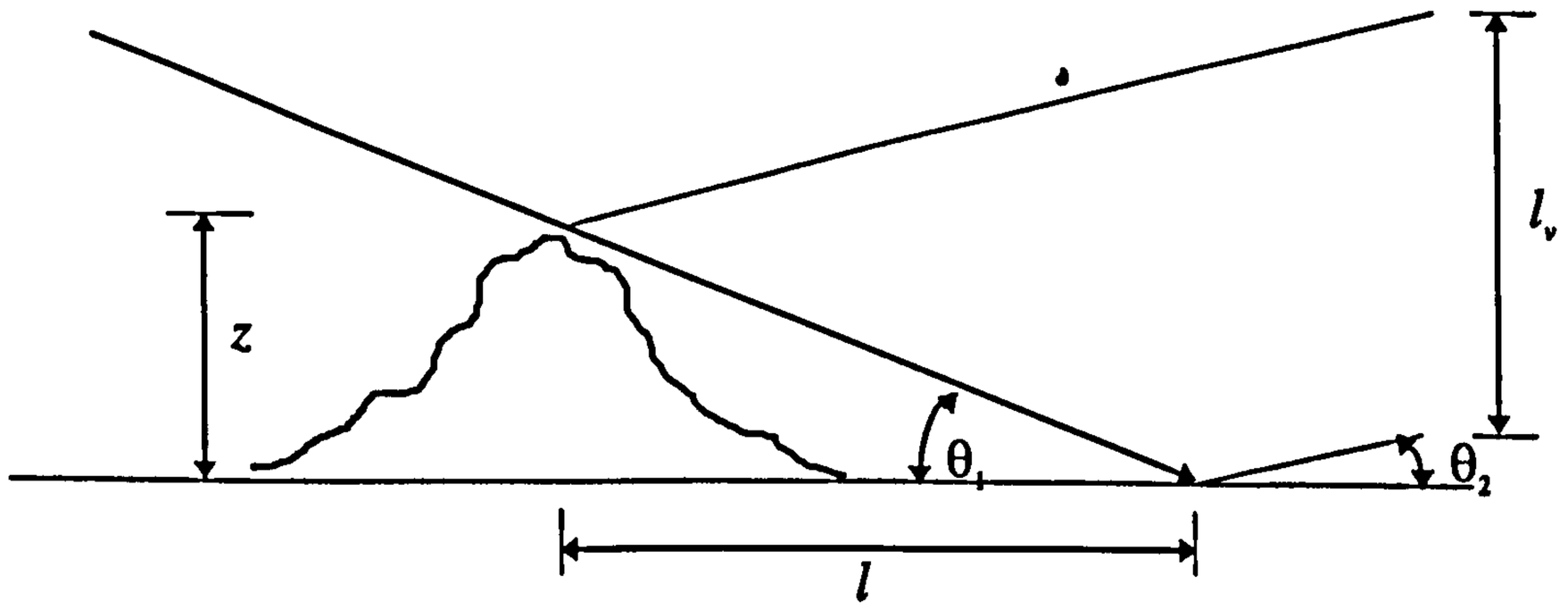

Figure 5-8 Shadow model

5.4 *Verification of method*

The surface roughness of a known flat surface made by spark erosion has been measured by the optical method described in section 5.3.1. The result has been tested in the following two ways:

1) Goodness fit test;

2) Comparing the result with stylus measurements.

Figure 5-9 is the shadow image of the known flat surface. It is reconstructed by the method described in section 5.1. Figure 5-10 is the surface height percentage polygon which is calculated from the shadow size percentage polygon according to Eq 5.22. The shadow size percentage polygon is measured form the shadow image of the surface.

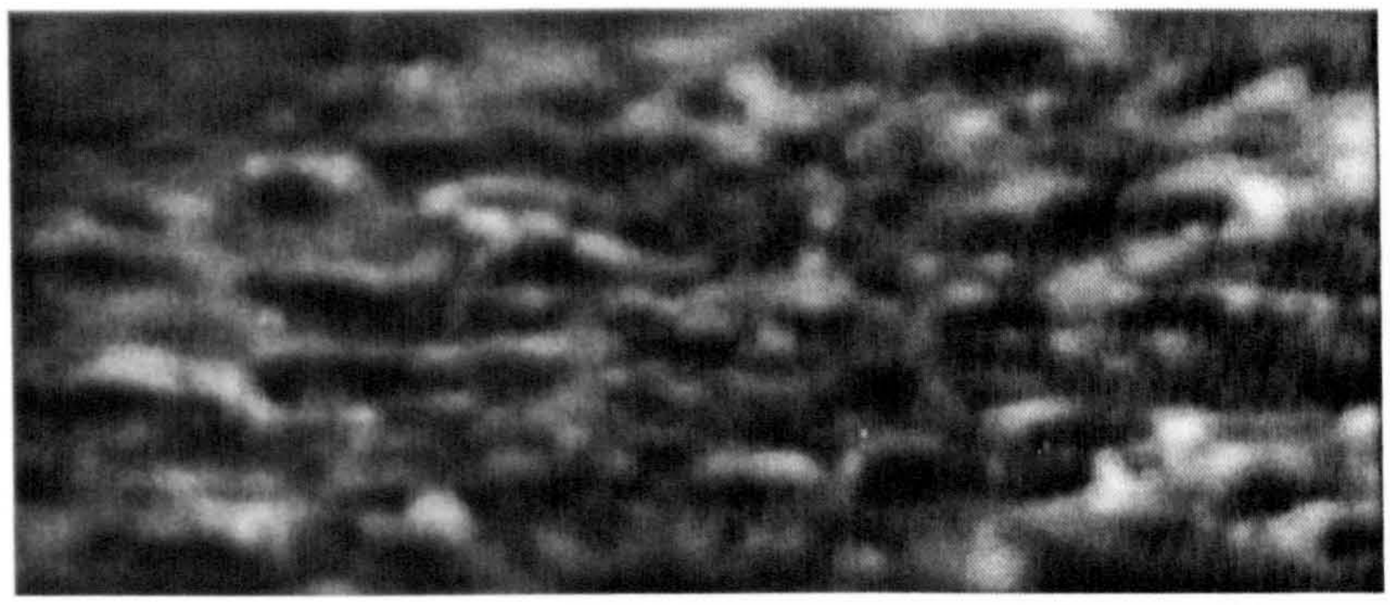

Figure 5-9 Shadow image of the known flat surface

5.4.1 The χ^2 Test of Goodness-of-fit [24]

The height percentage polygons measured from the shadow image is further tested if it is governed by a Gaussian distribution or not. The χ^2 Test of Goodness-of-fit is used. A Gaussian distribution, whose mean and standard deviation are the same as the data measured from the shadow image, is chosen. In this test, the total region of the height is divided into 5 subintervals as shown in Figure 5-11. The

expected probability p_i^0 which is calculated from the Gaussian distribution and the frequency p_i which is measured from shadow image are listed in the Table 5-1.

Table 5-1 The data for χ^2

	P_i^0	p_i
1	0.061	0.082
2	0.24	0.27
3	0.38	0.31
4	0.25	0.27
5	0.066	0.082

A value can be calculated from Table 5-1 according to the following equation:

$$\chi^2 = \sum_{i=1}^{5} \frac{(np_i - np_i^0)^2}{np_i^0}, \qquad 5.25$$

where n ,the total number of samples, emerged as 196.

The result is that $\chi^2 = 6.07 < \chi^2_{0.05,4} = 9.448$, where $\chi^2_{0.05,4}$ is the value of a 4 degree freedom χ^2 distribution with the critical region equal to 0.05. Therefore it can be said that, with a 0.05 significance level, the height distribution of the surface is a Gaussian distribution.

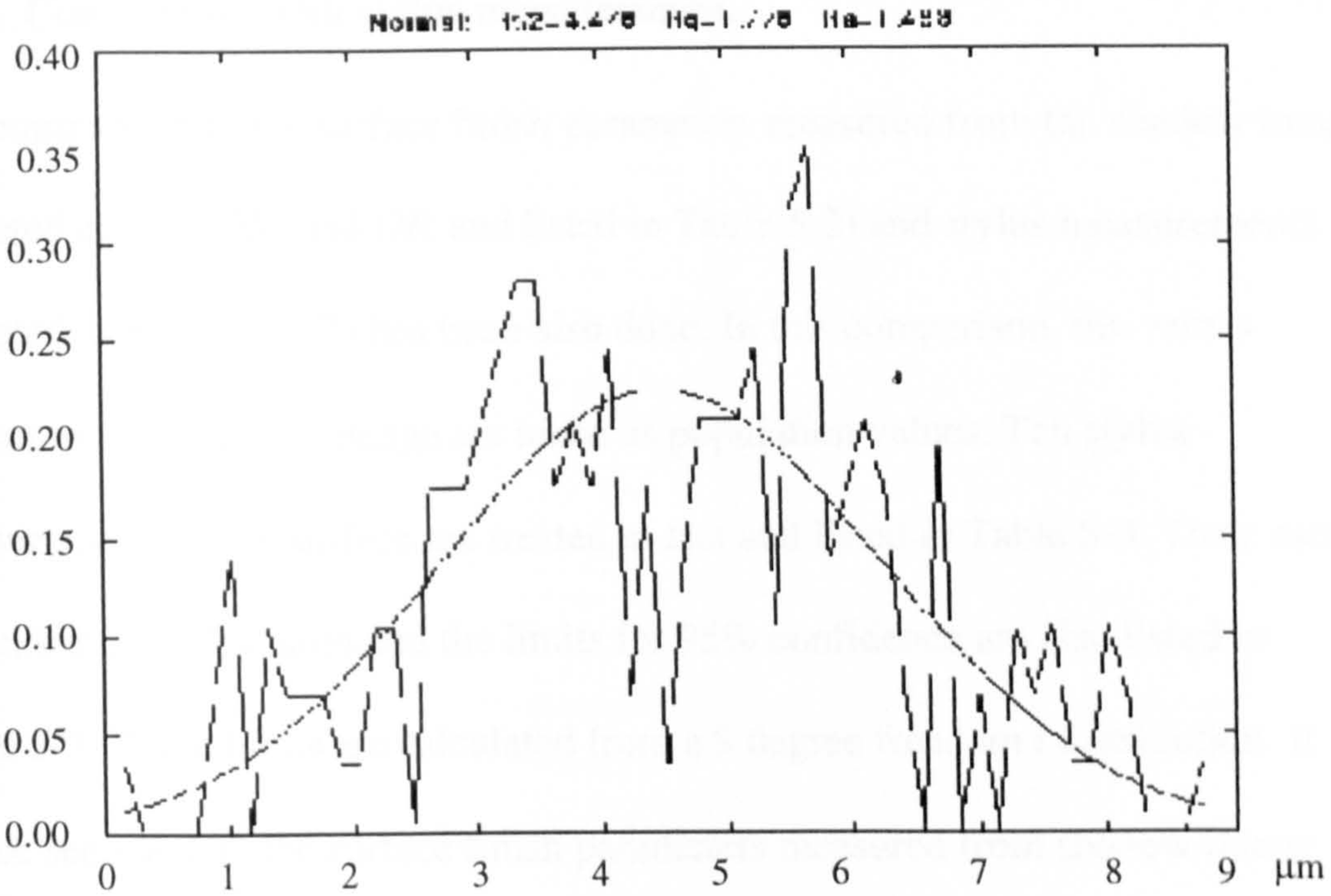

Figure 5-10 The height and the related normal distribution of the surface

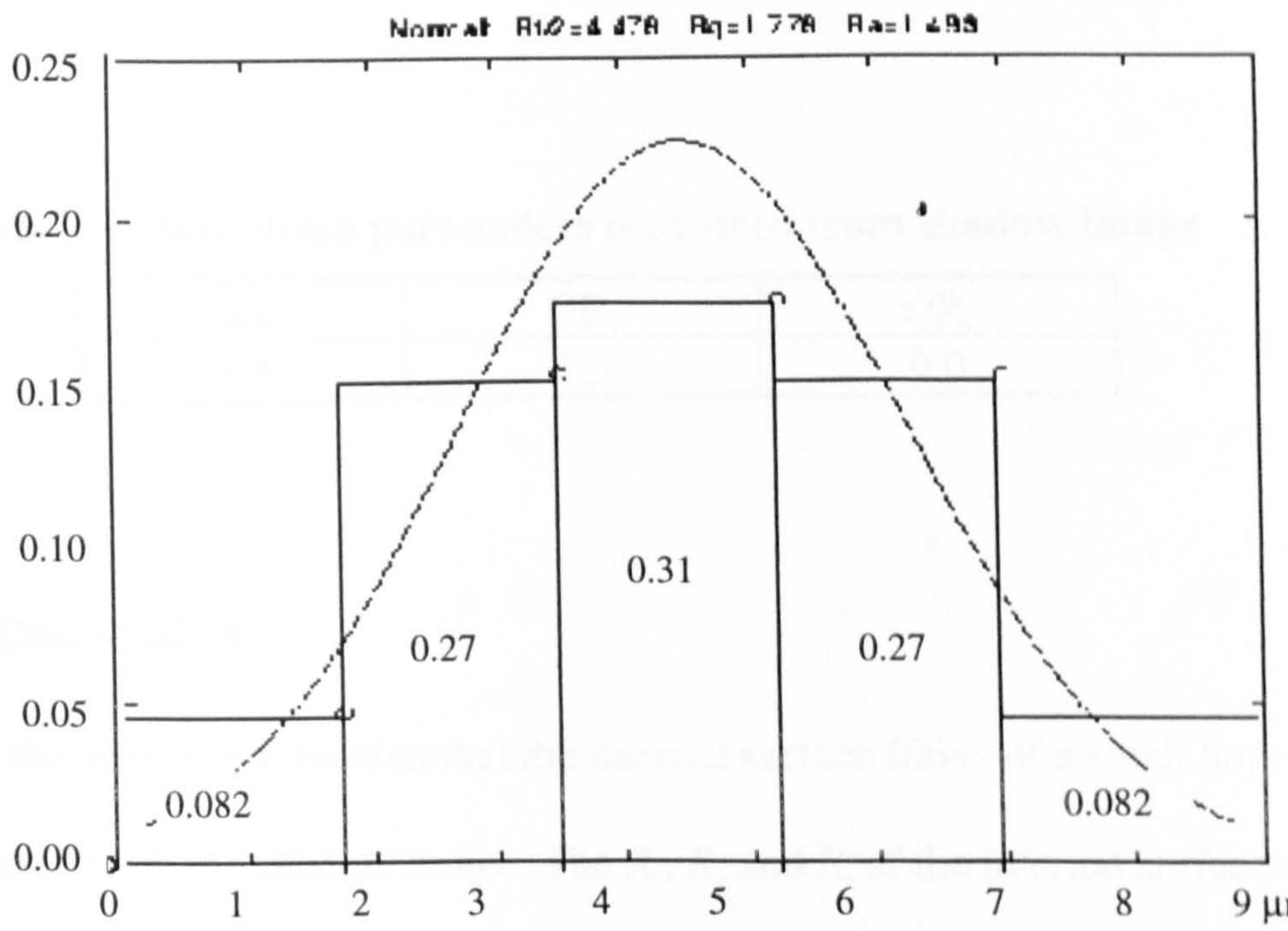

Figure 5-11 Histogram of height distribution measured from the shadow image

5.4.2 Comparison with stylus measurement.

The comparison of the surface finish parameters measured from the shadow image (denoted as OR_q, OR_a and OR_t and listed in Table 5-2) and stylus measurements (denoted as R_q, R_a and R_t) has been also done. In this comparison, the values measured from shadow image are taken as population values. Ten stylus measurements of the surface are treated as test and listed in Table 5-3. Their mean value, standard deviation and the limits for 95% confidence are also listed in Table 5-3. These limits are calculated from a 9 degree freedom *t* distribution. It can be seen that all the surface finish parameters measured from shadow image fall inside the interval. It therefore can be said that for a 95% confidence, all the measurements come from same surface sample. That is, that the optical method is acceptable.

Table 5-2 Surface finish parameters measured from shadow image

OR_q	OR_a	OR_t
1.8	1.5	9.0

5.5 Conclusion

From the tests, it can be seen that the internal surface finish of a small hole can be measured from the shadow image. The R_q, R_a and R_t of the internal surface of the hole are 1.8, 1.4 and 9.9×10^{-3} mm respectively. The χ^2 Test of Goodness-of-fit is also taken in the same way. $\chi^2 = 8.98 < \chi^2_{0.05,4} = 9.448$. Therefore the internal surface can also be consider as a Gaussian distribution for a 95% confidence.

Table 5-3 10 stylus measurements, their mean and standard deviation (SDT)

	R_a	R_q	R_t 10^{-3} mm
1	1.81	1.45	8.3
2	2.11	1.67	11.1
3	1.53	1.24	7.9
4	1.79	1.46	8.1
5	2.04	1.67	10.5
6	1.83	1.52	9.0
7	1.88	1.53	9.7
8	1.86	1.52	9.1
9	1.77	1.47	8.3
10	2.05	1.68	9.6
Mean	1.85	1.50	9.1
STD	0.167	0.128	11.1
Limits for 95% confidence	1.86 ±0.13	1.50 ±0.097	9.1 ±0.84

References

[1] D. Birchon *Optical Microscope Technique* George Newnes Ltd, London 1961

[2] L. C. Martin *Technical Optics* Vol.2 2nd Edition Sir Isaac Pitman & Sons Ltd. London 1966

[3] B. K. P. Horn *Robot Vision* The MIT Press 1987 London

[4] G. Healey and T. O. Binford "Local shape from specularity" *Comput Vision, Graph Image Process.* **42** 62-86 (1988)

[5] B. K. P. Horn and M. J. Brooks (eds.) *Shape from shading,* MIT Press , Cambridge, 1989

[6] N. Hurt "Mathematical Methods in Shape-From-Shading: A review of recent results" *Acta Applicandae Mathematicae* **23** 163-188, 1991.

[7] B. K. P. Horn, R. Szeliski, and A. L. Yuille, *MIT AI Lab* Impossible shading images. 1989.

[8] J. Oliensis "Existence and uniqueness in shape from shading" *Coins TR 89-109,* Univ., Mass. 1989.

[9] B. V. H. Saxberg "Existence and Uniqueness for Shape from Shading Around Critical Points: Theory and an Algorithm" *The International Journal of Robotics Research.* **11**(3) 202- 224 (1992)

[10] A. Tourin "A comparison theorem for a piecewise Lipschitz continuous Hamiltonian and application to Shape-from-Shading problems" *Numerische Mathematik* **62** 75-85 (1992)

[11] P. L. Lions, E. Rouy, and A. Tourin "Shape-from Shading, viscosity solutions and edges" *Numerische Mathematik* **64** 323-353 (1993)

[12] A. P. Pentland "Local Shading Analysis" *IEEE Transactions on PAMI* **6**(2) 170-187 (1984)

[13] F. P. Ferrie and M. D. Levine "Where and why local shading analysis works"

IEEE Transactions on PAMI **11**(2) 198-206 (1989)

[14] M. Ferraro "Local geometry of surfaces from shading analysis" *J. Optical Society of America A* **11**(5) 1575-1579 (1994)

[15] K. Ikeuchi and B. K. P. Horn "Numerical shape from shading and occluding boundaries" *Artif. Intell.* **17** 141-185 (1989)

[16] G. Smith "The recovery of surface orientation from image irradiance" *Proceeding DARPA Image Understanding Workshop,* Palo Alto, September 1982

[17] B. K. P. Horn and M. Brooks "The Variational Approach to Shape from shading" *Computer Vision, Graphics and Image Processing* **33** 174-208 (1986)

[18] P-S Tsai and M. Shah "Shape from shading using linear approximation" *Image and Vision Computing* **12**(8) 487-498 (1994)

[19] K. M. Lee and C-C. J Kou "Shape from shading with a linear triangular element surface model" *IEEE Transactions on PAMI* **15**(8) 815-822 (1993)

[20] H. U. Rashid and P Burger "Differential algorithm for the determination of shape from shading using a point light source approximation" *Image and Vision Computing* **10**(2) 119-127 (1992)

[21] O. E. Vega and Y. H. Yang "Shading logic: A Heuristic Approach to Recover Shape from Shading" *IEEE Transactions on PAMI* **15**(6) 592-597 (1993)

[22] A. G. Jones and C. J. Taylor "Robust shape from shading" *Image and Vision Computing* **12**(7) 411-421 (1994)

[23] B. K. P. Horn "Height and gradient from shading" *International J. Computer Vision* **5**(1) 37-75 (1990)

[24] Morris H. DeGroot *Probability and Statistics* Addison-Wesley 1989

6. Another study of internal measurement

To complete the internal measurement, the method described in this chapter is designed to measure the internal structure features within a component of a Cummins' lorry engine. Figure 6-1 shows the dimensions of the component. The diameters are 18.28 mm along *AB* and 15.00 mm along *GB*. The measurement of distances *AB*, *AC* and other dimensions are required. Even though special micrometer (chapter 2's [2]), and some kind of instrument like RTH Talyrond may be designed for this measurement, the optical non-contact method described in this chapter has its advantages:

1) The Talyrond and micrometer basically provided point-contact measurements. Because of the mechanical integrated, they do not provide some details such as the defects shown in Figure 6-6 and Figure 6-7. The optical method can give a view of that.
2) If the gaps, say *CD* and *EF*, are very small, the design and manufacture of a suitable probe for micrometer and Talyrond is difficult. The optical method does not touch the component. It is easy to measure small gaps.

The internal structure of such a component can be imaged by a specialised high resolution, long working distance and diffraction limited lens remotely. The image can be then stored digitally. The dimensions of the internal structure can be

therefore measured by detecting the edge locations in the digital images. This approach achieves a resolution better than ± 2.5 μm.

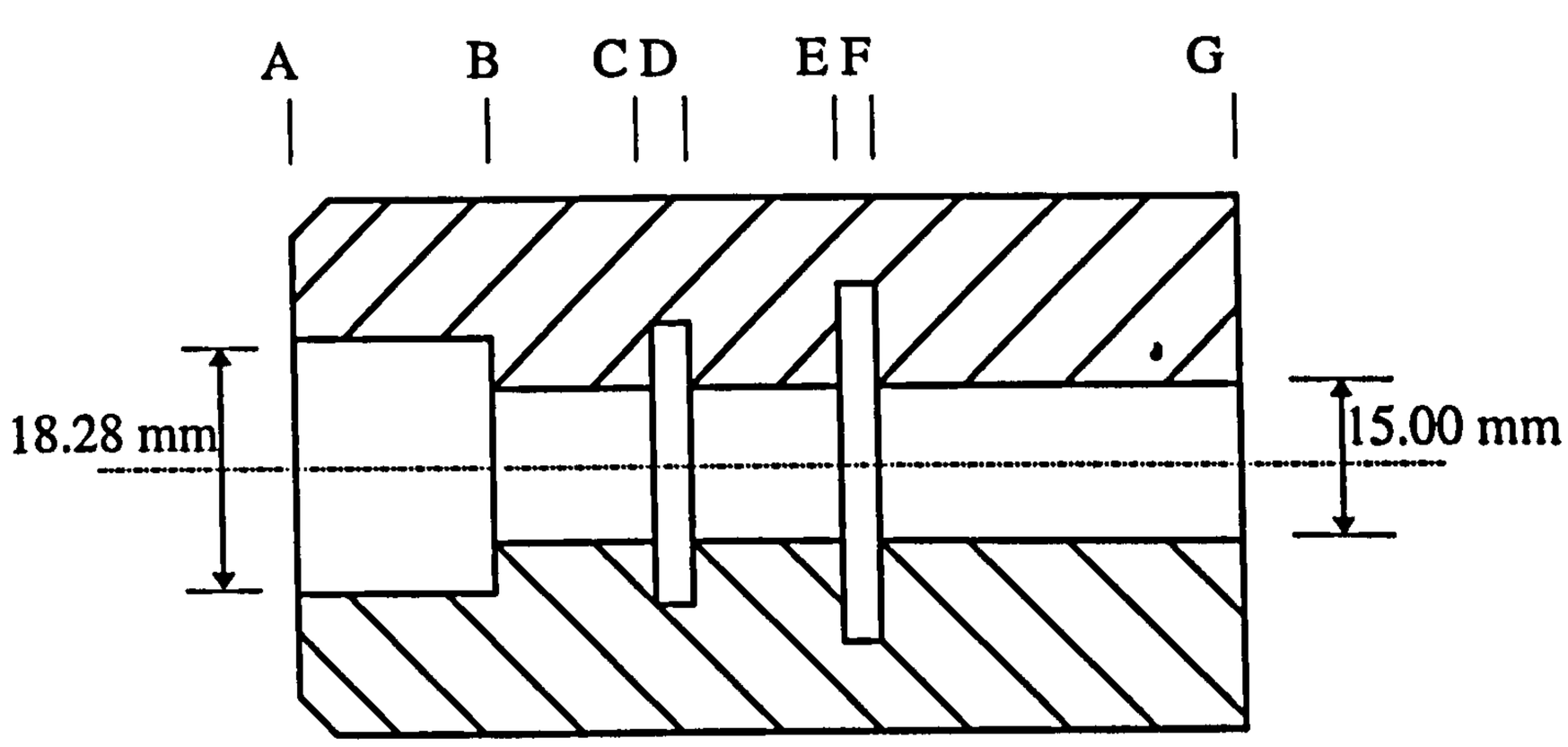

Figure 6-1 Dimension of the component

6.1 The method of measurement

This measurement is based on image edge detection and internal inspection by a high resolution, long working distance and diffraction limited lens. The image edge detection approaches have been reviewed in section 3.2.2. Figure 6-2 gives an example of measuring distance *AB*. Where E_b and E_a are the relative locations of edge $\mathcal{A}$ and $\mathcal{B}$ respectively. *D* is the distance between the two positions where these two images are taken.

The distance *AB* can be calculated from:

$$AB = D + E_b - E_a \qquad 6.1$$

Where E_b and E_a can be found from edge detection. D is the movement of the whole component and is recorded when the component is being moved. AC, AD and other dimensions can be measured in the same way.

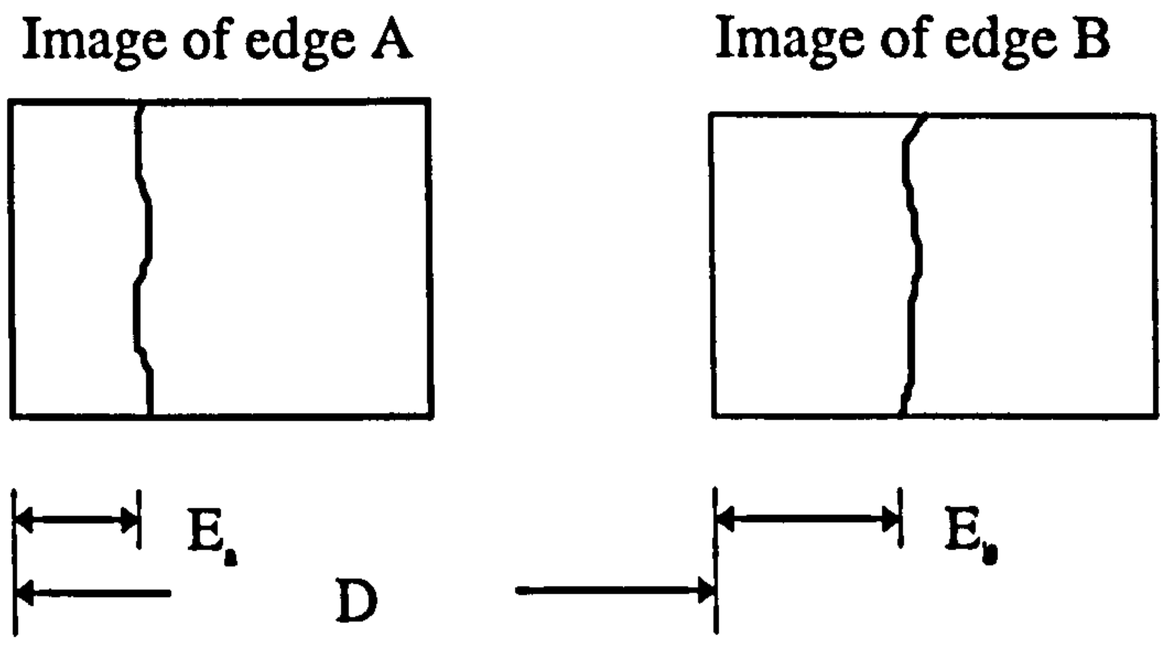

Figure 6-2 Measuring method

6.2 Measuring system

The measuring system is shown in Figure 6-3. The component is placed on a two-axis micrometer traverse. The movement of the traverse is measured by a displacement transducer with a resolution of 1 μm. A small 45^0 angled mirror is placed inside the component. K2[1] is a specialised high resolution long working distance and diffraction limited lens. The lens is placed outside of the component to view the interior surface orthogonally. In order to keep the lens focus at a known plane with a fixed magnification, all optical components(the lens, viewing mirror and the illumination system) were mounted as one system. The X movement of the component, which is along the axis of the component, is

[1] Parfocal Ltd. Imaging & Technology Ringwood Hants

measured by a displacement transducer[2]. The *Y* movement gives the viewer an opportunity to move the area of interest to the focal plane. The surface is illuminated by a tungsten light source delivered internally through 10 flexible light guides[3]. The light guides terminate around the 45^0.

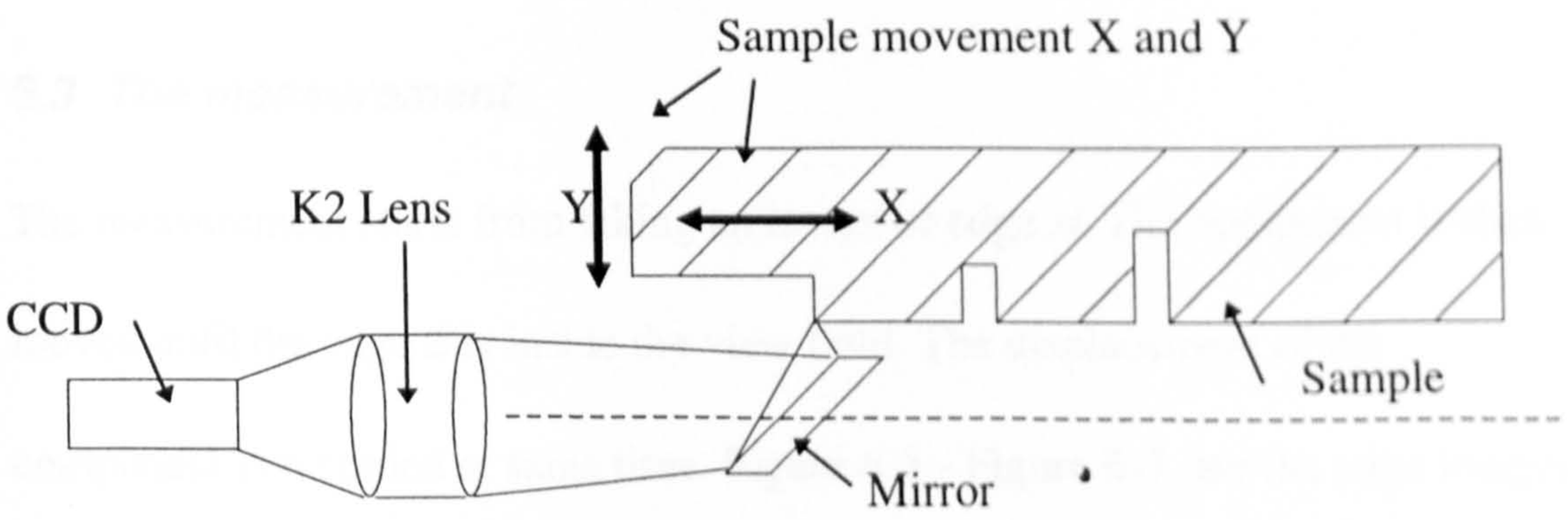

Figure 6-3 Measuring system

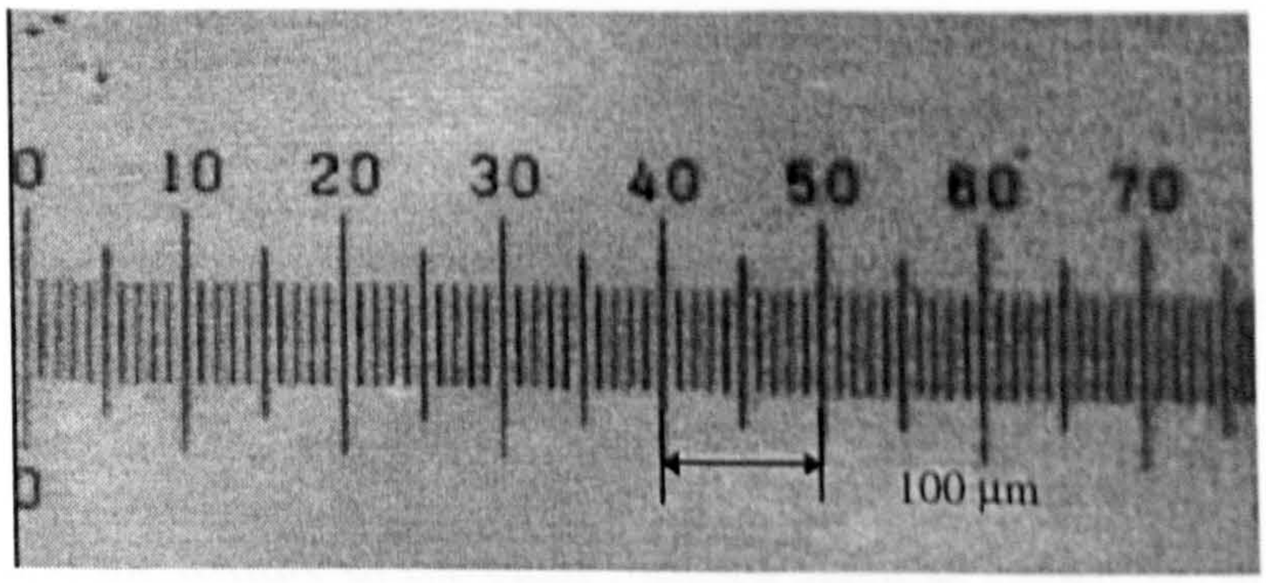

Figure 6-4 Calibration: 10 micron per division

[2] TESA Swiss
[3] Ultrafine Ltd. Brentford Middx UK

The system was calibrated by taking an image of a microscope graticule as shown in Figure 6-4. The pixel interval is 1.2 μm. The working distance of the lens is 60 mm. The effective F number of the lens is 4. The lens has a theoretical optical resolution of 4 μm. It is the limitation of the overall resolution of the system.

6.3 The measurement

The measurement starts from taking an image of edge $\mathcal{A}$. The component is then moved until the edge $\mathcal{B}$ is inside the view field. The displacement of the component is recorded at same time. Figure 6-5 - Figure 6-7, are the edge images of $\mathcal{A}$, $\mathcal{B}$ and $\mathcal{C}$ respectively. They are clear edge images. Figure 6-8 is a plot of the light intensity across edge $\mathcal{A}$. Figure 6-9 is a 2-D plot of edge $\mathcal{A}$.

A LoG edge detector is applied to edge $\mathcal{A}$, the outcomes are shown in

Figure 6-10 (a). The white curves in the figure are the edges. Their brightness relates to the strength of the edges. It is not surprising that the results included both edge $\mathcal{A}$ and the texture of the clear focused surface. However, in this particular measurement, the texture of clear focused surface is not of interest. The edge $\mathcal{A}$ must be separated. But there is no guarantee that edge $\mathcal{A}$ is the strongest edge. The texture edges cannot therefore be removed by scale setting. On the other hand, the edge $\mathcal{A}$ divides the image in to two regions: with or without clear

focused surface texture. To separate the edge *A* from the results of edge detector, the following approach has been developed. The first step in this approach is to check which side of the image has no clear focused surface texture. It can be achieved by dividing the image into two parts and counting the number of the results of edge detector in both side. The side which has the smaller number is the side which has no clear focused surface texture because nearly no edge can be found in this area. The results of the edge detector are then examined along every horizontal line from without-clear-focused-surface-texture side to with-clear-focused-surface-texture side (from left to right for edge *A*). The first edge met is considered as edge *A*. This procedure is just like a micrometer measurement. The spindle is screwed towards the object until it touches the surface. The final result of edge *A* is plotted back in the original image and is shown in Figure 6-10 (b). Each digital image covers a region of 0.55x0.77 mm. The result of the measurements are:

AB= 21.364±0.0025 mm and AC= 29.401±0.0025 mm.

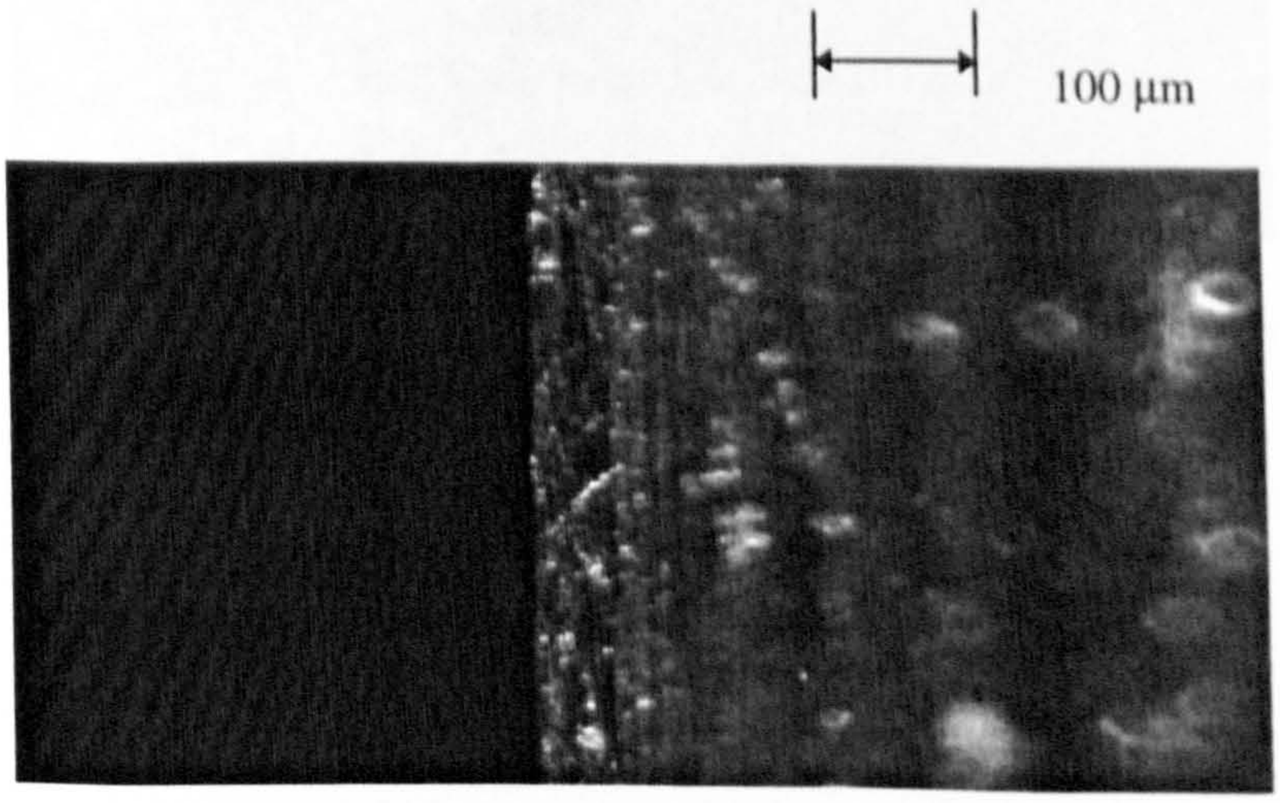

Figure 6-5 Edge at A

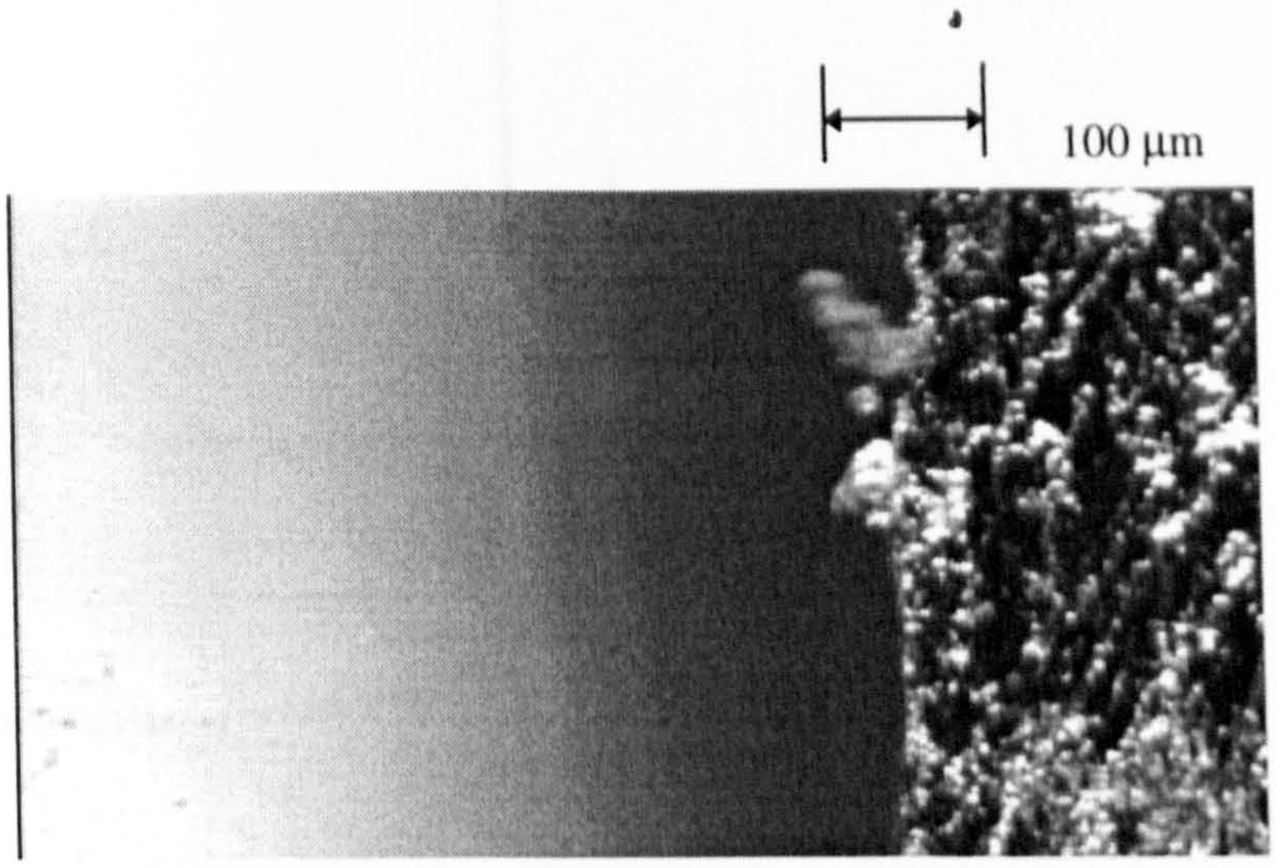

Figure 6-6 Edge at B

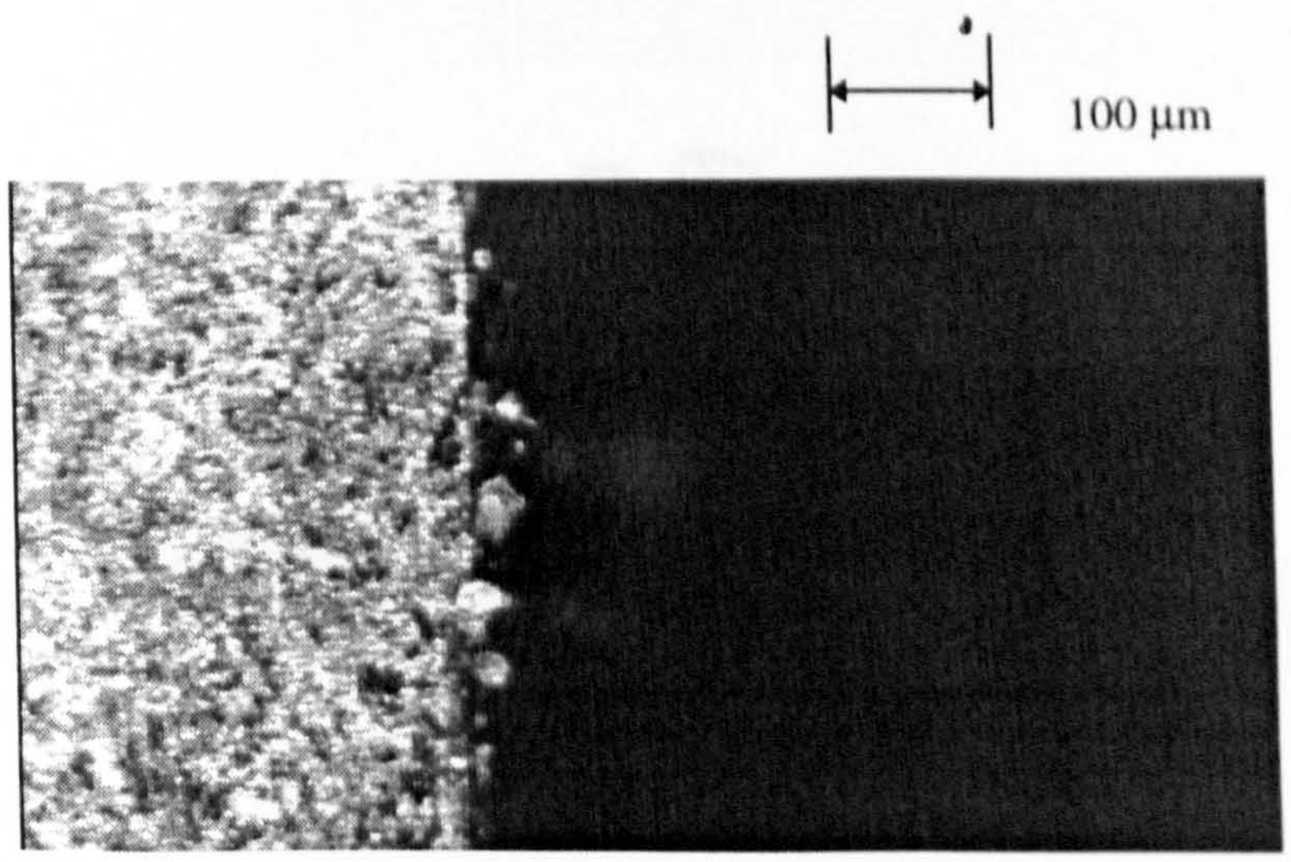

Figure 6-7 Edge at C

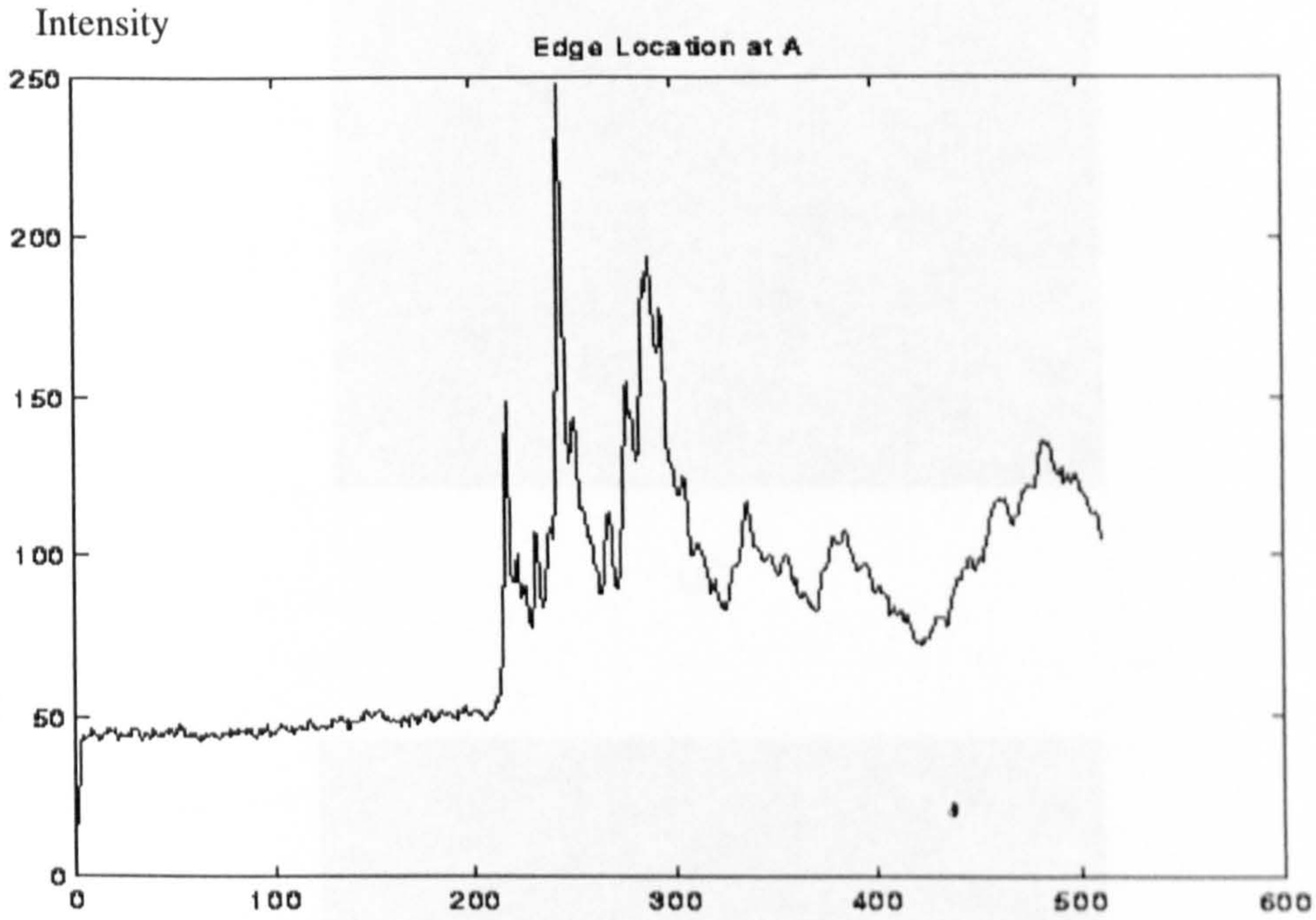

Figure 6-8 A plot of light intensity across the edge A

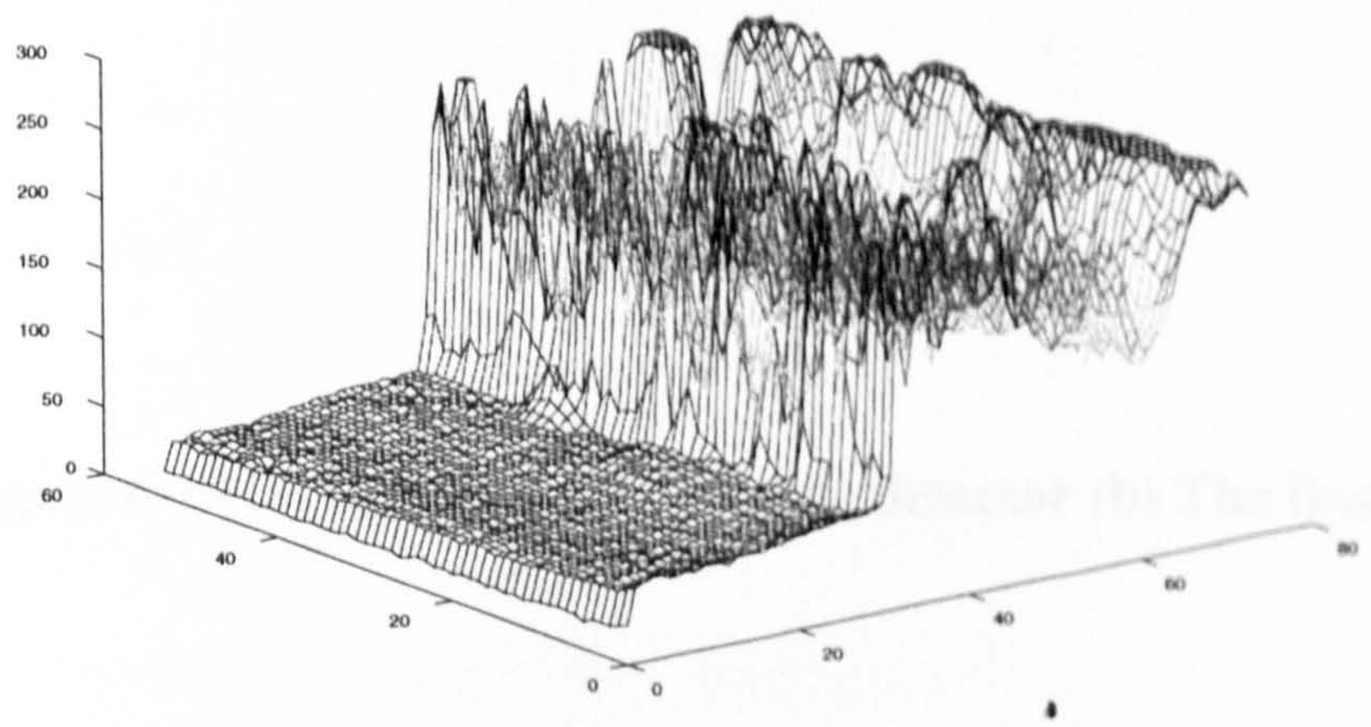

Figure 6-9 2-D plot of edge A

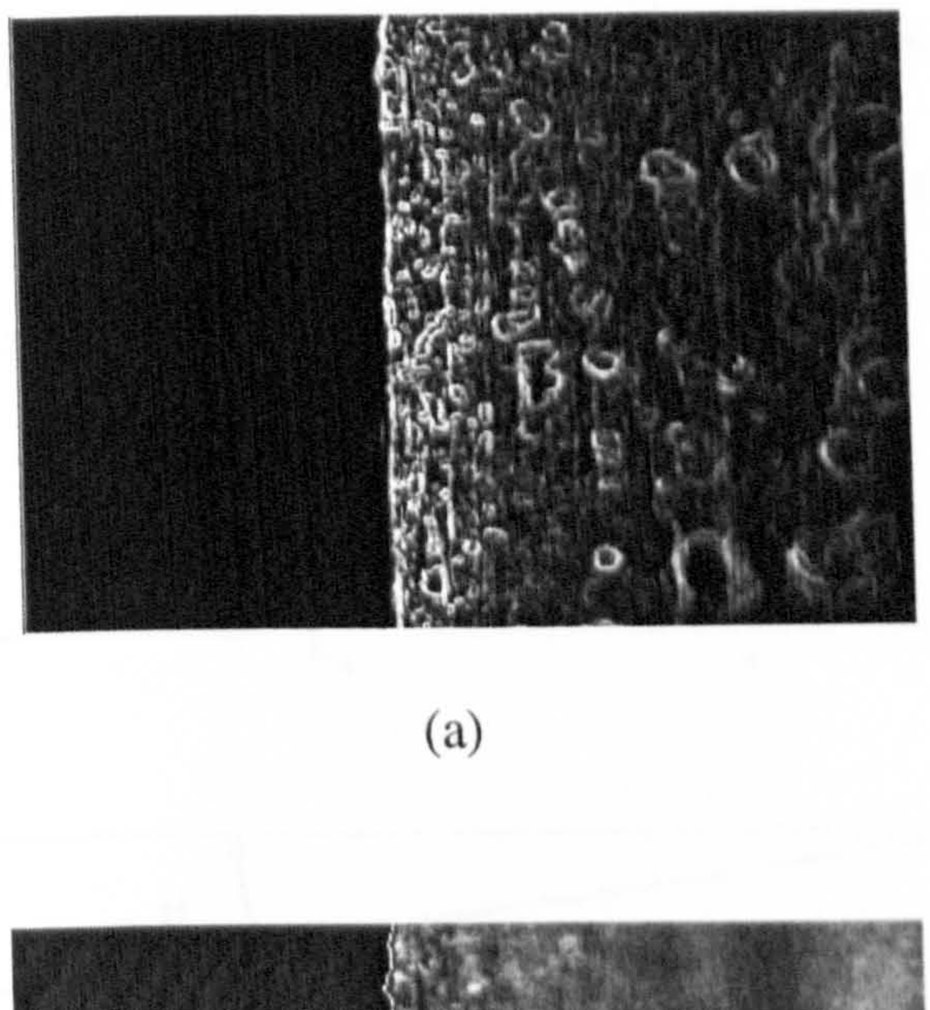

Figure 6-10 (a) Result of a usual edge detector (b) The final result

6.4 Discussion

6.4.1 The accuracy of stage movement

If component moves along the an axis other than the axis of the optical system, errors are generated. The errors are divided into two: E_x and E_y. E_x is caused by and X movement as shown in Figure 6-11, where L_x is the real length of the

component, θ_x is the angle between the axis of the component and the direction of X movement. Thus the error can be find from the following equation:

$$E_x = L_x(1- \cos(\theta_x)) \qquad 6.2$$

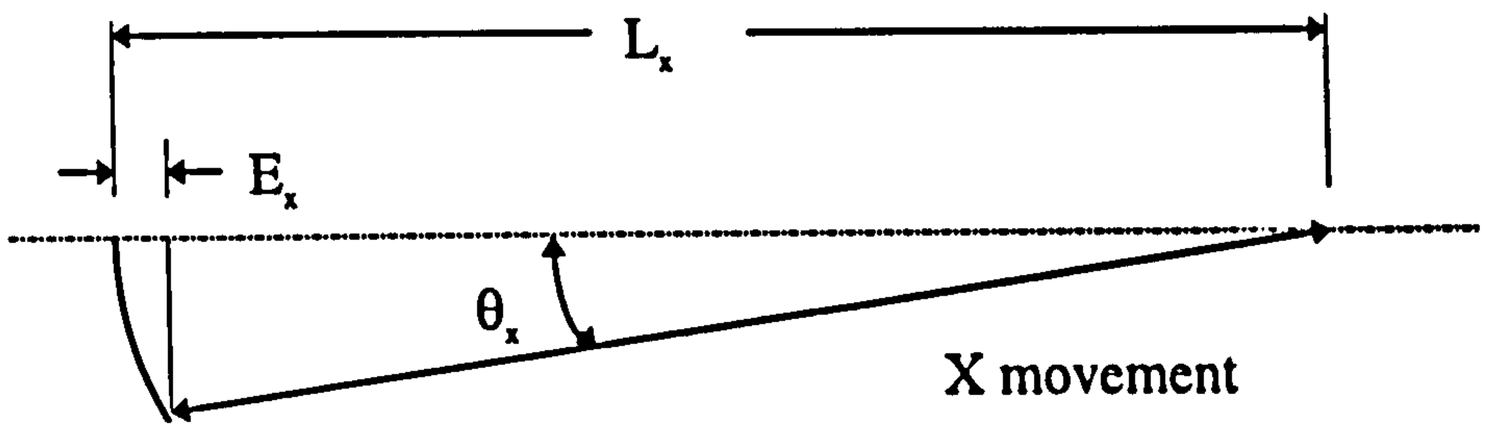

Figure 6-11 The error in X movement

E_y is caused by Y movement as shown in Figure 6-12, where L_y is the displacement of the component in Y direction. The error can be found from the following equation:

$$E_y = L_y \, tg(\theta_Y) \qquad 6.3$$

To work out the tolerance of θ_y and θ_x, it is reasonable to require that these errors must be smaller than half of the system resolution within the whole range. In this measurement $L_x = 50$ mm, $L_y = 1.5$ mm and $E_x = E_y = 2$ μm . The angles θ_x and θ_Y therefore must satisfy:

$$\theta_x < 0.57^0 \text{ and } \theta_Y < 0.095^0 .$$

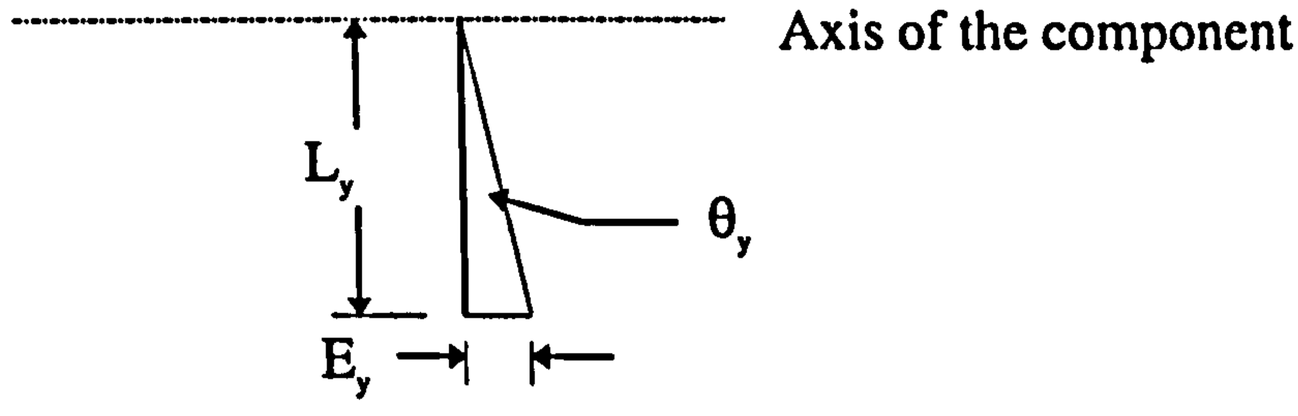

Figure 6-12 The error in movement of Y

6.4.2 Mirror size

Large mirror will reduce the flexibility of the system, while a small one may reduce the resolution of system. The ideal size should be the smallest mirror before the numerical aperture of the system is reduced. Referring to Figure 6-13, where D_1, D_2 and D_3 are the diameter of the lens, mirror and the surface size which can be imaged respectively. While L_1 is the working distance, L_2 is the distance from the mirror to the surface. With two added dash line, two similar triangles are formed. The following relationship can be therefore found:

$$(D_1 - D_2)/(L_1 - L_2) = (D_1 - D_3)/L_1 \qquad 6.4$$

Thus the ideal diameter of the mirror is defined:

$$D_2 = (L_1 D_3 + L_2 D_1 - L_2 D_3)/L_1 \qquad 6.5$$

In this system, $L_1 = 60$ mm, $L_2 \leq 10$ mm, $D_1 = 20$ mm and $D_3 \leq 0.77$ mm. Therefore as long as D_2 is bigger than 4 mm, the resolution is not reduced by the mirror. This size, less than third of the diameter of the hole, would allow much flexibility to install the light guides.

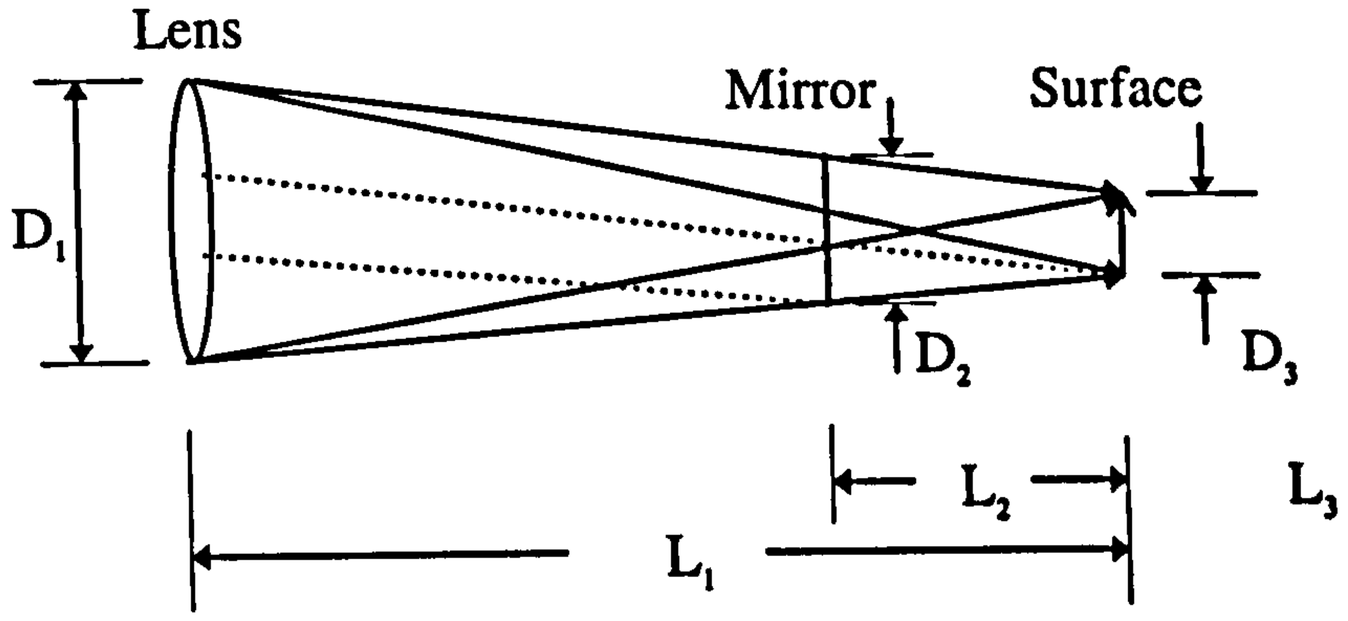

Figure 6-13 About mirror size

6.4.3 Improvements.

1) By taking a series of measurements with known sub-pixel movements and digitally averaging the information the resolution of the system could be increased.

2) A confocal internal illumination approach could be used to yield internal tolerances of better than 0.1 μm.

3) The device demonstrated could lead to a 'clever internal camera system' which could be used for example, to optically 'crawl' within very complicated structures and tolerance them. It would also provide a method of checking normally inaccessible interior passages.

7 Further research and applications

Non-destructive methods, which are based on digital image processing and conventional microscopy have been developed for internal dimension and surface finish measurements. The key parts in the methods are random edge detection and shadow image reconstruction.

Random edge detection has been used to measure the diameter and the straightness of Cummins diesel engine injector holes and Courtauld's spinnerette holes. It has also been used to measure a Rolls-Royce turbine blade hole, where the thickness between the internal surface to the outside of blade is special required. An accuracy of ± 3 μm for single image analysis and ± 1.5 μm for sub-divided images analysis has been achieved (chapter 4).

A shadow image of the internal surface of a small hole has been reconstructed, from which the surface finish parameters R_a and R_q have been measured. The measurement has been verified by both χ^2 Test of Goodness-of-fit and comparing with stylus measurements.

To complete the optical internal measurement, a method has also been developed for measuring the dimension of the feature inside a 15 mm diameter hole. The internal structural dimension of a diesel engine component has been measured. The accuracy is ± 2.5 μm

Further research and application are discussed in this chapter.

7.1 Internal dimensional measurement

In general, as with all metrological methods, the potential for further research are in increasing the accuracy, resolution and computation speed. In particular, random edge detection (locating the centre curve of the in-focus-strip) is a critical aspect of the internal dimensional measurement and requires further studies.

7.1.1 The accuracy

Figure 4-4 shows the error in locating the centre of the in-focus-strip. Two ways might increase the accuracy. They are:

1) improving the original image;

2) improving the random edge detection algorithm.

7.1.1.1 Improving original image:

One obvious experience gained during the project is that the most accurate measurements are made from the highest quality images. Thus, the light source, microscope objective and camera each need to be optimised in order to improve the overall accuracy of the whole system.

- Illumination: It has been mentioned that the dynamic grey level range of a digital image is 2^8 and the local signal of a random edge can be set to vary

fully inside the range. However, to achieve this setting for the whole random edge inside the image, the internal surface of the hole must be evenly illuminated. Figure 7-1 gives a further explanation. In figure 7-1(a), the internal surface is not illuminated evenly, the signal of the whole random edge cannot be set to vary fully inside the dynamic grey level range. However with an even illumination, the signal of the whole random edge varies fully inside the range as shown in figure 7-1 (b).

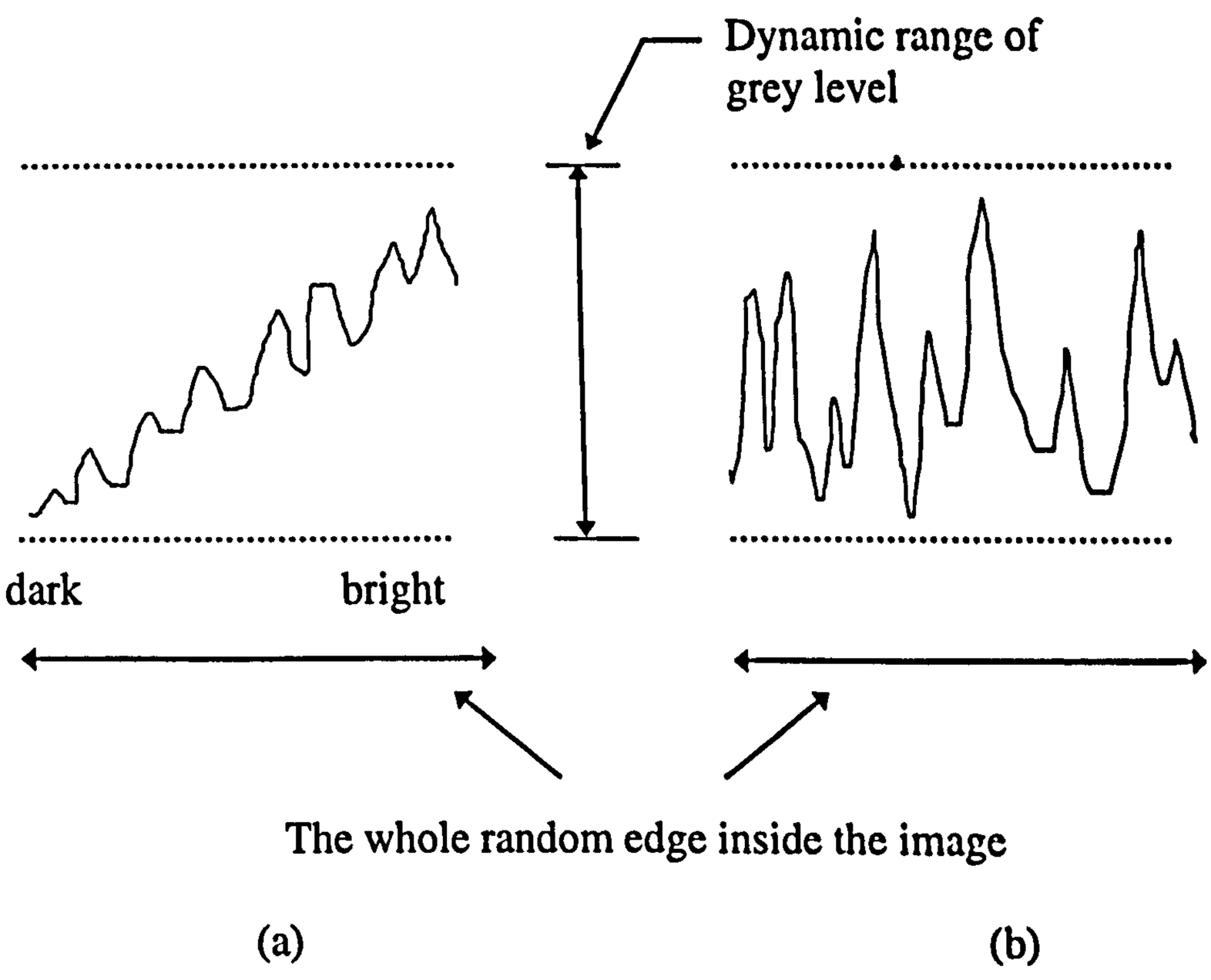

Figure 7-1 The importance of even illumination: (a) uneven illumination with lower signal level. (b) even illumination with higher signal level

- Objective: Because of the uneven response for every sensor unit in CCD camera and the limited quantization steps in the A/D converter, noise is added into the digital image during the image conversion from the original analogue image to the digital image. The frequency of this noise is the inverse of the

sampling interval and does not vary with the magnification of the objective. However, the larger the magnification of the objective is chosen, the larger the surface details in an image can be got. The result is that the frequency of the surface details in the image is reduced. This reduction gives the frequencies of noise and the in-focus-strips a pre-separation as shown in Figure 7-2. The noise can be easily filtered off because of this pre-separation, the accuracy of measurement is therefore increased.

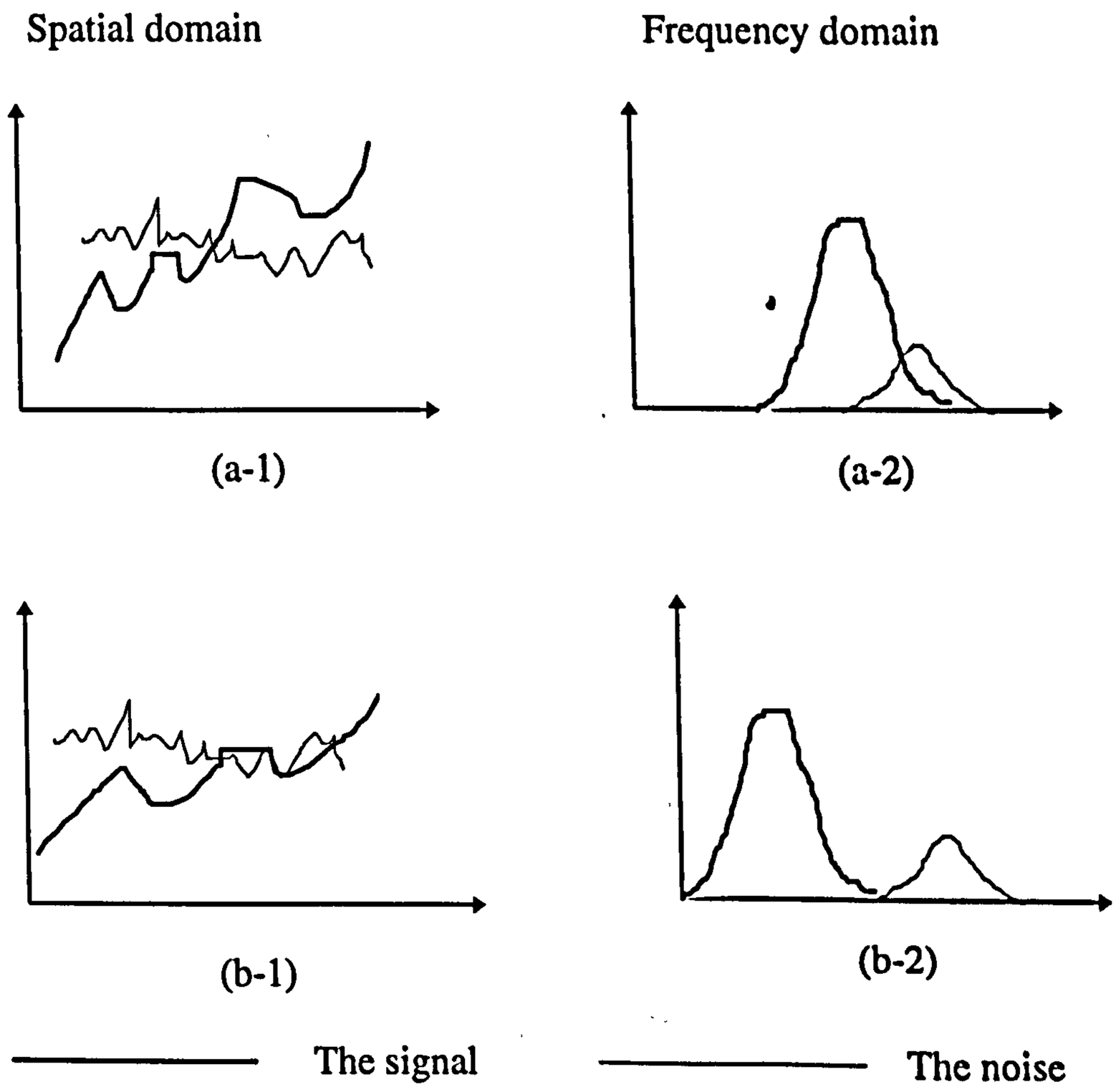

Figure 7-2 Pre-frequency separation by larger magnification objective

(a) 1 and 2 are the image captured by lower magnification objective.
(b) 1 and 2 are the image captured by larger magnification objective.
In the frequency domain, it can be see that the frequencies in the image captured by larger magnification objective are better separated than that in the images captured by lower magnification objective.

Camera: A more powerful objective produces a larger image. It therefore requires either a large sensor area camera or several sub-divided small images to represent the whole image. Unfortunately these two methods need more computer memory and longer processing time. Figure 7-3 is drawn for the explanation, where n is the number of pixels along a side of the image and θ is pre-defined angle between sample lines. The size of memory needed is increased with n^2. If m and l denote number of pixels along the data sampling line and the number of lines respectively, the data need to be processed increase with a factor between n to n^2. This is because the length of sampling line m is proportional to the size of the image n. If the number of lines l is fixed (θ is fixed), the data is increased with n. If the interval between lines is fixed, the number of lines is proportional to the size of the images, the data is therefore increased with a factor of n^2.

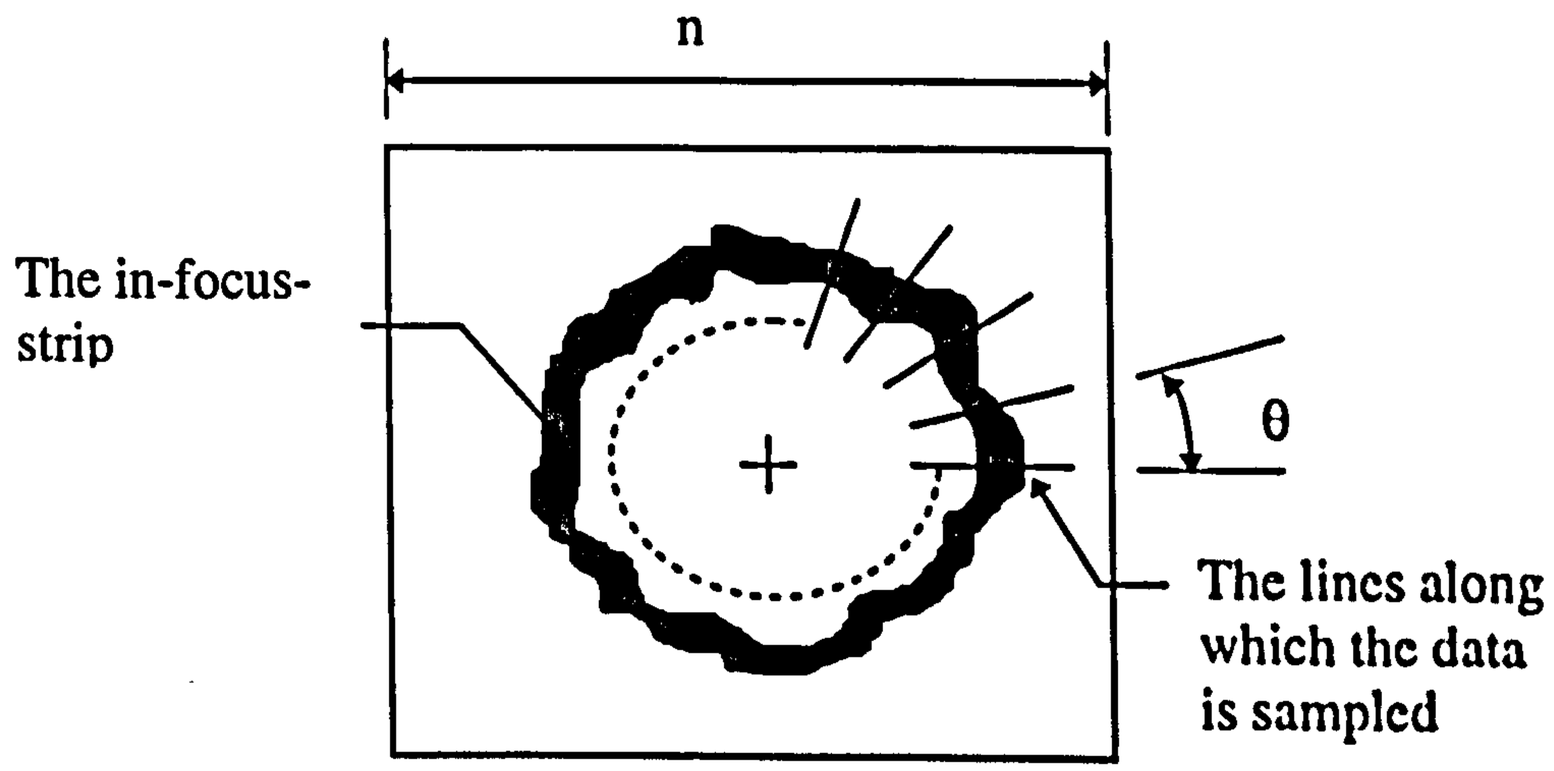

Figure 7-3 Illustration of the increase in file size and processing data

The random edge detection is basically a one dimensional processing, where finite impulse response (FIT) or infinite impulse response (IIR) filters are used. The computing time of these kind filter is linear with the total data to be dealt with. Therefore the total computing time is increased with the total data collected.

7.1.1.2 Improve software in edge detecting:

Besides using a more powerful objective to separate the signal and noise, a more complicated digital filter with a narrower distinguish frequency band can also be used. This kind of filter can reduce the noise with less signal blurring, even for cases where the frequencies of noise and the signal are not well separated. However, this kind of filter means a more complicated form of Eq 3.1 and Eq 3.2. A longer processing time is therefore required.

7.1.2 Resolution

Currently, when measuring a 125 μm diameter hole in ceramic connector, the error is quite large (30%). (The connector is provided by Marconi Electronics. It is used to construct the equivalent of a RS232 connector for fibre optic inter-connects.) Figure 7-4 is an image of the hole. It can be seen that the quality of the image is low. There is no clear in-focus-strip in the image. The possible reasons are: stronger internal multiple reflections and the non uniform optical characteristics of ceramic materials.

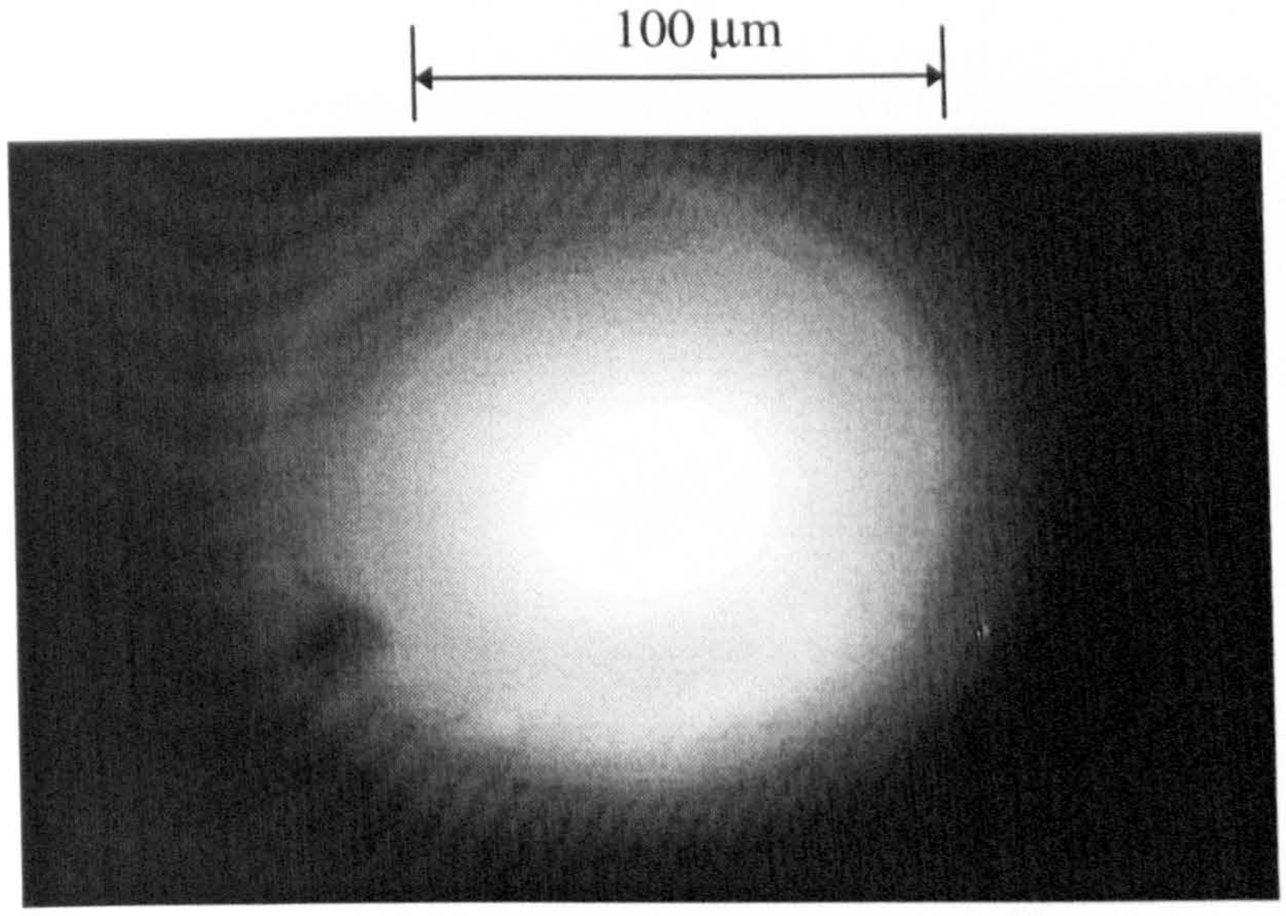

Figure 7-4 An image of 125 μm hole ceramic

7.1.2.1 Internal multiple reflections

Every point of the internal surface is also illuminated by multiple reflections from the rest of the surface. These multiple reflections come from random directions. They therefore reduce the contrast of the shadow pattern. The total intensity of the internal multiple reflections is a function of two factors:

1) the propagation distance (the intensity of scatted light from every point attenuates with the square of the distance which is proportional to the diameter of the hole);

2) the area of the internal surface where the reflections come from(this area is also proportional to the diameter of the hole).

That is:

$$I_m \propto \int \frac{1}{D^2} ds \propto \frac{s}{D^2} = \frac{\pi dL}{D^2} \propto \frac{1}{D}, \qquad 7.1$$

where I_m is the intensity of total multiple reflection; D is the diameter of the hole; s is the internal surface of the hole and the L is the length of the hole. If the length of the hole is fixed, the intensity of the internal multiple reflection is inverse to the diameter of the hole. As the diameter reduces from 200 μm (Cummins hole) to 125 μm, the intensity of multiple reflection is near doubled. There is therefore no clear in-focus-strip in the image.

The following proposals might reduce the internal multiple reflections and are worth further study.

1) Introduce polarised light for illumination. The fraction of light reflection from a surface is a function of the polarisation and the incident angle of the light[1]. When linear polarised light is used, the whole internal surface can be roughly divided into two regions: the surface is either parallel or vertical to the polarisation as shown in Figure 7-5. The reflection in region *I* is weaker than that in region *II*. Therefore in region *II*, the multiple reflection received is weaker, where should improve the quality of the random edge.
2) The use of a spatial filter in illumination. A carefully chosen ring-like spatial filter can limit the light only to illuminate the interested area. It might reduce the total amount of multiple reflection inside the hole. Therefore the image quality of the random edge can be improved. Figure 7-6 illustrates this proposal.

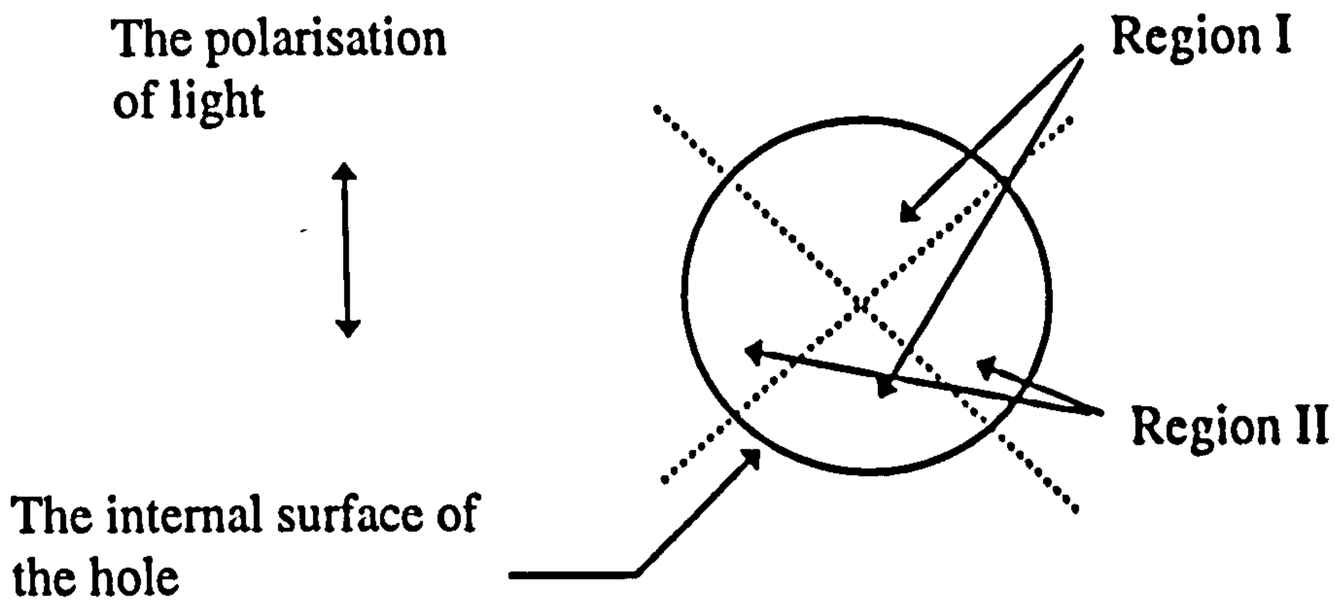

Figure 7-5 Polarised illumination. In region I, the surface is parallel to the polarisation of the light, the reflection is weaker than that of region II.

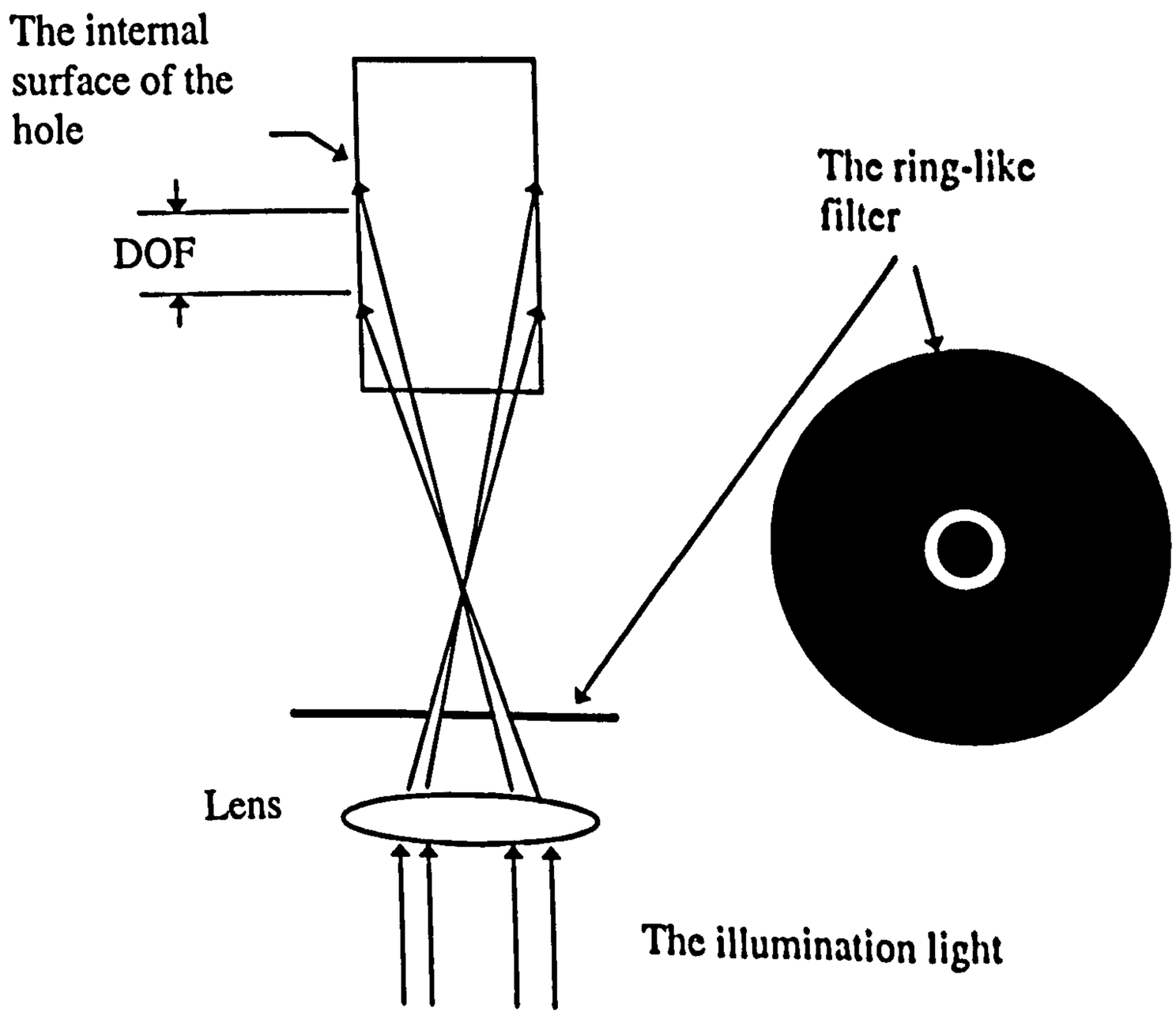

Figure 7-6 Proposal for illumination with a ring-like filter

7.1.2.2 The optical characteristics of ceramic

The second reason for poor clarity in the in-focus-strip might be the difference of optical characteristic between ceramic and metal materials. A method to increase the image quality might be found from a study of the optical property of the ceramic material of the component. For example the reflection fraction as a function of wavelength. Some information might be got if different wavelengths of light source are used[2] [3] [4] [5].

7.1.3 Computation speed

There are two ways to increase computation speed.

1) Using suitable programmer language. Most of the programmes are developed in Matlab as this package is easy and flexible to test ideas. But the computation speed is low. After the ideas have been proved, a C++ programme will increase the computation speed.
2) More intelligent programme. The programme can be more intelligent. For example, the location of the in-focus-strip does not change very much between two neighbouring strips, the random edge detection can be limited to only search a small area around the location of the previous strip. The total data needed to be processed is reduced, so that the computation speed is increased.

7.2 Internal surface roughness measurement

There are two parts in this measurement, reconstructing the shadow image and making a shadow model. Both of them can be improved by further considerations.

7.2.1 Reconstructing shadow image.

The shadow image is reconstructed from a set of in-focus-strips. In the in-focus-strip, the brightness reduced from the side near to the centre of the hole to the outside. During the shadow pattern reconstruction, the brighter side of an in-focus-strip is always connected with the darker side of a neighbouring in-focus-strip. A smoother connection might be obtained by considering the changes of brightness in every in-focus-strip. The brightness might be a function of the illumination profile.

7.2.2 Shadow model

Current assumptions of the shadow model are very simple:

- there are shadows at the side of the peaks or valleys towards the observer;
- the peaks or valleys are far apart enough so that there is no blockage of measuring the size of shadow;
- the distribution of the height of the peaks and the depth of the valleys are the same.

A more complicated model which can take account of blockage would either improve the measurement or prove that the simple assumption is good enough for evaluating statistical measurement.

7.3 Other methods of internal inspection

Nowadays as more and more complicated components are widely used, different internal inspection techniques are required. A probe with thousands of fine light guide has been produced as shown in Figure 7-7 (a product of Ultrafine[1]). The internal feature can be imaged by this probe, but this probe can only give an view of internal surface. A possible method to achieve quantitative analysis is to add a few single model optical fibres within the fine light guides. These fibres can be used to create structured light (such as fringe patterns) inside the component. The pattern of structured light can then be viewed from the probe. The internal surface profile can be therefore measured by analysing the deformation of the structure light patterns on the internal surfaces. Currently the pixel density of the probe can be made more than 6,000 pixels in a 1.5 mm diameter area.

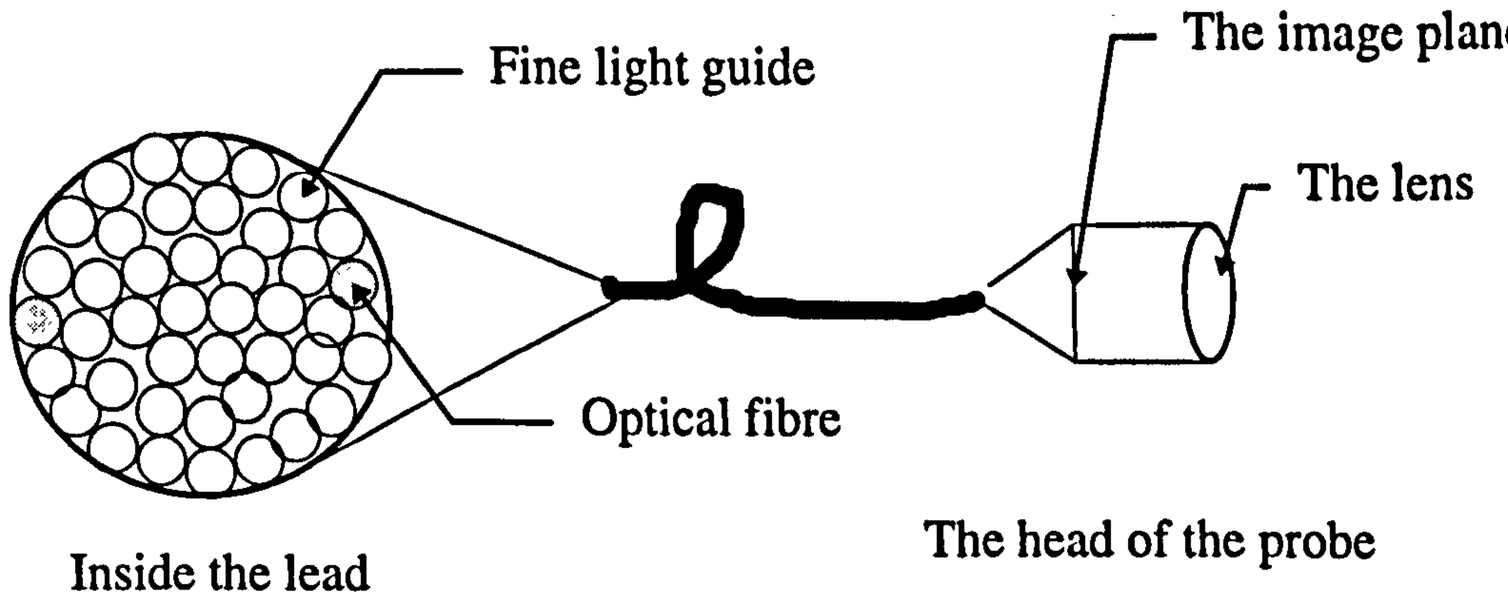

Figure 7-7 A fine light guide bundle probe

[1] Ultrafine Ltd. Brentford Middx UK

References

[1] W. G. Driscoll and W. Vanghan "Polarization" Chapter 10 in *Handbook of Optics* McGraw-Hill Book Company 1978

[2] J. A. Ogilvy *Theory of wave scattering from random rough surfaces* Adam Hilger 1991

[3] J. M. Elson, J. M. Bennett and J. C. Stover " Wavelength and angular dependence of light scattering from beryllium: comparison of theory and experiment" *Applied Optics* **32**(19) 3362-3376 (1993)

[4] J. A. Sanchez-Gil and M. Nieto-Vesoerinas "light scattering from random rough dielectric surface" *J. Optical Society of American A* **8**(8) (1991)

[5] J. A. Sanchez-Gil and A. A. Maradudin "Limits of validity of three perturbation theories of the specula scattering of light from one-dimensional, randomly rough, dielectric surfaces" *J. Optical Society of American A* **12**(7) 1547-1558 (1995)